SINGLE-NEUTRON KNOCKOUT REACTIONS:
APPLICATION TO THE SPECTROSCOPY OF $^{15,16,17,19}$C

By

Valentina Maddalena

AN ABSTRACT OF A DISSERTATION

Submitted to
Michigan State University
in partial fulfillment of the requirements
for the degree of

DOCTOR OF PHILOSOPHY

Department of Physics and Astronomy
and
National Superconducting Cyclotron Laboratory

2000

Professor P. Gregers Hansen

**ABSTRACT**


SINGLE-NEUTRON KNOCKOUT REACTIONS:
APPLICATION TO THE SPECTROSCOPY OF $^{15,16,17,19}$C


By


Valentina Maddalena

The technique of one-nucleon removal reactions has been recently developed at the NSCL to study the single-particle stucture of nuclei far from stability, close to both the proton and the neutron drip lines.

Among those, the neutron-rich carbon isotopes $^{16,17,19}$C have been investigated to understand their essentially unknown structure. In particular, $^{17,19}$C are both characterized by a low neutron separation energy, one of the typical signatures of the halo character. The technique consists in the measurement of partial cross sections, and their associated momentum distributions, corresponding to the final states of the $^{15,16,18}$C residues. These are compared with predictions based on shell-model calculations and an eikonal model of the reaction mechanism.

As a test case, the well-known nucleus $^{15}$C has been investigated. The absolute validity of the spectroscopic factors extracted by our method will be discussed. The measured momentum distributions of the residues have revealed a characteristic broadening and low-energy tail, observed already for the $\ell = 0$ halo of $^{11}$Be. Moreover, an interdependence between scattering angle and momentum has been observed and interpreted theoretically as arising from the diffractive channel.

Spectroscopic factors and $\ell$-value assignments for all the isotopes have been ex-

tracted. The ground-state spins of $\frac{3}{2}^+$ and $\frac{1}{2}^+$ have been assigned to $^{17}$C and $^{19}$C, respectively. An estimate for the one-neutron separation energy for the ground state of $^{19}$C has been obtained, suggesting that it be revised upwards.

SINGLE-NEUTRON KNOCKOUT REACTIONS:
APPLICATION TO THE SPECTROSCOPY OF $^{15,16,17,19}$C


By

Valentina Maddalena


A DISSERTATION


Submitted to
Michigan State University
in partial fulfillment of the requirements
for the degree of


DOCTOR OF PHILOSOPHY


Department of Physics and Astronomy
and
National Superconducting Cyclotron Laboratory


2000

# ABSTRACT

## SINGLE-NEUTRON KNOCKOUT REACTIONS: APPLICATION TO THE SPECTROSCOPY OF $^{15,16,17,19}$C

By

Valentina Maddalena

The technique of one-nucleon removal reactions has been recently developed at the NSCL to study the single-particle stucture of nuclei far from stability, close to both the proton and the neutron drip lines.

Among those, the neutron-rich carbon isotopes $^{16,17,19}$C have been investigated to understand their essentially unknown structure. In particular, $^{17,19}$C are both characterized by a low neutron separation energy, one of the typical signatures of the halo character. The technique consists in the measurement of partial cross sections, and their associated momentum distributions, corresponding to the final states of the $^{15,16,18}$C residues. These are compared with predictions based on shell-model calculations and an eikonal model of the reaction mechanism.

As a test case, the well-known nucleus $^{15}$C has been investigated. The absolute validity of the spectroscopic factors extracted by our method will be discussed. The measured momentum distributions of the residues have revealed a characteristic broadening and low-energy tail, observed already for the $\ell = 0$ halo of $^{11}$Be. Moreover, an interdependence between scattering angle and momentum has been observed and interpreted theoretically as arising from the diffractive channel.

Spectroscopic factors and $\ell$-value assignments for all the isotopes have been ex-

tracted. The ground-state spins of $\frac{3}{2}^+$ and $\frac{1}{2}^+$ have been assigned to $^{17}$C and $^{19}$C, respectively. An estimate for the one-neutron separation energy for the ground state of $^{19}$C has been obtained, suggesting that it be revised upwards.

To my family, my friends, and my love Bruno!

# ACKNOWLEDGMENTS

Many people have contributed in making my four years at Michigan State University unforgettable.

First of all, I am deeply grateful to my advisor Gregers Hansen, my continuous source of wisdom. He has led me through the intricacies of physics with much patience and always with a smile.

I wish to thank Thomas Glasmacher, S. D. Mahanti, C. P. Yuan, and Vladimir Zelevinski, for serving in my committee and for nice and fruitful discussions.

I am also indebted to Alex Brown and Jeff Tostevin, my theory guides. Thank you for providing me with the calculations, and even with the opportunity (and thrill) of running some programs myself!

Thank you Navin, for being such a good friend and always there to guide me in the data analysis and interpretation. It was great working with you!

My gratitude goes also to the S800 collaboration, the operators and all who helped in the experiments, making them successful, and especially Brad Sherrill, Daniel Bazin, and Mathias Steiner.

Thank you to Joachim, with whom I could share the ups and downs of the analysis, and for his helpful hints for my thesis.

Thank you to the ones who helped me to come here, without whom I could have

# Contents

# List of Tables

# List of Figures

# Chapter 1

# Introduction

## 1.1   Motivations for the study of nuclear structure

Radioactivity was found by Henri Antoine Becquerel in 1896 and the subsequent discovery of readioactive elements by Pierre and Marie Curie earned them the 1903 Nobel Prize for Physics. With Rutherford's discovery of the atomic nucleus the basis had been laid for all subsequent research on nuclear physics and for a development that still continues, one hundred years later. Although the present work is concerned only with basic aspects of nuclear structure, it should be pointed out that there are many practical applications of nuclear physics in various fields, such as medicine, biology, archeology, national security and energy generation.

The properties of matter are determined by the number of protons and neutrons in a nucleus. In particular, the number $Z$ of protons characterizes the different elements, from hydrogen to uranium; depending on the number $N$ of neutrons, each element can be present in nature in a variety of isotopes. The stable elements that exist in nature are 80 and there are almost 300 stable isotopes. When displayed in the chart of the nuclides (Fig. 1.1), where the number of protons $Z$ is plotted against the number of neutrons $N$, the stable nuclei lie approximately along the diagonal from the lower left to the upper right, called the valley of stability.
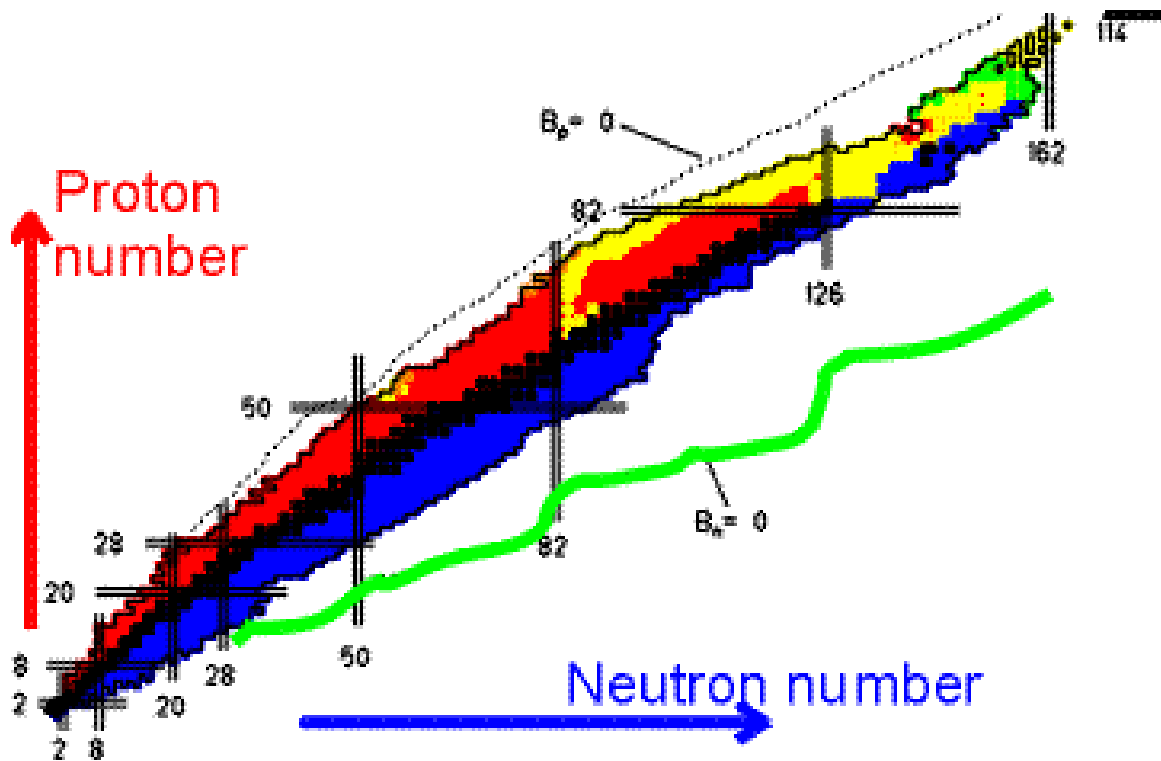
Figure 1.1: The chart of nuclides. The valley of stability is indicated by the black dots representing the stable nuclei in nature. The limits of nuclear stability are indicated by the proton and neutron drip lines, behind which no bound nuclei can exist. The double lines indicate the magic numbers for the stable nuclei.

However, thousands of radioactive isotopes are stable in time scales that are long compared with the time of nuclear intrinsic motion ($10^{-22}$ s). Their properties offer important clues to nuclear structure, and to astrophysics as well. In fact, they are continually created in the cosmos and play a crucial role in the evolution of the stars and in the origin of the elements in our solar system 4.5 billion years ago. Most of them cannot be found naturally on earth because they decay by different mechanisms into stable species with half-lives that range between less than a thousandth of a second to billions of years. These unstable isotopes lie away from the line of stability, in the region within the neutron and proton drip lines, which define the limits beyond which nuclei become unstable to nucleon decay. Due to their distance from the valley of stability, nuclei close to the drip lines are often referred to as "exotic" nuclei, indicating entities different from the most ordinary ones, available in nature.

The drip lines have experimentally been reached only for the lightest 8 elements and their position in the nuclear chart is not exactly known yet. Therefore, in order to test existing nuclear structure models, one of the most important topics of research in nuclear physics is the exploration of the nuclear chart to find out where the limits of nuclear binding are. One of the most remarkable results of these studies was the discovery of novel nuclear structures in nuclei far from stability in the last decades of the $20^{th}$ century. Being characterized by very different properties than ordinary nuclei, these exotic nuclei have a thin cloud of nucleons orbiting at large distances from the others, forming the core. In analogy with the luminous ring around the sun or the moon seen under certain meteorological conditions, these nuclei are referred to as "halo nuclei".

Besides the search for the exact position of the drip lines in the nuclear chart, other motivations to investigate nuclei far from stability are the quests for which combination of protons and neutrons can make up a nucleus; what are the properties

3

of nuclei with an extreme proton-to-neutron ratio; or how existing models should be modified in order to describe rare isotopes.

The study of nuclei far from stability is not intrinsic to itself, but it has important implications in the understanding of many astrophysics phenomena. An example is the solar neutrino problem, related to the $^7$Be(p,$\gamma$)$^8$B reaction taking place in the sun, or the CNO-cycle in the nucleosynthesis process and all nuclear reactions taking place in the stars, under extreme nuclear matter conditions.

Thus, the investigation of the properties of exotic nuclei has become one of the most important goals in nuclear physics and it is now possible thanks to the development of modern technologies available for radioactive beam production and heavy-ion accelerators.

In an effort of fine-mapping the nuclear chart, the essentially unknown structure of the heavy carbon isotopes $^{16,17,19}$C has been investigated in this work. The experimental approach used for this purpose is a new technique originally designed to study halo nuclei, but that was found to be a powerful tool to probe the structure of any exotic nucleus. The technique was tested using a beam of $^{15}$C, the structure of which is well known. Before describing the technique in detail, a brief overview on the properties of halo nuclei is given below.

## 1.2  Properties of Halo Nuclei

Nuclei at the drip lines are filled with nucleons up to the limit set by the combination of the nuclear kinetic energy and the depth of the nuclear potential well, resulting in a bound state close to the continuum. The binding energy for this state is very small and, due to the short range of the nuclear force, threshold effects appear. The last nucleons undergo the quantum-mechanical effect of tunneling, so that their

probability of being at large distances from the core is appreciable. This is what was referred to as "halo" state for the first time in 1987 [Han87] and since then the term halo has been referred to all exotic nuclei manifesting those properties. The manifestation of the halo phenomenon is less evident if the halo nucleons are in a state of large angular momentum ($\ell > 1$), in which case the centrifugal barrier lowers the probability of tunneling far from the core. Analogously, the Coulomb barrier hinders the formation of proton halos, because the repulsion between the protons and the nuclear core makes it difficult for the nucleons to tunnel. The Coulomb repulsion also affects the absolute binding, so that the proton drip line actually lies closer to the valley of stability than the neutron drip line.

The most simple halo nucleus is the deuteron, although when it was first studied it was not labeled as such. Its binding energy is only 2.22 MeV and the average distance (root-mean square) between the neutron and the proton is 3.9 fm. Other halo nuclei observed so far include neutron halos as well as proton halos. Neutron halo nuclei exist in a variety of configurations, where the halo may be formed by one, two or four neutrons, as is the case for $^{11}$Be (1-$n$ halo), $^6$He, $^{11}$Li, $^{14}$Be and $^{17}$B (2-$n$ halo), $^8$He (4-$n$ halo). An established case of one-proton halo is $^8$B. The hypertriton is an interesting example of halo nucleus, where the halo is not formed by a nucleon, but by the $\Lambda$ particle, orbiting around a deuteron core. The estimated separation energy is as small as $0.08 \pm 0.02$ MeV [Boh70, Boh68]. More recently halo-like states have been discovered in deeply bound pionic states in heavy nuclei [Yam96]. At the atomic scale examples of halo states may be negative ions or two-electron atoms, although these are bound by the long range Coulomb potential. Systems subject to a potential which decreases with distance faster than the Coulomb potential, such as an electron bound in the field of a dipole, or noble gas molecules subject to the weak van der Waals force present analogies to the nuclear halo states as well.

Several are the experimental signatures of a halo nulceus. Tanihata et al. [Tan85, Fuk91] measured surprisingly large interaction cross sections in a series of experiments on the neutron-rich $^{6,8}$He and $^{11}$Li. This result was interpreted as due to a long tail in the wave functions of those nuclei. It was also found [Arn87] that the proton distributions in $^{9}$Li and $^{11}$Li are the same, which led to the conclusion that the broad spatial distribution in $^{11}$Li was to be attributed to the neutrons. Moreover, while the interaction cross sections were found to increase with the mass number of the $^{8,9,11}$Li isotopes, those were shown to be constant as a function of mass in reactions which changed the proton number [Bla92].

Coulomb dissociation cross sections were also expected [Han87, Ber88] and later observed [Kob89, Nak99] to be surprisingly large. As a direct consequence of the Heisenberg principle, extended spatial distributions manifest themselves as narrow momentum distributions of the fragments produced in breakup reactions of halo nuclei. Observations of this effect were found for a number of nuclei [Kob88, Ann90, Orr92, Baz95, Baz98, Bau98, Aum00, Gui00, Nav00].

Is any of the carbon isotopes studied in this work a halo nucleus? Those are certainly good candidates, especially $^{15}$C, $^{17}$C and $^{19}$C, with their low separation energies (1.218, 0.74, 0.8$\pm$0.3 MeV, respectively, the last value from this work), but more details on their wave functions need to be known. Much information has been obtained indeed with the experimental approach used for this work and the results are discussed in Chapters 4 and 5. We shall see that $^{19}$C is definitely a halo state, from what we know as good a case as $^{11}$Be.

## 1.3 Experimental approach

The most traditional method used to study ordinary nuclei consists in bombarding the nucleus of interest in the form of a target with a stable beam. Obviously such a method can not be used for the study of short-lived nuclei, as it would require the use of a radioactive target. The experimental approach to study short-lived radioactive isotopes is then reversed with respect to the traditional method, in that radioactive beams of the nuclei of interest are produced and react on a stable target. In these experiments the kinematics is referred to as "inverse", as the measurements are done with respect to the projectile's frame, rather than the target's.

Information on the various properties of exotic nuclei can be extracted from different kinds of experiments, such as Coulomb excitation, transfer reactions and breakup reactions. In a Coulomb excitation experiment the incident nucleus is excited by the Coulomb field of a heavy target and the $\gamma$ rays measured from the de-excitation provide information on the transition probabilities for the excited states.

Single-nucleon transfer reactions at low beam energies identify rather directly single-particle configurations of the nuclear wave function [Boh75, Sat90, Fes92]. The classic tools have been stripping and pickup reactions, such as the (d,p) and (p,d) reactions, and the analogous reactions for probing proton states. For medium mass and heavy targets these light ions have a short mean free path inside the nucleus. The reactions are therefore surface dominated. They can also be described usefully as one-step processes involving the transfer of a nucleon to or from a given single-particle state. The development of theoretical methods such as the distorted waves Born approximation (DWBA) has facilitated the use of transfer reactions to make angular-momentum assignments from the shapes of angular distributions, and to deduce spectroscopic factors from the magnitudes of measured cross sections.

Breakup reactions have been extensively used to measure interaction cross sections and the momentum distributions of the emerging fragments resulting from the removal of the halo nucleon(s). With the additional information from coincident $\gamma$ rays, this technique allows the identification of the various final states in the residues and it has been recently applied to a variety of exotic nuclei, including the carbon isotopes $^{15}$C, $^{16}$C, $^{17}$C and $^{19}$C which are the subject of this work.

Details of the technique and of the experimental setup used can be found in Chapter 2. The theories for the structure and the reaction mechanisms used to interpret the experimental data are illustrated in Chapter 3. The validity of the method used as a spectroscopic probe is demonstrated in Chapter 4 through the study of $^{15}$C, which was intended to serve as a test case, being its structure known. Finally, Chapter 5 presents detailed discussions of previous theoretical and experimental work on $^{16}$C, $^{17}$C and $^{19}$C, as well as the results from the experimental data of this work. The conclusive Chapter 6 offers some comments and a perspective on the potential of knockout reactions for precise single-particle structure studies with beams of rare isotopes. Details on the data analysis procedure are given in Appendix A.

# Chapter 2

# Experimental technique and setup

## 2.1   Single-nucleon knockout reactions

A new technique suited for spectroscopic studies of rare nuclei produced with low intensity as beams from fragmentation reactions has been recently developed at the NSCL. The projectile residues formed by removing a single nucleon in the interaction with a light target are observed in inverse kinematics. The final states of the heavy residues are identified by their $\gamma$ decay [Nav98, Tos99b, Aum00, Gui00, Nav00, Mad00]. The $\gamma$ rays tag reactions leading to individual discrete final levels and allow a determination of differential and integrated partial cross sections. It is possible to extend this technique to unbound final states by reconstructing the invariant mass (or other parameters of the intermediate state) from observations of the breakup products, see the recent work of Chen et al. [Che00] dealing with proton knockout from $^{11}$Be leading to the unbound systems $^{10}$Li and $^{9}$He.

Analogously to the reactions with light particles, e.g., the classical (p,2p) knockout reactions [Sat90], where the angular correlation between the emerging protons carries information about the momentum of the proton removed from the target, in single-nucleon knockout reactions the momentum of the removed nucleon can be reconstructed from the recoil of the observed heavy residue. The shape of the lon-

gitudinal momentum distribution identifies the orbital angular momentum $\ell$ of the removed nucleon, while the absolute removal cross section determines the spectroscopic factors. The transverse momentum components carry essentially the same information, but they are more sensitive to contributions from the reaction mechanism such as Coulomb deflection and diffractive scattering. The momentum components parallel to the beam direction are those that carry a clean signature of the momentum content related to the single-particle state in question. The results are shown in the laboratory system, as distributions of the quantity $P_{\|}$, which is the projection of the measured total momentum onto the beam axis. Since the residue's deflection angle is small, typically a few degrees, the difference between the total momentum and the parallel momentum is small. The laboratory distributions are broadened by the relativistic $\gamma$-factor, which has to be included in the comparisons with theory.

The principal virtue of this technique for the spectroscopy of rare isotopes is its high sensitivity, which is of paramount importance in experiments aimed at exploring nuclei at the drip lines. This is illustrated in this work, where the results from reactions with an incident $^{19}$C beam intensity of less than one particle per second are presented. The special experimental strength of the technique lies in the high energy of the beam particles and the detection of only the heavy residue. The high energy allows the use of thick targets and gives a strong forward focusing and hence a detection efficiency close to unity. It also allows the secondary beam and "tertiary" fragments to be tracked particle by particle, so that there is essentially no background. There are also important theoretical advantages. The high beam energies allow the use of reaction models, based on the sudden and the eikonal approximations [Tos99b, Hen96], which have high predictive power. These methods can be used to relate the measured single-nucleon removal cross sections to theoretical spectroscopic information using a fixed set of theoretical input parameters, as discussed in detail

in Chapter 3.

The first applications of the knockout reaction method were aimed at clarifying specific features of exotic nuclei that are otherwise well understood, such as the $\ell$–assignments and spectroscopic factors for the presumed proton halo states of $^{26,27,28}$P [Nav98], and the spectroscopic factors linking known states in $^{10,11,12}$Be [Tos99b, Aum00, Nav00], and in $^{13,14}$B [Gui00]. The method was then extended to the neutron-rich carbon isotopes $^{16,17,19}$C about which much less is known. However, they have been the subject of a number of recent theoretical and experimental studies [Baz95, Baz98, Mar96, Rid97, Rid98, Bau98, Ban98, Oza98, Nak99, Sme99, Tos99a, Chu00, Cha00, Des00, Sau00, Kan00]. The validity and accuracy of the method was also tested on the well-known nucleus $^{15}$C. This work will focus on the results obtained on the carbon isotopes. In particular (in agreement with [Nak99]), it will be shown that the $^{19}$C ground state is similar to $^{11}$Be and has a well developed halo.

## 2.2   Experimental setup

The experiments were performed at the National Superconducting Cyclotron Laboratory (NSCL) at Michigan State University, on $^{15,16,17,19}$C, at energies of approximately 60 MeV/nucleon. The radioactive beams were produced by fragmentation of a primary beam on a thick $^9$Be target. The primary and secondary beam characteristics are given in Table 2.1, page 32. These secondary beams were purified in the A1200 fragment separator [She92] by the combination of magnetic analysis and an intermediate degrader. The resulting beam was delivered to the experimental setup shown in Fig. 2.1, consisting of three parts: a dispersion-matching beam line, a target surrounded by an array of position-sensitive NaI(Tl) $\gamma$ detectors [Sch99], and the S800 spectrograph [Cag99], used for detecting the projectile residues from the reaction.

NaI(Tl) array and target

Beam →

Dispersion matched beamline

S800 spectrograph
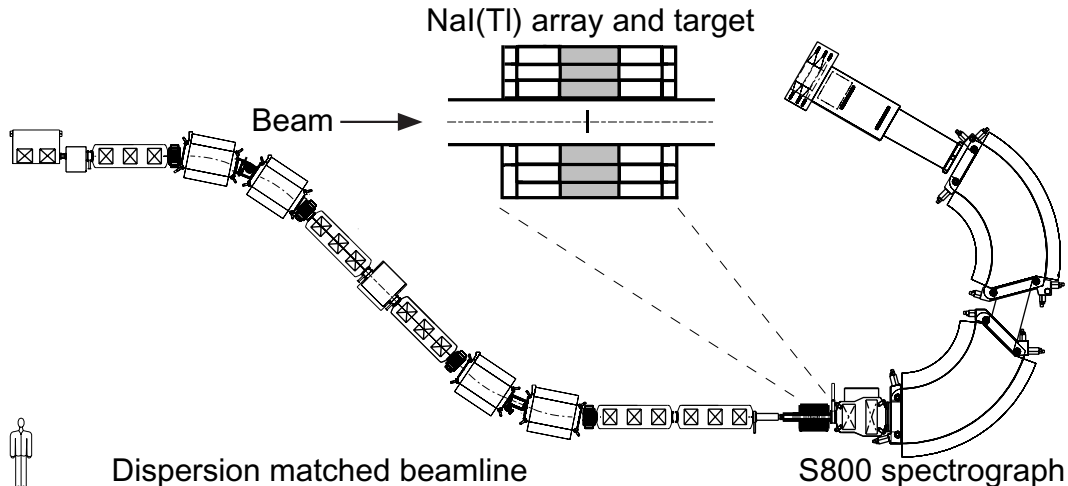
Figure 2.1: Experimental setup. The dispersion-matched beam line delivers a secondary beam of radioactive ions on the target arrangement shown schematically in the inset. The target is surrounded by an array of 38 NaI(Tl) detectors, 20 cm long and 5 cm in diameter, which detect $\gamma$ rays in coincidence with projectile-like fragments measured in the S800 spectrograph.

## 2.3 The S800 spectrograph

Spectrographs are very versatile and their performance can be customized as needed for different experiments. For the experiments discussed in this work, for instance, the technique of single-nucleon knockout reactions described above required the detection of coincident $\gamma$ rays. For this purpose a position-sensitive NaI(Tl) array was placed around the target.

The analysis beamline of the S800 [Cag99] is very similar to the A1200 fragment separator [She92], but with better resolution and larger solid angle acceptance.

Since the A1200 separator has been designed to accept a large momentum bite (up to 3%), a dispersion-matched system was used in order to achieve high resolution. With this technique the spread in incident momentum is compensated by dispersing the secondary beam on the reaction target and using the spectrograph to cancel its dispersion at the focal plane. The S800 spectrograph has been designed to operate in this way. Due to the large dispersion of the S800, the beam must be limited to a

12

spread in relative momentum of 0.5%. In this case, it is possible to study reaction products at a relative momentum resolution of 0.025%.

The spectrograph is characterized by a large angular acceptance, (up to 20 msr solid angle: $\pm$ 5° in the horizontal, $\pm$ 3.5° in the vertical, dispersive direction), and by a momentum acceptance of $\pm$ 2.5%. The position and angles of the fragments are determined by two $x/y$ position-sensitive cathode-readout drift chambers (CRDC) [Yur99] separated by 1 meter at the focal plane of the spectrograph. Immediately following the CRDC's a segmented ionization chamber 41 cm deep and a series of plastic scintillators of different thicknesses (5, 10 and 20 cm respectively) measure the energy loss, total energy and time of flight of the residues, used for particle identification purposes.

## 2.3.1  Cathode Readout Drift Counters

The two CRDC's measured the position coordinates of the fragments at the exit of the spectrograph, providing angle information both in the $x$ (dispersive) and in the $y$ direction. The detectors are filled with 80% $CF_4$ and 20% $C_4H_{10}$ at 140 Torr. The advantages of this gas are low aging deterioration, high drift velocity and low avalanche spread. The detectors have an active area of $30 \times 59$ cm$^2$ and an active depth of 1.5 cm. Along the 59 cm long side (corresponding to the dispersive direction) there are cathode pads separated by 2.54 mm. The principle of operation is analogous to that of a single-wire drift detector. When a charged particle goes through the detector it induces ionization in the gas. A constant vertical electric field drifts the electrons toward an anode wire, where amplification takes place and the charge is collected. The cathode pads placed in front of and behind the anode wire collect the positive charge induced by the anode. The position $x$ is then taken as the centroid of the Gaussian fit of the charge distribution. The position along the $y$ direction is

obtained from the drift time of the electrons to the anode wire. Typical drift times are of the order of 0-20 $\mu$s, while the response time from the scintillators is 3-4 orders of magnitude smaller. The drift time can then be measured as the time between the scintillator signal and the anode wire signal, from which the $y$ position can be deduced. The resolution in both the $x$ and $y$ position was about 0.3 mm, tested with a beam of $^{22}$Ne at 80 MeV/u. Since the S800 momentum dispersion is 9.6 cm/% and the S800 has been designed to have a momentum resolution of 1 part in 20,000, a position resolution of better than 0.48 mm is necessary and the two CRDC's are thus well suited.

The calibration of the detectors is done by inserting a mask with holes and slits in front of the detectors, exposed to the beam particles. The known positions of holes and slits provide $y$ calibration points, while the $x$ position is calibrated using the known spacing between each pad.

**Trajectory reconstruction**

The measured coordinates of the fragments at the focal plane were the input for the code COSY INFINITY to reconstruct the trajectory of the fragments and obtain their position before entering the spectrograph after the reaction. As the particles pass through the magnetic elements of the spectograph their positions change, due to the action of the magnetic fields. If the magnetic fields are known at all points, the trajectory of the ions passing through is governed by the Lorentz force law $d\mathbf{p}/dt = q(\mathbf{E} + \mathbf{v} \times \mathbf{B})$ and can be thus calculated analytically, as a matrix transformation from the inital to the final coordinates. In the particular configuration of the S800, the four coordinates $(x_f, \theta_f, y_f, \varphi_f)$ measured at the focal plane (position and angle in the dispersive and non-dispersive directions, respectively) can be expressed as a transformation of the coordinates at the target position $(\theta_t, y_t, \varphi_t, \delta_t)$, where $\delta$ is the

14

fractional kinetic energy difference from the central ray, $\delta = (E - E_0)/E_0$, through a matrix S, i.e.,

$$
\begin{bmatrix} x_f \\ \theta_f \\ y_f \\ \varphi_f \end{bmatrix} = S \begin{bmatrix} \theta_t \\ y_t \\ \varphi_t \\ \delta_t \end{bmatrix}
$$

This assumes that the initial spot size in the dispersive direction $x$ is small and approximated to zero. To reconstruct the particle coordinates at the target position from the knowledge of the coordinates at the focal plane an inversion procedure is needed. This is rather complicated because the matrix S is not invertible. However, the code COSY INFINITY [Ber93] has been developed for this purpose, including third order optics and all optical aberrations. The code calculates the inverse matrix R, such that:

$$
\begin{bmatrix} \theta_t \\ y_t \\ \varphi_t \\ \delta_t \end{bmatrix} = R \begin{bmatrix} x_f \\ \theta_f \\ y_f \\ \varphi_f \end{bmatrix}
$$

and it can be used to deduce energy and angles in the target chamber.

## 2.3.2 Ionization Chamber

The ionization chamber is a standard Frisch Gridded Ion Chamber segmented into 16 one-inch anodes perpendicular to the ions' trajectory. The chamber is filled with P-10 (90% argon and 10% methane) at 300 Torrs. This detector provides precise $Z$ identification up to $Z \simeq 50$ [Yur99].

### 2.3.3 Scintillation Detectors

The scintillation detectors provide energy loss, total energy and timing information. The first one is also used as the exit window of the ionization chamber, with the advantage of reducing the straggling normally associated with an exit window. The timing information is derived from the signals of the photomultipliers at each end of each scintillator. The time resolution obtained for a test beam of $^{16}$O at 60 MeV/u was 160 psec FWHM.

### 2.3.4 Particle Identification

Although the radioactive beams produced by in-flight fragmentation were purified in the fragment separator A1200, where the magnetic settings were chosen to allow for the transport of mainly the isotope under investigation, not always all the contaminants could be eliminated by the magnetic analysis. Therefore, particle identification was the first important step in the data analysis. For this purpose a series of different gates on the measured variables was determined. First of all, the data corresponding to the setting of the spectrograph adjusted to the full beam momentum were analyzed to identify the beam particles of interest. This was done by selecting the events with the appropriate coordinates in the energy loss ($\Delta E$) vs. time of flight ($TOF$) plane, where particles occupy specific regions depending on their mass and charge. The energy loss information was given by the ionization chamber, while the time of flight was measured between the first scintillator and a beam-line timer (BLT), a scintillator placed at the end of the A1200 separator. The signal from the first scintillator was also the trigger condition for the data acquisition. Therefore, the BLT signal was delayed and, as a result, the $TOF$ appears reverted, so that an increase in $TOF$ corresponds to an increase in velocity. As an example, the plot observed for the case

of a beam of $^{16}$C is shown in the top panel of Fig. 2.2. The $^{16}$C beam particles occupy the central part of the plot and were selected using the gate drawn. The contaminants at the left and at the right of $^{16}$C were $^{14}$B and $^{18}$N, respectively.

To identify the residues from the reaction, the magnetic field of the spectrograph was scaled by a factor (A-1)/A to take the smaller mass of the residues into account. With this setting, the fragments had the same time of flight as the incident beam, because the removal of one neutron from each beam particle left the fragment velocity essentially unchanged. This allowed a simple identification of the fragments from the reaction by just gating on the same region of the $\Delta E$ vs. $TOF$ plane, occupied by the beam particles with the previous settings, as shown in the lower panel of Fig. 2.2. Moreover, since the $TOF$ is directly proportional to the ratio A/Z, the groups of fragments immediately below the $^{15}$C residues could be identified as $^{13}$B and $^{12}$B, while the lower group of fragments corresponds to $^{10}$Be. Analogously, the groups of particles below $^{17}$N are $^{15}$C and $^{14}$C fragments produced in reactions on the $^{18}$N beam contaminant.

However, other conditions were necessary to select only the events of interest, as obvious from the bottom panel of Fig. 2.2. Events satisfying the first gate included also (slower) beam particles scattered in the S800, which needed to be excluded. These appear at smaller $TOF$ and higher $\Delta E$ in the left part of the gate drawn in the bottom plot of Fig. 2.2. A clear differentiation was possible using the $TOF$ vs. $x$ (dispersive position) information for each of the two CRDC detectors. The gates used for $^{16}$C are shown in Fig. 2.3. Similar gates were defined for the other carbon isotopes.

The intensities of the beams and residues, obtained using the gates discussed above, were normalized using the signals of the BLT scintillator, placed at the end of the A1200. The cross sections for one-neutron removal reactions were calculated as the

17
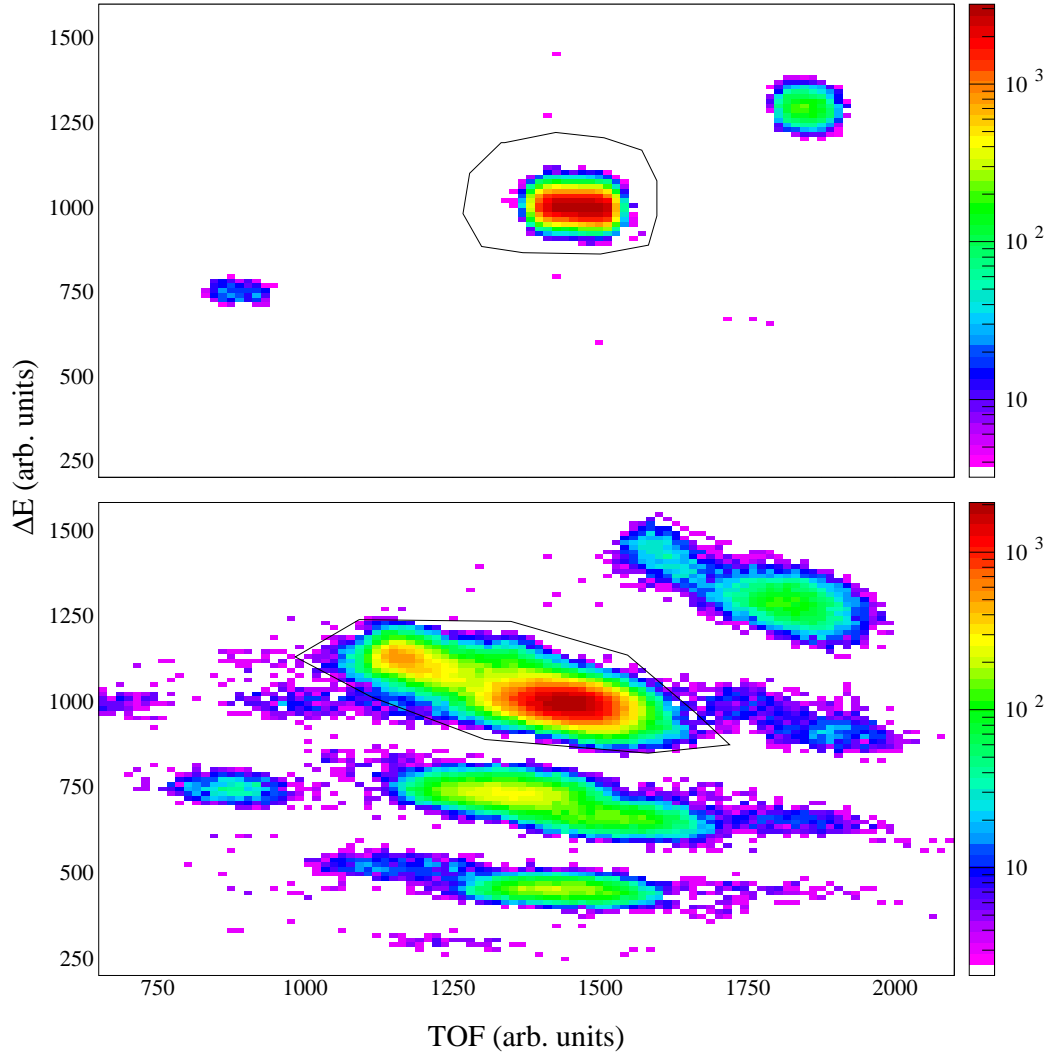
Figure 2.2: Energy loss ($\Delta E$) vs. Time of Flight ($TOF$) spectra for two different field settings. The top plot was obtained with the spectrosgraph adjusted to the momentum of the $^{16}$C beam particles, identified by the gate drawn. The contaminants $^{14}$B and $^{18}$N (left and right, respectively) were also present. The bottom plot was obtained at a reduced magnetic field to identify the $^{15}$C reaction residues from $^{9}$Be($^{16}$C,$^{15}$C)X, selected by the gate drawn. (See text for details on the identification of the other fragments which appear in the plot.)
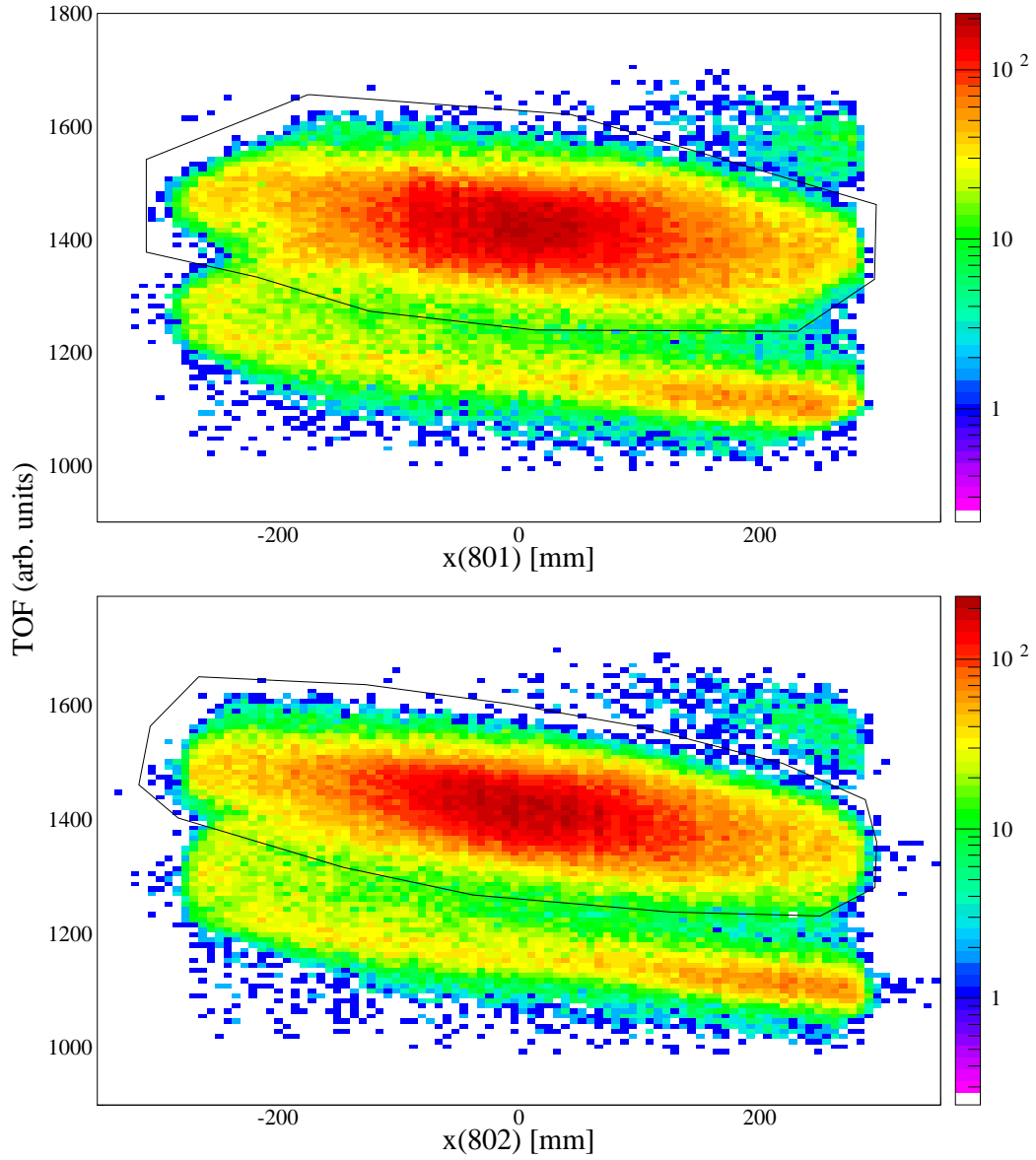
Figure 2.3: Time of flight vs. $x$, position in the first (top) and in the second (bottom) CRDC for $^9\text{Be}(^{16}\text{C},^{15}\text{C})\text{X}$. The scattered beam particles included in the gate drawn in the bottom plot of Fig. 2.2 can be well identified and separated from the $^{15}\text{C}$ residues (selected with the gates drawn).

rate of detected fragments divided by the rate of incident projectiles and taking into account the thickness and number density of the $^9$Be target, as well as the electronics dead time. Details on the derivation of the cross section for each individual isotope are given in Appendix A.

## 2.4   The NaI array

The excited states of the residues were detected by an inner ring of 11 cylindrical position-sensitive NaI(Tl) scintillators [Sch99] surrounding the target, as illustrated in Fig. 2.1. The complete array has a total of 38 detectors with 27 arranged in two outer rings. However, only a marginal improvement of the peak to background intensity was gained when the outer detectors were included in the analysis, therefore these were not used.

Each scintillator was read out by two photomultiplier tubes, one at each end, thus allowing for the determination of both the energy and the interaction point of the photon in the detector. This was possible because the measured light outputs $E_{1,2}$ from the two photomultipliers at each end depend on the interaction point as $E_{1,2} \propto E e^{-\mu(\frac{L}{2} \pm x)}$, where $x$ is the interaction point from the center of the scintillator, $\mu$ is the attenuation coefficient, $L$ is the detector length and $E$ is the total energy deposited. Therefore, the total energy $E$ and the position $x$ can be obtained as $E \propto \sqrt{E_1 E_2}$ and $x \propto \log(E_1/E_2)$, respectively.

A collimated $^{60}$Co source was used for the position calibration. The collimator consisted of two heavy met (95% tungsten, 3.5% nickel and 1.5% copper) cylinders arranged coaxially with a 4.6 mm gap in between, where the source was placed. A long ruler attached to the collimator served as a handle to insert the source inside the beam pipe and to read the actual position at which the source was placed. The

source was moved in steps of 1/4 inch, and for each position data were recorded on tape for 5 minutes. For each detector the reconstructed position was plotted in function of the position read from the ruler and the data were fitted with a polynomial of order 3, to accurately describe the non-linear behavior at the edges of the scintillators. The polynomial was finally inverted and used to extract the calibrated position information from the recorded light signals.

For the energy calibration different sources of known energies were used, covering a wide range of energies. More precisely, $\gamma$ rays of 0.511 and 1.274 MeV from $^{22}$Na, of 0.898 and 1.836 MeV from $^{88}$Y and of 0.239, 0.583 and 2.614 MeV from $^{228}$Th were used. The data for each source were recorded for about 2-6 hours. A position-dependent energy calibration of the energy spectra was derived at ten different points along the detectors in the direction parallel to the beam.

The position information provided by the array made it possible to correct for the Doppler shift in the energy of the $\gamma$ rays emitted by the fast ($\beta \simeq 0.34$) residues. This is illustrated in Fig. 2.4, where the energy dependence on the angle disappears after the correction.

The back transformation to the center of mass system (c.m.), however, does not generate the spectrum that would have been observed from a source at rest, due to events in which radiation has escaped from the crystal. Examples of these are annihilation radiation and Compton-scattered photons. Since the reconstruction cannot identify these features, the part of the response function that does not belong to the full-energy peak gets smeared. This may seem unimportant since the full-energy peaks obviously are reconstructed correctly. However, an accurate understanding of the measured envelope of the $\gamma$ spectrum requires knowledge also of the shape of the continuum distributions underlying the peaks. For the decomposition of the measured

21
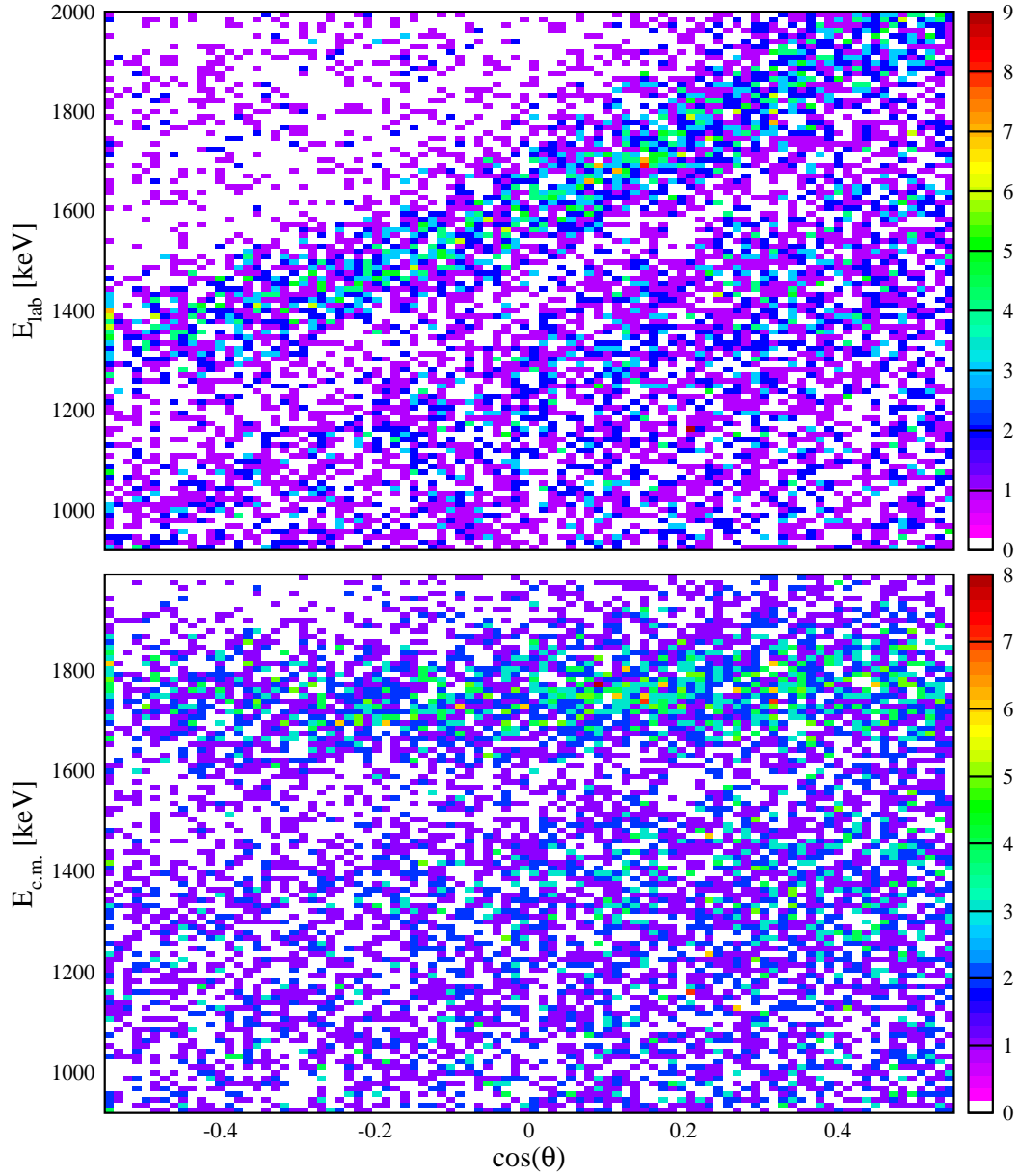
Figure 2.4: γ-ray energy E$_{lab,c.m.}$ vs. cos(θ) before (E$_{lab}$, top) and after (E$_{c.m.}$, bottom) Doppler correction of the γ rays from the deexcitation of the $^{16}$C residues produced in one-neutron removal reactions on $^{17}$C.

spectrum, complete response functions were constructed in a numerical simulation.

## 2.4.1  Simulations

For a $\gamma$ ray of a given energy, assumed to be isotropically emitted in the c.m. system, a sequence of Lorentz-boosted $\gamma$ events with the appropriate angular distribution was generated in a Monte Carlo procedure. These were subsequently used in the Monte Carlo code GEANT [Gea94], which simulated the energy deposited in the detectors as well as losses generated by interactions with chamber walls and detector mounts. One million primary $\gamma$ rays were generated for a given energy. For each event the (random) outcome was randomly folded with the energy resolution, which was assumed to scale with the square root of the energy and was fixed to the measured resolution corresponding to a full width at half maximum (FWHM) of 7.5% at 1.33 MeV. Based on the observed spatial resolution of 1.5 cm FWHM, the sequence of simulated $\gamma$ signals was corrected event by event for the Doppler shift to construct the apparent energy in the c.m. system. Histograms of the simulated events created the reference line shapes. The resulting shapes were approximated by smooth analytical curves (to eliminate statistical fluctuations from the Monte Carlo procedure) and were used for fitting the observed spectra. Examples of these fits will be encountered in Chapters 4 and 5.

The reliability of the simulations had been previously verified by comparing measured and simulated $\gamma$-ray spectra from (necessarily stationary) calibration sources. An agreement to within 10% in the absolute intensity was found. As an example, the measured and simulated spectra from the calibration source of $^{88}$Y are plotted in in Fig. 2.5. Noting that the data include also natural background, the comparison between the two spectra shows a remarkable agreement.
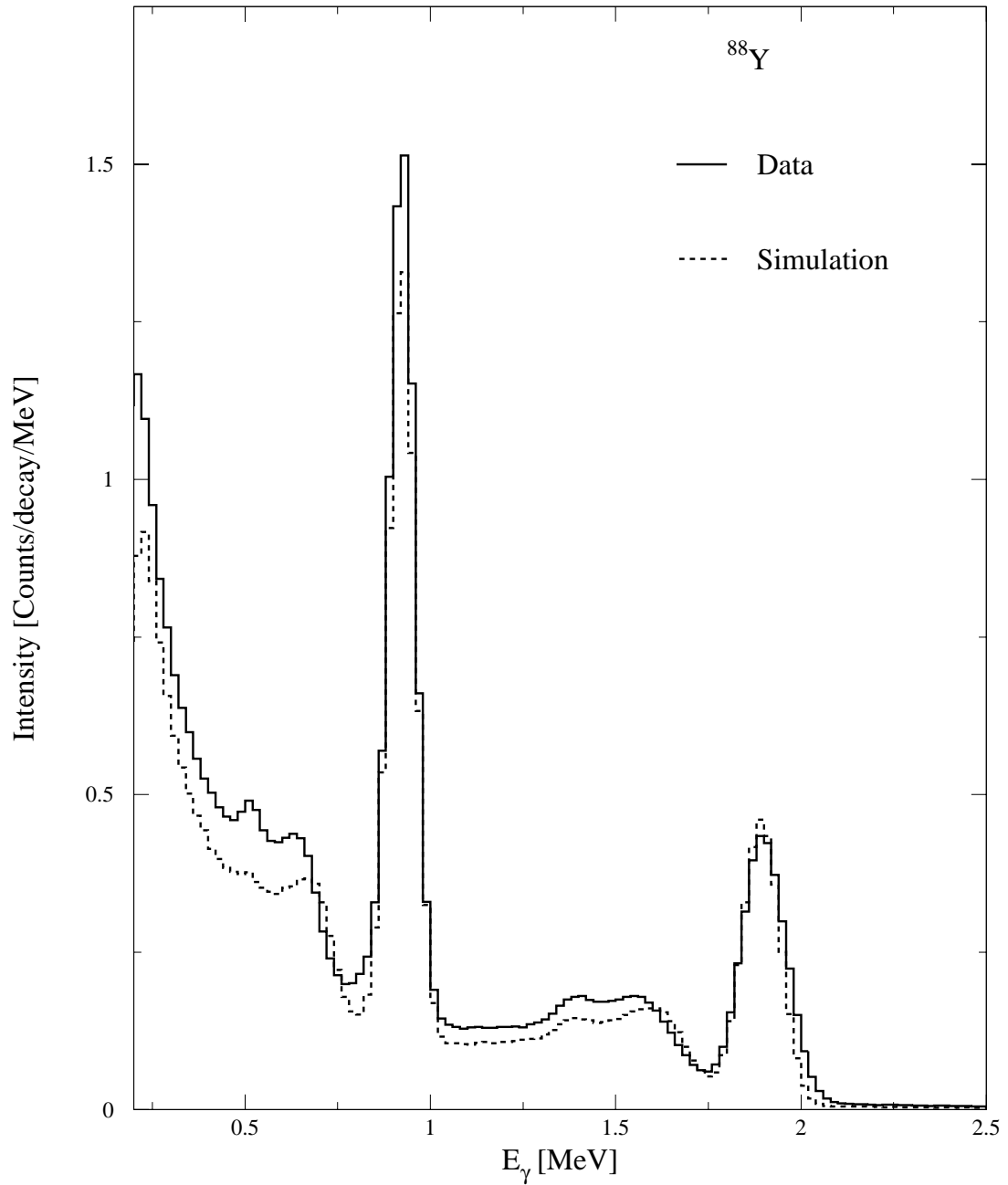
Figure 2.5: Measured and simulated $\gamma$-ray energy spectra for the $^{88}$Y source, normalized to the number of $\gamma$ rays emitted during the electronics live time. The observed deviations between data and simulation are attributed to the natural background.

## 2.4.2    Analysis of the measured $\gamma$-ray spectra

For each event the $\gamma$ rays detected by each of the 11 scintillators were recorded and Doppler-corrected. Since the events are expected to be equally distributed around the axis of the NaI(Tl) array, only one $\gamma$-ray spectrum was analyzed, obtained by adding the spectra from the individual 11 detectors. The procedure to obtain the final spectrum was the following. Since over 99% of the detected fragments was associated with a multiplicity of $\gamma$ rays $m_\gamma \leq 3$ in the first ring of NaI(Tl) detectors, the hits were sorted according to their energy and only the three highest energy hits were retained. This reduced the number of variables from 11 (one energy per each detector) to 6 (detector number and energy for the three highest energy hits measured in each event), producing a data file essentially equivalent to the original, where the data were just sorted differently. The final spectrum was obtained by summing the three spectra corresponding to the three highest energy hits. In this particular case, this was equivalent to the spectrum that would have been obtained by summing the 11 spectra from the individual detectors.

An alternative procedure to analyze the $\gamma$-ray spectra would be the add back of the energies event by event. In the add back, since the Doppler effect acts only on the primary $\gamma$ ray, while it does not affect secondary $\gamma$ rays (from Compton scattering, for example), the energies should be summed before applying the Doppler correction and the resulting energy should be corrected using the angle of the primary (usually the one with the highest energy) $\gamma$ ray. However, the situation becomes more complicated if for each event more than one $\gamma$ ray is produced (i.e., if the excited residues decay to the ground state via a cascade of two or more $\gamma$ rays). In that case an unambigous identification of primary and scattered $\gamma$ rays is not possible. These considerations led to the choice of the first procedure. For a quantitative analysis, the same procedure

was applied to the simulated spectra.

A complication in the data analysis was the presence of a continuum distribution varying approximately exponentially with energy. This was attributed to neutrons, $\gamma$ rays and charged particles produced in the target and to their secondary interactions with construction materials and the scintillators. This distribution has been seen consistently in previous experiments [Nav98, Aum00, Gui00, Nav00] with an intensity, for $\gamma$ energies above 0.25 MeV, of approximately 9% per outgoing fragment. Although it reduces the sensitivity to detect weak transitions (the $^{17}$C analysis shows an example of this, section 5.2.3), it does not significantly interfere with the determination of the $\gamma$-ray energies and intensities.

In particular, accurate estimates of this continuum could be obtained by comparing the $^{12}$Be and $^{16}$C data. In both cases only one $\gamma$ ray of energy 0.32 and 0.74 MeV, respectively, was observed. At energies higher than 1 MeV the two spectra (both in the laboratory system and in the c.m.), normalized to the number of outgoing fragments, agree in shape and intensity to within 15%. This is shown in Fig. 2.6.

By averaging the $^{12}$Be and $^{16}$C data, two experimental continuum distributions for $E_\gamma > 1$ MeV were obtained, one in each reference system. The two distributions were compared and found to be equivalent, as demonstrated by Fig. 2.7.

It will be seen in Chapter 5 that the result for the exponential continuum obtained from the fit of the $\gamma$-ray spectrum measured in coincidence with $^{16}$C residues from reactions on $^{17}$C, was consistent with the measured distribution.

The assumption on the origin of the continuum distribution as mainly arising from reactions induced by the neutrons removed from the beam is demonstrated by the observed angular distributions of the $\gamma$ rays in the laboratory and in the c.m. systems. As shown in Fig. 2.8, the $\gamma$ rays of the continuum distribution measured
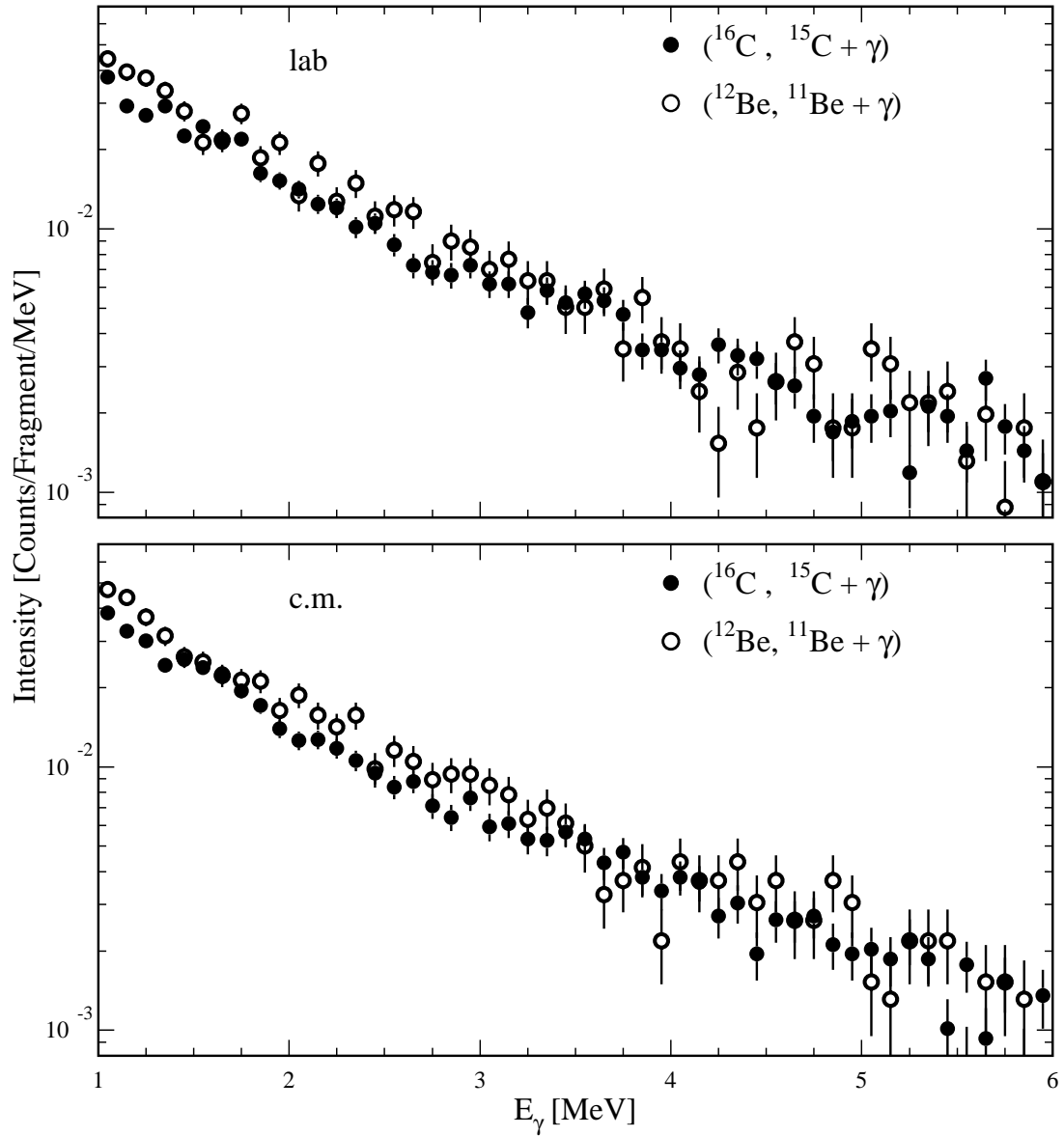
Figure 2.6: Experimental laboratory (top) and c.m. (bottom) $\gamma$-ray spectra from the residues $^{11}$Be and $^{15}$C for $E_\gamma > 1$ MeV.
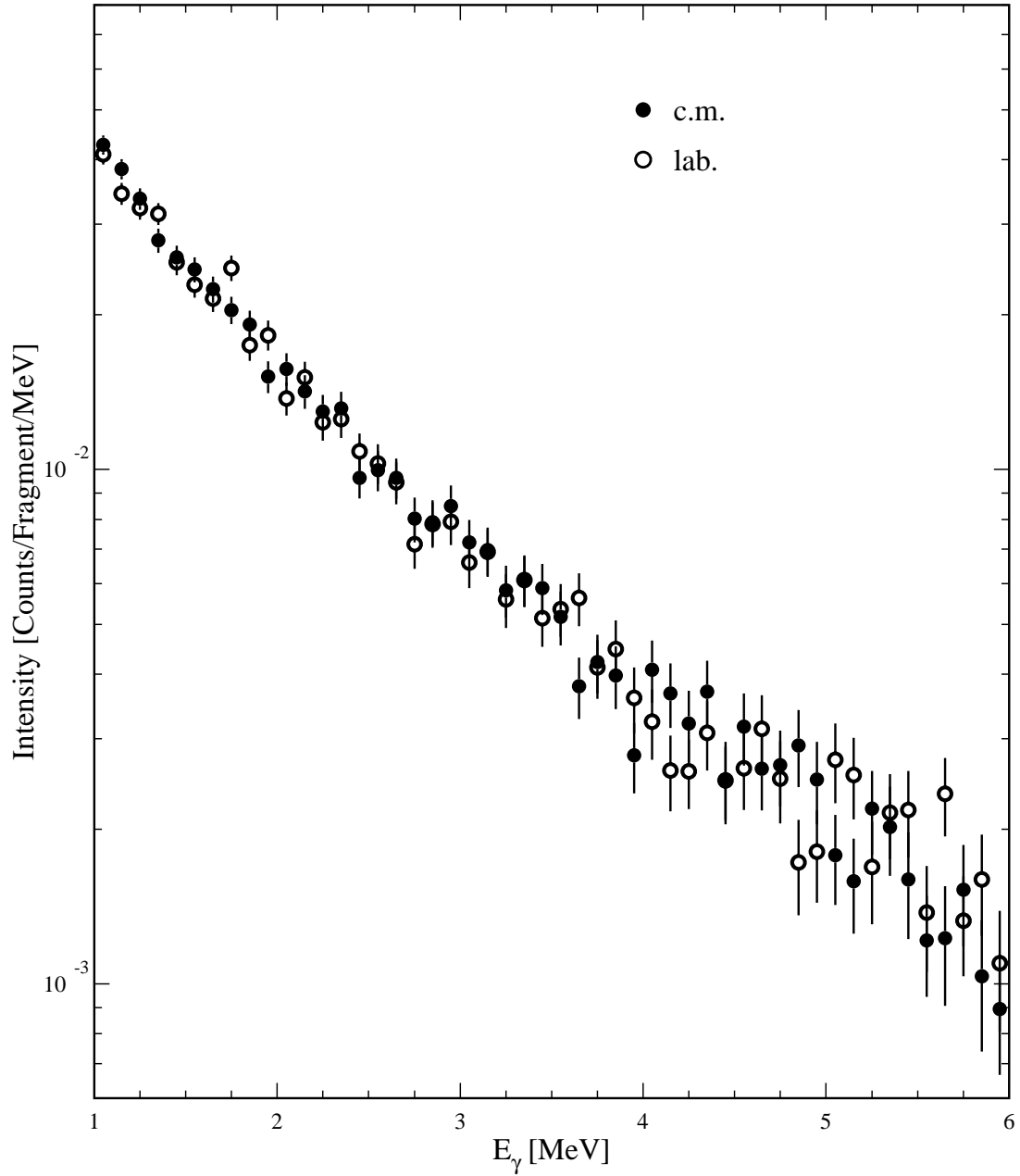
Figure 2.7: Experimental c.m. (full dots) and laboratory system (open dots) $\gamma$-ray spectra representing the continuum distribution lying beneath the measured $\gamma$-ray spectra for $E_\gamma > 1$ MeV. The two spectra were obtained as an average of the $^{12}$Be and $^{16}$C data.

from $^{16}$C appear focused forward in the laboratory system.

A study of the angular distribution of $\gamma$ rays from the residues was also performed, to investigate whether the possible alignment in the fragments could be identified. The angular distribution of the $\gamma$ rays emitted by excited fragments which are not aligned is expected to be isotropic. However, this was found [Han00] to be the case also when the fragments have some degree of alignment. In fact, for the cases of $^{15}$C and $^{17}$C, using the calculated cross sections for fully aligned states as weights for the angular distributions characteristic of each projection of the angular momentum, the resulting angular distributions are isotropic. The angular distributions of the $\gamma$ rays emitted by the $^{14}$C and $^{16}$C residues in their first excited state (most populated in both cases) were obtained and show a forward focusing in the laboratory system, while in the c.m. they are isotropically distributed. The measured angular distributions were then compared to the distributions predicted by the simulation of the 6.09 MeV and 1.77 MeV $\gamma$ rays, respectively. As an example, Fig. 2.9 shows that the angular distribution obtained from the $^{17}$C data, corresponding to the decay of the $^{16}$C fragments in the laboratory system presents the same behavior as the simulated one.

## 2.5   The experiments

The $^{15,16,17,19}$C reacted on a 228 mg/cm$^2$ $^9$Be target. The characteristics of the incident $^{15,16,17,19}$C beams are listed in Table 2.1. The secondary beam energy is the average energy at the target mid-plane.
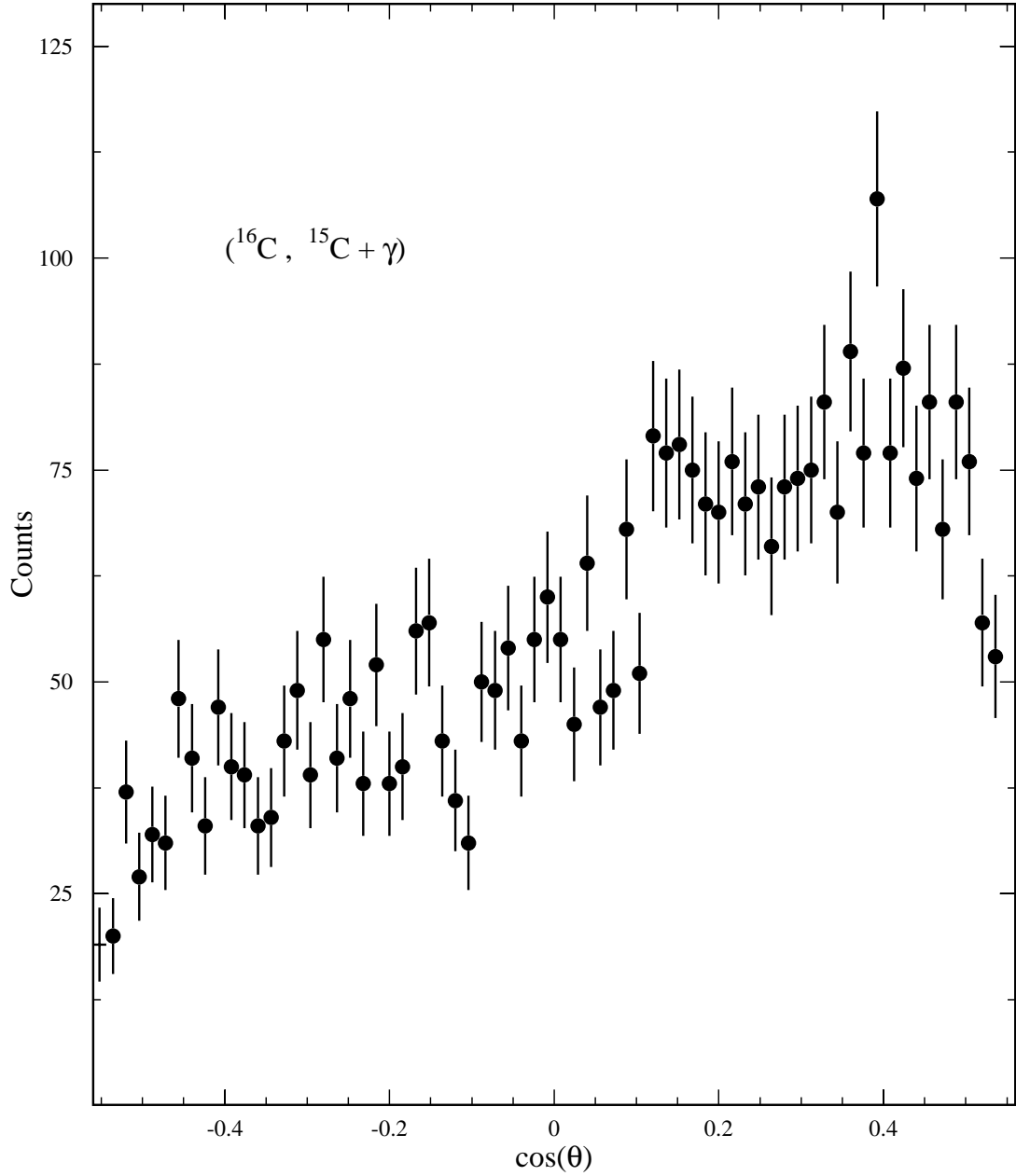
Figure 2.8: Experimental laboratory system angular distribution of the $\gamma$ rays with $E_\gamma > 1.2$ MeV measured from one-neutron removal reactions on $^{16}$C. The distribution is focused at forward angles, demonstrating the origin of the continuum distribution from interactions induced by the neutrons removed from the beam.
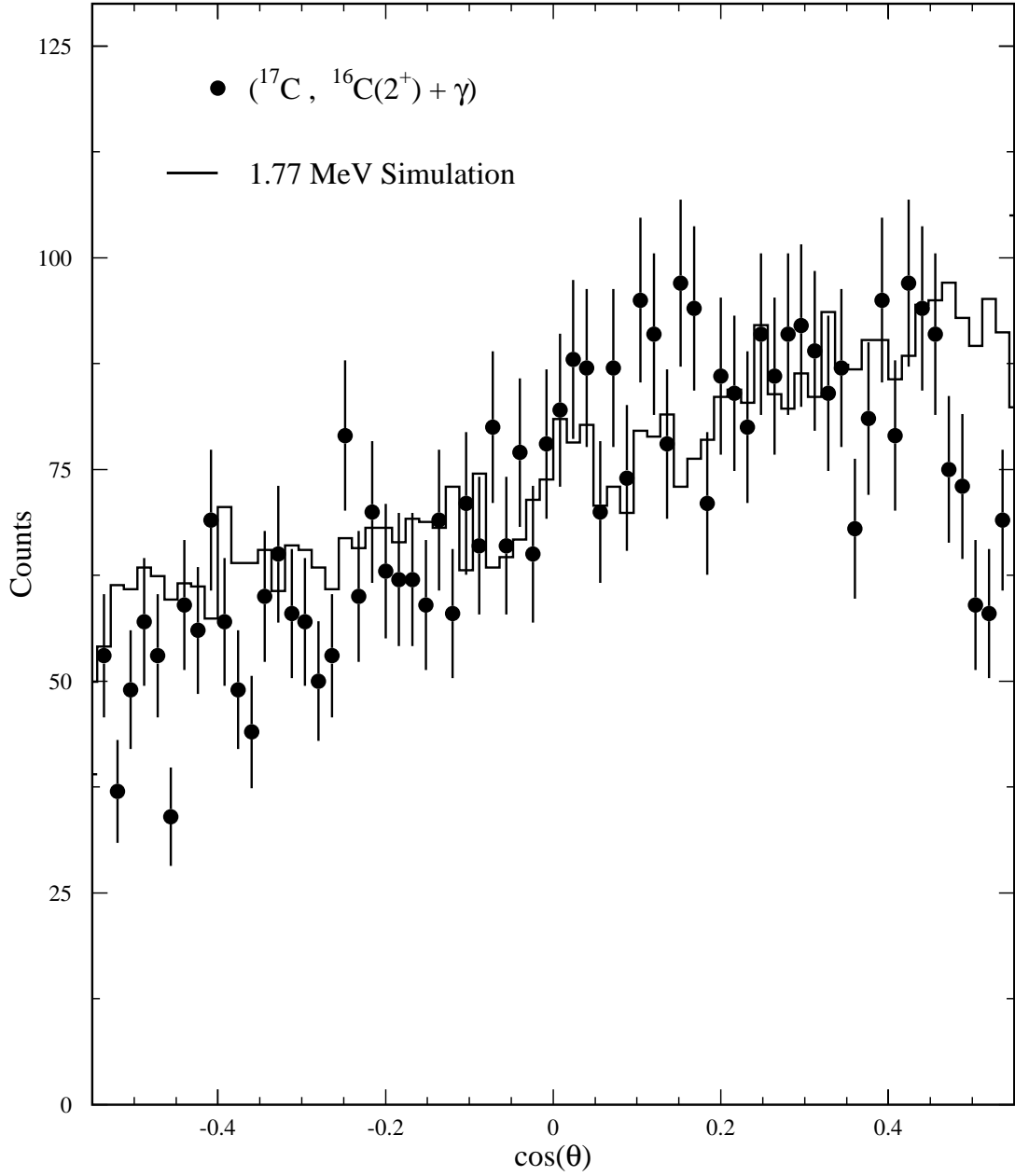
Figure 2.9: Experimental laboratory system angular distribution of the $\gamma$ rays with $1.6 < E_\gamma < 2.0$ MeV, corresponding to the decay of the $^{16}$C fragments, produced in one-neutron removal reactions on $^{17}$C, from the $2^+$ state at 1.77 MeV to the ground state. The solid line is a simulation of the angular distibution of Lorentz-boosted $\gamma$ rays of 1.77 MeV.

Table 2.1: Experimental parameters and settings.

| Primary beam | $^{18}$O | $^{22}$Ne | $^{22}$Ne | $^{22}$Ne | $^{22}$Ne |
|---|---|---|---|---|---|
| Intensity of primary beam [pnA] | 330 | 330 | 330 | 330 | 330 |
| Energy of primary beam [MeV/nucleon] | 80 | 80 | 80 | 80 | 80 |
| Secondary beam | $^{15}$**C** | $^{16}$**C** | $^{17}$**C** | $^{19}$**C** | $^{19}$**C** |
| Intensity of secondary beam [particles/sec] | 90 | 310 | 230 | 0.5-1 | 0.5-1 |
| Energy of secondary beam [MeV/nucleon] | 54 | 62 | 62 | 57 | 56 |
| Secondary target | $^{9}$Be | $^{9}$Be | $^{9}$Be | $^{9}$Be | $^{197}$Au |
| Target thickness [mg/cm$^2$] | 228 | 228 | 228 | 228 | 518 |
| Data acquisition time | 3.5 h | 6 h | 18 h | 3 d | 1 d |
| Main beam impurities | - | $^{14}$B, $^{18}$N | $^{15}$B, $^{19}$N | $^{18}$C | $^{18}$C |

# Chapter 3

# Theoretical Analysis

Knockout reactions have been often used for spectroscopic studies of neutron-halo nuclei [Han95], where the large cross sections and narrow momentum distributions observed in the breakup of neutron halo systems provided evidence for the large size of the halo. It was shown by Bertsch et al. and others [Ber90, Yab92, Hen96] that the eikonal approximation, previously used for nucleon-nucleus scattering at high energies, gave a good description of the cross sections for such reactions on light targets. From this also follows that the outgoing fragment's longitudinal momentum distribution reflects the momentum content of the wave function in the volume sampled by the projectile's interaction with the target [Han95, Han96, Hes96]. The cross sections and momentum distributions are very sensitive to the angular momentum and separation energy of the nucleon in the initial state.

More recently it has been shown that there are also appreciable cross sections for the removal of a nucleon from the occupied non-halo single-particle states in the projectile. An example of this is furnished by the light phosphorus isotopes, where the knockout of the halo proton from the ground state constitutes only 30-55% of the total measured knockout cross section [Nav98]. Even for the very pronounced single-neutron halo nucleus $^{11}$Be, one finds by comparing the original inclusive exper-

iment [Kel95] on the $^9\text{Be}(^{11}\text{Be}, ^{10}\text{Be})\text{X}$ reaction at 66 MeV/nucleon with the exclusive measurement with $\gamma$ rays in coincidence [Aum00], that 22% of the cross section populates excited levels of the $^{10}\text{Be}$ residues. The momentum distributions of the heavy residues arising from knockout from deeply bound states can be calculated using the same techniques as for the halo states.

Similarly, extending the eikonal approximation as applied to halo nucleus ground states to treat the removal of a non-halo nucleon from the initial state, the cross section $\sigma_{th}(I^\pi)$ for populating a given final state $I^\pi$ of the residue or core, may be written [Tos99b] as

$$\sigma_{th}(I^\pi) = \sum_j C^2 S(I^\pi, n\ell j)\sigma_{sp}(S_n, n\ell j). \tag{3.1}$$

Here $C^2 S$, the spectroscopic factor for removal of a nucleon with given single-particle quantum numbers $(n\ell j)$, expresses the parentage of this configuration in the initial state with respect to the specific state $I^\pi$ of the remaining nucleons. Following nucleon removal this is assumed to be the final state of the residue, which is therefore assumed to behave as a spectator particle and to interact at most elastically with the target [Hus85]. The sum in Eq. (3.1) is taken over all configurations which have a non-vanishing parentage. The $\sigma_{sp}$ are the single-particle removal cross sections, which are strongly dependent on the orbital angular momentum $\ell$ and the neutron separation energy $S_n$. The calculation of these quantities is discussed below.

The approach of the present work and its predecessors [Nav98, Aum00, Nav00, Gui00] has been adopted in recent work by Sauvan et al. [Sau00], who have measured inclusive one-neutron removal cross sections and momentum distributions for 23 nuclei in the $p - sd$ shell. The results are in good agreement with calculations based on techniques that are essentially identical to those used here. In particular, the results for the inclusive absolute cross sections suggest that the method may actually be more

accurate than the $\pm 20\%$ conservative estimate proposed in the following. It is also interesting to compare this and our results with the measurements of charge-changing cross sections ($\sigma_{cc}$) reported by Chulkov et al. [Chu00]. In their analysis they obtain total neutron-removal cross sections $\sigma_{-xn}$ by taking the difference between interaction cross sections $\sigma_I$ and $\sigma_{cc}$. While the $\sigma_I$ and $\sigma_{cc}$ can be discussed in terms of global density distributions, Chulkov et al. find that the $\sigma_{-xn}$ show a more complicated behavior suggesting the influence of nuclear structure effects. The present work shows how these can be accounted for in the one-neutron removal channel through the use of spectroscopic factors calculated from a many-particle wave function. An example of how these effects can show up in the two-neutron removal channel is offered by our recent experiment on $^{12}$Be [Nav00], where a sizeable fraction of the one-neutron removal cross section populates the unbound $0d_{5/2}$ state in $^{11}$Be.

## 3.1   Theory of the spectroscopic factors of $^{15,16,17,19}$C

A number of recent papers cited above have discussed the properties of the heavy carbon isotopes within the framework of particle-core-coupling models, cluster models and global density distributions. Although such models provide qualitative insight into the structure and resulting cross sections of the ground states, they do not furnish a unified description of all states. Shell-model calculations have been used instead. The natural shell-model space for these nuclei is the complete set of basis states spanned by the neutrons in $1s_{1/2}$, $0d_{5/2}$ and $0d_{3/2}$ ($sd$–shell) orbits together with protons in $0p_{3/2}$ and $0p_{1/2}$ ($p$–shell) orbits.

The Hamiltonian for the neutrons in the $sd$–shell is well established by Wildenthal's USD interaction [Bro88]. The $p$–shell Hamiltonian is also well established [War92]. The proton-neutron ($p - sd$) part of the Hamiltonian is based upon the

work of Warburton and Brown [War92]. They considered all of the known data (165 levels) in the mass region $A = 10 - 20$ which could be associated with the $p - sd$ Hamiltonian. Among the 165 energy-level data considered were those of $^{15}$C: $\frac{1}{2}^+$ and $\frac{5}{2}^+$; $^{16}$C: $0^+$, $2^+$, $3^+$, and $4^+$; $^{17}$C: $\frac{3}{2}^+$; $^{18}$C: $0^+$ and $2^+$; and $^{19}$C: $\frac{1}{2}^+$.

Two types of $p - sd$ Hamiltonians were developed: (1) WBT, modeled on a set of two-body matrix elements (TBME) obtained from a bare G matrix, and (2) WBP, modeled on a one-boson exchange potential (OBEP) which includes the one-pion exchange potential (OPEP) (fixed at its known strength) and a long-range (monopole) interaction. For WBT, 28 linear combinations of the 95 $p - sd$ TBME were adjusted to fit the data. For WBP, ten parameters associated with the strength of the OBEP terms were varied. The root mean squared (rms) energy deviations for the 165 $p - sd$ data were 389 keV for WBP and 330 keV for WBT. Comparisons between the predictions made with WBP and WBT will give an indication of the theoretical error in these type of calculations. WBP is an evolution of the Millener-Kurath potential model for the $p - sd$ interaction which was developed earlier [Mil75].

The WBP and WBT interactions have been used to predict many properties of nuclei in the $A = 10 - 20$ mass region [Bro95, Bro98, Aum00, Nav00]. In general, the wave functions and spectroscopic properties with WBP and WBT are similar, but there are differences in the energy-level ordering, especially when the levels are spaced more closely than the 350 keV rms deviation established in their derivation. In the present context, the calculations provide both level energies and the required spectroscopic factors $C^2S$. These are presented in Tables 4.2, 5.1, 5.2, 5.3, and 5.4, and discussed in detail in Chapters 4 and 5.

For both $^{17}$C and $^{19}$C theory predicts a triplet of low-lying levels with spin-parity $\frac{1}{2}^+$, $\frac{3}{2}^+$ and $\frac{5}{2}^+$. The ordering of these levels differs between WBP and WBT. WBP

gives for $^{17}$C: $\frac{3}{2}^+$ (ground state), $\frac{5}{2}^+$ at 0.03 MeV and $\frac{1}{2}^+$ at 0.30 MeV; and for $^{19}$C: $\frac{1}{2}^+$ (ground state), $\frac{5}{2}^+$ at 0.19 MeV and $\frac{3}{2}^+$ at 0.62 MeV. WBT gives for $^{17}$C: $\frac{5}{2}^+$ (ground state), $\frac{3}{2}^+$ at 0.08 MeV and $\frac{1}{2}^+$ at 0.27 MeV; and for $^{19}$C: $\frac{5}{2}^+$ (ground state), $\frac{1}{2}^+$ at 0.5 MeV and $\frac{3}{2}^+$ at 0.40 MeV. The present experimental results give $\frac{3}{2}^+$ for the $^{17}$C ground state and $\frac{1}{2}^+$ for the $^{19}$C ground state. Thus the WBP interaction is favored in this respect. However, it does not rule out WBT since the required levels associated with the experimental spins are within the nominal 350 keV deviation expected. Details about the wave functions will be discussed in Chapters 4 and 5. The WBP interaction will be used for the spectroscopic factors. Generally, the spectroscopic factors obtained for WBP and WBT are very similar, and any important differences will be discussed. The spectroscopic factors between the low-lying positive parity states are related to pickup from $s-$ and $d-$orbitals. Pickup from the $p-$orbitals leads to negative parity states at excitation energies above the neutron-decay threshold in all the carbon isotopes studied in this work, with the exception of $^{15}$C, for which they are observed in the present experiment.

## 3.2   Theory of the single-particle cross sections

The cross sections $\sigma_{sp}$ in Eq. (3.1) were calculated in the eikonal model [Tos99b]. The same input parameter set was used as in the reported analyses of Refs. [Nav98, Aum00, Gui00, Nav00]. The calculation of each single-particle cross section assumes that the removed nucleon is described by a normalized single-particle wave function with quantum numbers $(n\ell j)$ moving with respect to the core of remaining nucleons in state $c \equiv I^\pi$. Such configurations are written $|\phi^c_{JM}\rangle$, where $J$ is the magnitude and $M$ the projection of the projectile's ground-state total angular momentum, $\vec{J} = \vec{I} + \vec{j}$.

Since only the residue is detected, and not the neutrons, these single-particle

cross sections are a sum of the contributions from removal of the neutron due to elastic breakup (diffraction dissociation) and absorption (stripping) [Hus85], $\sigma_{sp} = \sigma_{sp}^{diff} + \sigma_{sp}^{str}$. These two contributions are computed separately, as integrals over the projectile's center of mass impact parameter, using [Tos99b]

$$\sigma_{sp}^{diff} = \frac{1}{2J+1} \int d\vec{b} \left[ \sum_M \langle \phi_{JM}^c | \, |(1 - \mathcal{S}_c \mathcal{S}_n)|^2 |\phi_{JM}^c\rangle - \sum_{M,M'} |\langle \phi_{JM'}^c | (1 - \mathcal{S}_c \mathcal{S}_n) |\phi_{JM}^c\rangle|^2 \right]$$

(3.2)

and

$$\sigma_{sp}^{str} = \frac{1}{2J+1} \int d\vec{b} \sum_M \langle \phi_{JM}^c | (1 - |\mathcal{S}_n|^2) |\mathcal{S}_c|^2 |\phi_{JM}^c\rangle.$$

(3.3)

Here the quantities $\mathcal{S}_c$ and $\mathcal{S}_n$ are the elastic S-matrices, or profile functions [AlK96, Tos97], for the core-target and removed neutron-target systems, expressed as functions of their individual impact parameters. These are calculated using the optical limit of Glauber theory [Gla59]. The neutron-core relative motion wave functions $|\phi_{JM}^c\rangle$ are calculated in a Woods-Saxon potential with radius and diffuseness parameters 1.25 and 0.7 fm. The depth of the potential was adjusted to reproduce the separation energy of the nucleon in the (initial) state with given $n\ell j$. In those cases where a more strongly bound nucleon is removed from a system which also binds a weakly bound and delocalized neutron, this few-body composite structure of the residue upon $\mathcal{S}_c$ was taken into account explicitly, as in [Tos99b]. An example of this is the case of $^{16}$C (section 5.1.3).

Equation (3.3) allows a simple interpretation. It is the integral over impact parameter, and average over $M$ substates, of the joint probability of the core being left intact by the reaction (given by the quantity $|\mathcal{S}_c|^2$) and of the neutron being absorbed (given by the quantity $(1 - |\mathcal{S}_n|^2)$). The diffractive cross section, Eq. (3.2), represents the probability that both the core and the neutron are not absorbed in the reaction. For halo states, Eqs. (3.2) and (3.3) make roughly equal contributions to the single-

particle cross section. For more strongly bound states the contribution from Eq. (3.2) is typically a factor of 2-3 smaller than that of Eq. (3.3) and may be smaller. It will be interesting to test this assumption experimentally.

The essential parameters in the calculation of the functions $\mathcal{S}$ are an effective nucleon-nucleon interaction and the rms matter radii of the assumed Gaussian matter distributions for the core and target nuclei. The $^9$Be matter radius was taken as 2.36 fm. The effective interaction, also assumed a Gaussian, used the free nucleon-nucleon cross sections [Cha90] and the real-to-imaginary ratio for the forward scattering amplitude tabulated by Ray [Ray79] for 100 MeV nucleons. The interaction range, of 0.5 fm, was chosen [Tos99b] so that the calculated reaction cross sections are consistent with measured values. Specifically, calculated reaction cross sections for the $^{12}$C–$^{12}$C and $^{27}$Al–$^{12}$C systems at 83 MeV/nucleon [Kox87], and for the proton–$^9$Be system at 60 MeV/nucleon [Ren72], were consistent with experiment.

The point-particle rms matter radii for the carbon isotopes were first reported in [Sai89, Lia90]; the results of the recent paper by Ozawa et al. [Oza98] are used here. Our results are not very sensitive to the matter radius; for $^{19}$C an overall increase of 10% reduces the calculated cross sections for removal of the halo or of more bound neutrons by 8% and 16%, respectively. The calculated single-particle cross sections, defined as the sum of the stripping and diffraction dissociation contributions, are given in Tables 4.2, 5.1, 5.2, 5.3, and 5.4. The use of alternative microscopic descriptions of the neutron-target interaction, and corresponding $\mathcal{S}_n$, has been shown to calculate very similar $\sigma_{sp}$ [Tos99c].

Theoretical calculations of the longitudinal momentum distributions of the core fragments were made in a simpler model, based on a black-disc approximation. In this, $\mathcal{S}_c$ and $\mathcal{S}_n$ are assumed to be unity outside of a cutoff impact parameter and zero

inside [Han96]. These impact parameter cutoffs were chosen to reproduce core-target reaction cross section systematics [Kox87] and the neutron-target reaction cross section of 306 mb at 60 MeV/nucleon. (The corresponding values are 286 and 298 mb when calculated for 62 and 57 MeV, respectively, with the parameters used for the partial cross sections. The widths of the momentum distributions are insensitive to the precise choice of target radius.) The neutron relative motion wave functions were calculated in a Woods-Saxon potential, as above. In this model the profile functions affect the limits of impact parameter integrations, and the momentum distribution takes the form of a one-dimensional Wigner transform of the wave packet produced in the reaction [Han96]. The integrated cross sections obtained with this procedure agree well with those calculated using the more realistic profile functions. Test calculations show that the shapes of the momentum distributions are much less sensitive to the choice of the impact-parameter cutoff than are the absolute values of the cross sections. In the following, these calculated shapes are presented scaled to fit the observed intensity, the idea being that the shape, taken separately, is the quantity that carries information on the $\ell$–assignment. The absolute value of the partial cross section then leads to the spectroscopic factor.

An alternative treatment, by Bonaccorso and Brink, has also been applied to the longitudinal momentum distributions of neutrons from the breakup of halo states [Bon98a, Bon98b, Bon99]. They use a semi-classical (constant velocity, straight line) approximation for the relative motion of the core and target, with a lower impact parameter cutoff, but a (non-sudden) quantum-mechanical treatment of the interaction of the neutron with the target. The treatment, which deals with the diffractive and the stripping parts in a consistent way, gives an excellent description of the angular distribution of neutrons following the breakup of $^{11}$Be [Bon98a]. The breakup contribution to the heavy residue longitudinal momentum distributions discussed in

the present work can be inferred from that of the neutron in the rest frame of the projectile. For ($^{11}$Be, $^{10}$Be$_{gs}$) breakup it was found [Aum00] that the resulting shapes are essentially indistinguishable from those of the eikonal calculation. A recent application to the carbon isotopes [Bon99] reported cross sections somewhat larger than those given in Table 5.4, however, depending on the chosen set of optical parameters for the n+$^9$Be system, the agreement is better. Bonaccorso finds [Bon00] for the case of $^{19}$C at 60 MeV/nucleon and an assumed neutron separation energy of 0.5 MeV single-particle cross sections, given as (stripping, diffraction in mb), of (100, 76) in agreement with our (99, 71) for the ground state. For an assumed $\ell = 2$ cross section to a 1.62 MeV excited level, she finds (21, 11) as compared with our values of (25, 11). Reference [Bon99] reports an interesting feature arising from the inclusion of the spin-dependence of the neutron interaction in the analysis. It turns out that different momentum signatures arise from the breakup of the $0d_{5/2}$ and $0d_{3/2}$ spin-orbit partners. The present data are not good enough to reveal this effect, but this prediction should certainly be kept in mind and investigated in future experiments.

# Chapter 4

# The test case: $^{15}$C

## 4.1 Previous theoretical and experimental work

The structure of $^{15}$C is well known from (d,p) transfer reaction studies on $^{14}$C [Gos73].

Spins and parities of $\frac{1}{2}^+$ and $\frac{5}{2}^+$ were assigned to the ground state and to the first excited state at 0.74 MeV, respectively. There are no other states below the neutron separation energy $S_n = 1.218$ MeV. The simplest levels that can exist in $^{15}$C are one-particle two-hole states and have positive parity. These correspond to an $s - d$ shell neutron coupled to a $^{14}$C core in the ground state. The low neutron separation energy and the ground state $J^\pi = \frac{1}{2}^+$ suggest the possibility of a halo structure, where the valence neutron is loosely bound to the semi-magic nucleus $^{14}$C.

The momentum distribution from nuclear breakup of $^{15}$C was studied in an earlier experiment [Baz98] and evidence of important contributions from excited states in $^{14}$C was found. Interaction and charge changing cross sections ($\sigma_I$, $\sigma_{cc}$) have been recently measured [Chu00] for several carbon isotopes ($^{12-20}$C). Interaction cross sections include all possible reactions, excluding elastic and inelastic scattering, while charge-changing cross sections represent only the channels corresponding to a change in the atomic number of the projectile. The difference between the two cross sections is then equal to the neutron-removal cross section $\sigma_{-xn}$, and has been found to be

similar for the neighboring nuclei $^{15}$C and $^{14}$C. This has been taken as evidence for the absence of a halo structure in $^{15}$C. However, the neutron-removal cross section includes contributions from the removal of any number of neutrons, thus preventing a discussion of any specific channel. More interesting is the comparison between the one-neutron removal channel for $^{14}$C and $^{15}$C. As a matter of fact, an enhanced one-neutron removal cross section for $^{15}$C has been observed [Sau00] and found to be in close agreement with theoretical estimates based on the same model used in this work.

## 4.2   Present shell-model results

According to shell-model calculations [Bro88], the wave function of the ground state of $^{15}$C is predominantly given by an $s$–wave neutron coupled to a ground state $^{14}$C core configuration $(1s_{1/2} \otimes 0^+)$, while the components with $^{14}$C in its excited states are small. For $^{15}$C, WBP and WBT give similar spectroscopic factors, for all possible configurations (cf. Table 4.1). However, the calculated level scheme of $^{15}$C is different in the two cases, although within the expected nominal deviation of 350 keV: with WBP the $\frac{5}{2}^+$ excited state is at 0.38 MeV, with WBT it is at 0.66 MeV, closer to the experimental value of 0.74 MeV [Ajz91]. For $^{14}$C both WBP and WBT interactions reproduce well the experimental level scheme [Ajz91], as illustrated in Table 4.1.

The set of basis states used to calculate the spectroscopic factors indicated with WBP and with WBT in Table 4.1 includes only $0\hbar\omega$ and $1\hbar\omega$ configurations, i.e., the two lowest energy configurations of the harmonic-oscillator configuration space. The extension of the configuration space, by including higher energy configurations $2\hbar\omega$ in the WBP calculation (denoted by WBP$^+$ in Table 4.1 and in the following), gives slightly smaller spectroscopic factors for the first three largest components $(1s_{1/2}\otimes0^+,$

Table 4.1: Experimental and calculated energy levels of $^{14}$C and associated spectroscopic factors for the different components of the $^{15}$C ground state wave function, calculated with WBP, WBT and WBP$^+$. There is no combination of the $^{14}$C $3^-$ state with a $p - sd$ shell neutron that can couple to the $^{15}$C ground state spin $\frac{1}{2}^+$. The theoretical energies are calculated with WBP, except for the excited $0^+$ state and the last $2^+$ state, which appear around 13 and 15 MeV, with WBP and WBT, respectively. For the other levels the three different calculations give similar energies. The experimental energies are taken from [Ajz91].

| $E_{exp}[MeV]$ | $E_{th}[MeV]$ | $I^\pi[\hbar]$ | $\ell[\hbar]$ | $C^2S_{WBP}$ | $C^2S_{WBT}$ | $C^2S_{WBP+}$ |
|---|---|---|---|---|---|---|
| 0.0 | 0.0 | $0^+$ | 0 | 0.98 | 0.98 | 0.95 |
| 6.09 | 5.48 | $1^-$ | 1 | 1.18 | 1.20 | 0.96 |
| 6.59 | 6.36 | $0^+$ | 0 | - | - | 0.02 |
| 6.73 | 6.45 | $3^-$ | - | - | - | - |
| 6.90 | 7.15 | $0^-$ | 1 | 0.46 | 0.46 | 0.39 |
| 7.01 | 7.77 | $2^+$ | 2 | 0.017 | 0.015 | 0.017 |
| 7.34 | 6.69 | $2^-$ | 1 | 0.001 | 0.001 | 0.001 |
| 8.32 | 8.32 | $2^+$ | 2 | - | - | 0.027 |

$0p_{1/2,3/2} \otimes 1^-$ and $0p_{1/2} \otimes 0^-$). For the $0d_{5/2} \otimes 2^+$ component the spectroscopic factor does not vary. In addition, another $2^+$ state in $^{14}$C comes down in energy at 8.32 MeV (with WBP and WBT it is at around 13 and 15 MeV, respectively), with a significant spectroscopic factor. Even though it corresponds to an unbound level in $^{14}$C, its energy of 8.32 MeV is very close to the neutron separation energy of 8.18 [Ajz91], therefore it has been included in the analysis. These two last components have been treated together, and their spectroscopic factors have been added, in the calculation of the cross sections and the comparison with the experimental results. The three different shell-model outputs are listed in Table 4.1.

For a consistent analysis with the other carbon isotopes (see also section 3.1), the WBP values will be used in the following. The results obtained by using the WBP$^+$ spectroscopic factors will also be discussed and are given in Table 4.2.

## 4.3 Experimental results

Two excited states in $^{14}$C are expected to be the most populated in the reaction (inset in Fig. 4.1): the $1^-$ state at 6.09 MeV, which decays directly to the ground state, and the $0^-$ state at 6.9 MeV, decaying to the ground state through the $1^-$, in a cascade of two $\gamma$ rays of 0.81 and 6.09 MeV.

The $\gamma$-ray spectrum observed from the decay of the excited $^{14}$C fragments (Fig. 4.1) was fitted using the simulated line shapes of the 0.81 and 6.09 MeV $\gamma$ rays. The additional continuum distribution measured from the $^{12}$Be and $^{16}$C data, as discussed in section 2.4.2 and shown in Fig. 2.7, was included in the fit. With these three components, while reproducing accurately the experimental data up to $E_\gamma \sim 6.4$ MeV, the fit somewhat underestimated the yield of $\gamma$ rays at higher energies. Although its associated spectroscopic factor is predicted to be very small, an additional response curve for a $\gamma$ ray around 7 MeV was included in the fit, to account for the $2^+$ level. The possibility of another $\gamma$ ray at 0.5 MeV from the decay of the $0^+$ state at 6.59 MeV to the $1^-$ was also examined and estimated to be negligible. However, the presence of 0.511 MeV annihilation photons from the higher energy $\gamma$ rays made it difficult to analyze the low energy part of the spectrum with good accuracy.

As discussed in section A.1.2, the measured total cross section is 137$\pm$16 mb, to be compared to the theoretical prediction of 197.5 mb. Using the coincident $\gamma$-ray information, the partial cross sections to the three excited states and to the ground state were extracted and are given in Table 4.2.

In agreement with theory, the largest component of the cross section corresponds to the removal from $^{15}$C of the $1s_{1/2}$ neutron coupled to a $^{14}$C$_{g.s.}$ core.

The results from WBP and WBP$^+$ are not sensibly different, and although they are consistent with the data within two standard deviations, a comparison between
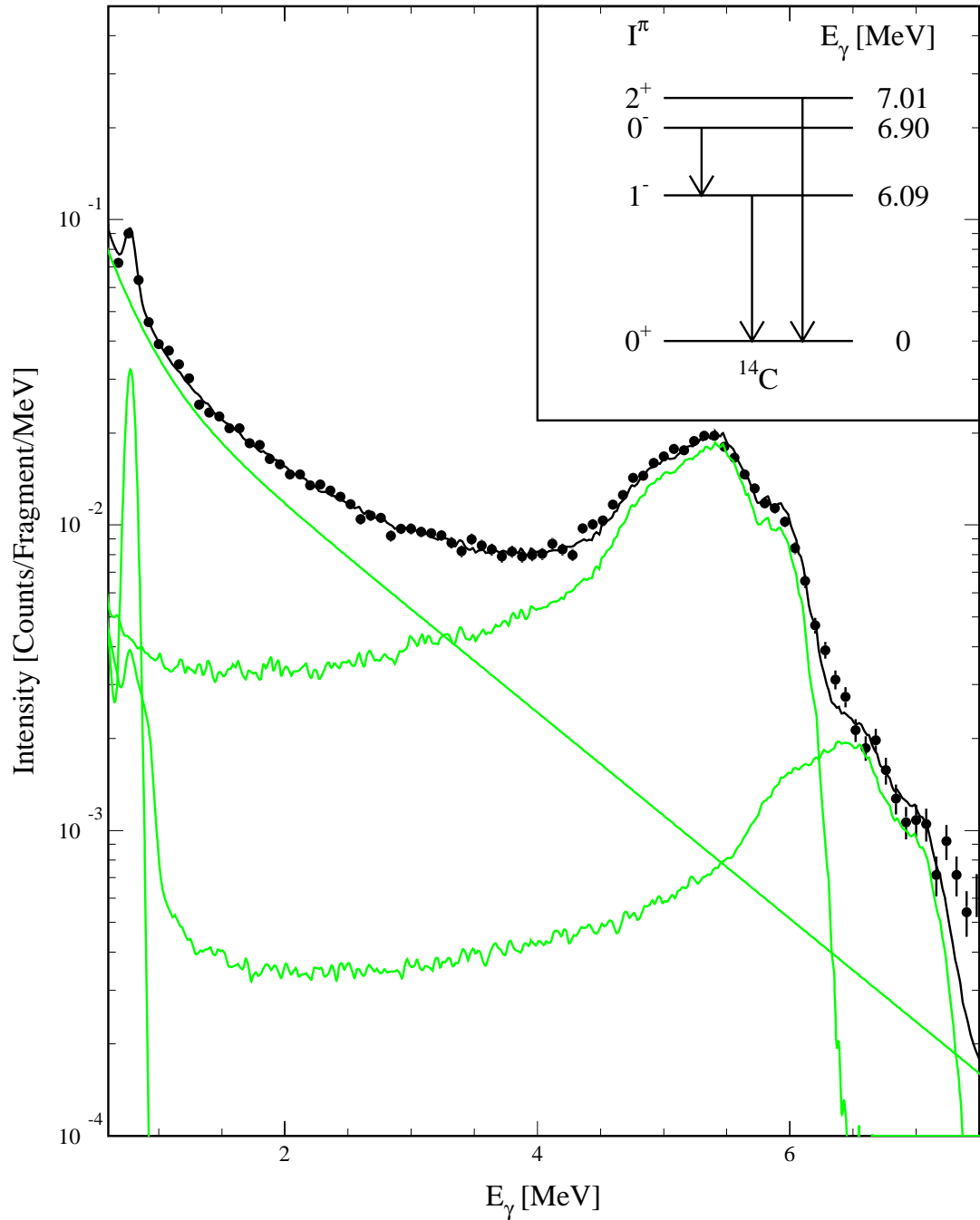
Figure 4.1: Doppler corrected $\gamma$-ray spectrum from $^9$Be($^{15}$C,$^{14}$C)X. The curves are the simulated response functions for the observed $\gamma$ rays and the exponential measured continuum distribution extracted from the $^{12}$Be and $^{16}$C data (Fig. 2.7). Inset: Simplified level scheme of $^{14}$C.

Table 4.2: Comparison between the experimental cross sections and the theoretical predictions with spectroscopic factors calculated with different interactions (WBP and WBP$^+$, denoted with the subscript +) for the reaction $^9$Be($^{15}$C,$^{14}$C)X at $E = 54$ MeV/nucleon. The level energies are taken from previous work [Ajz91].

| $E$ [MeV] | $I^\pi$ [$\hbar$] | $\ell$ [$\hbar$] | $\sigma_{sp}$ [mb] | $C^2S$ | $C^2S_+$ | $\sigma_{th}$ [mb] | $\sigma_{th,+}$ [mb] | $\sigma_{exp}$ [mb] | $b_{th}$ [%] | $b_{th,+}$ [%] | $b_{exp}$ [%] |
|---|---|---|---|---|---|---|---|---|---|---|---|
| 0.0 | $0^+$ | 0 | 144 | 0.98 | 0.95 | 141.5 | 137.1 | 109±13 | 71.7 | 74.5 | 80±2 |
| 6.09 | $1^-$ | 1 | 34 | 1.18 | 0.96 | 40.5 | 33.0 | 22±3 | 20.5 | 17.9 | 16±2 |
| 6.90 | $0^-$ | 1 | 32 | 0.46 | 0.39 | 14.9 | 12.6 | 3±1 | 7.5 | 6.8 | 2±1 |
| 7.01 | $2^+$ | 2 | 34 | 0.02 | 0.017 | 0.6 | 1.5 | 3±1 | 0.3 | 0.8 | 2±1 |
| 8.32 | $2^+$ | 2 | 34 | - | 0.027 | - | 1.5 | - | | | |
| sum | | | | | | 197.5 | 184.2 | 137±16 | | | |

the predicted and measured cross sections and branching ratios indicates a qualitative agreement. The comparison also favors the WBP$^+$ spectroscopic factors. Why the structure of $^{15}$C seems to present a different behavior than the heavier carbon isotopes remains to be understood. One explanation for the observed smaller cross sections may be the manifestation of the quenching of the spectroscopic factors in nuclei closer to the valley of stability. Dieperink and de Witt Huberts [Die90] find that the general occupancy of single-particle proton orbitals below the Fermi surface, as determined from the charge densities, is only $75 \pm 10\%$ rather than unity and that for (e,e$'$p) single-proton removal reactions, the reduction can be even more drastic. For the nucleus most relevant to those discussed in the present work, $^{12}$C, the spectroscopic factors to the $\frac{3}{2}^-$ and $\frac{1}{2}^-$ states of $^{11}$B are only 65% and 50%, respectively, of the values predicted by a shell-model calculation similar to the one used here. It may be possible that $^{15}$C lies in a transition region where this phenomenon is still present.

With the $\gamma$-ray information, the measured momentum distribution of the $^{14}$C residues was decomposed into the two components corresponding to the $^{14}$C fragments

in the ground state and in the excited states $1^-, 0^-$, shown in Fig. 4.2.

In particular, the momentum distribution of the residues in the $1^-, 0^-$ states was obtained by requiring a coincidence with $\gamma$ rays in the energy range between 4.4 and 6.4 MeV, where the dominating contribution to the $\gamma$ spectrum is given by the 6.09 MeV response curve. The 6.09 MeV level is fed by the 6.90 MeV level, therefore the obtained distribution includes the contribution from the $0^-$ state as well. The resulting distribution was corrected for the additional contribution from the continuum. This was extracted from events in coincidence with $\gamma$ rays of energies between 1 and 2.5 MeV, where the continuum is the major component of the spectrum. The momentum distribution of the ground state residues was obtained by subtracting the excited states momentum distribution from the inclusive. Therefore, it includes also the contribution from the $2^+$ state. However, its intensity is very small and within the uncertainty on the ground state intensity, thus it was neglected. A clean discrimination between the momentum distributions of the individual excited states in $^{14}$C was not possible due to the presence of a $\gamma$ ray at 0.98 MeV, interpreted as arising from the deexcitation of the $1^+$ state in $^{8}$Li produced in the target. This is demonstrated in Fig. 4.3, where the laboratory and c.m. spectra are plotted together, showing how the 0.98 MeV peak is smeared out after Doppler correction, extending under the 0.81 MeV peak. A peak at that energy was observed also in the laboratory system spectra from the $^{12}$Be and $^{16}$C data, as shown in Fig. 4.4.

A comparison with the calculated curves for $\ell = 0, 1$ clearly indicates the $s$–wave character of the ground state distribution and the $p$–wave character of the excited states of $^{14}$C, as expected (Fig. 4.2). This result reaffirms the spectroscopic power of one-neutron knockout reactions.

However, while the momentum distribution of the excited states is in good agree-
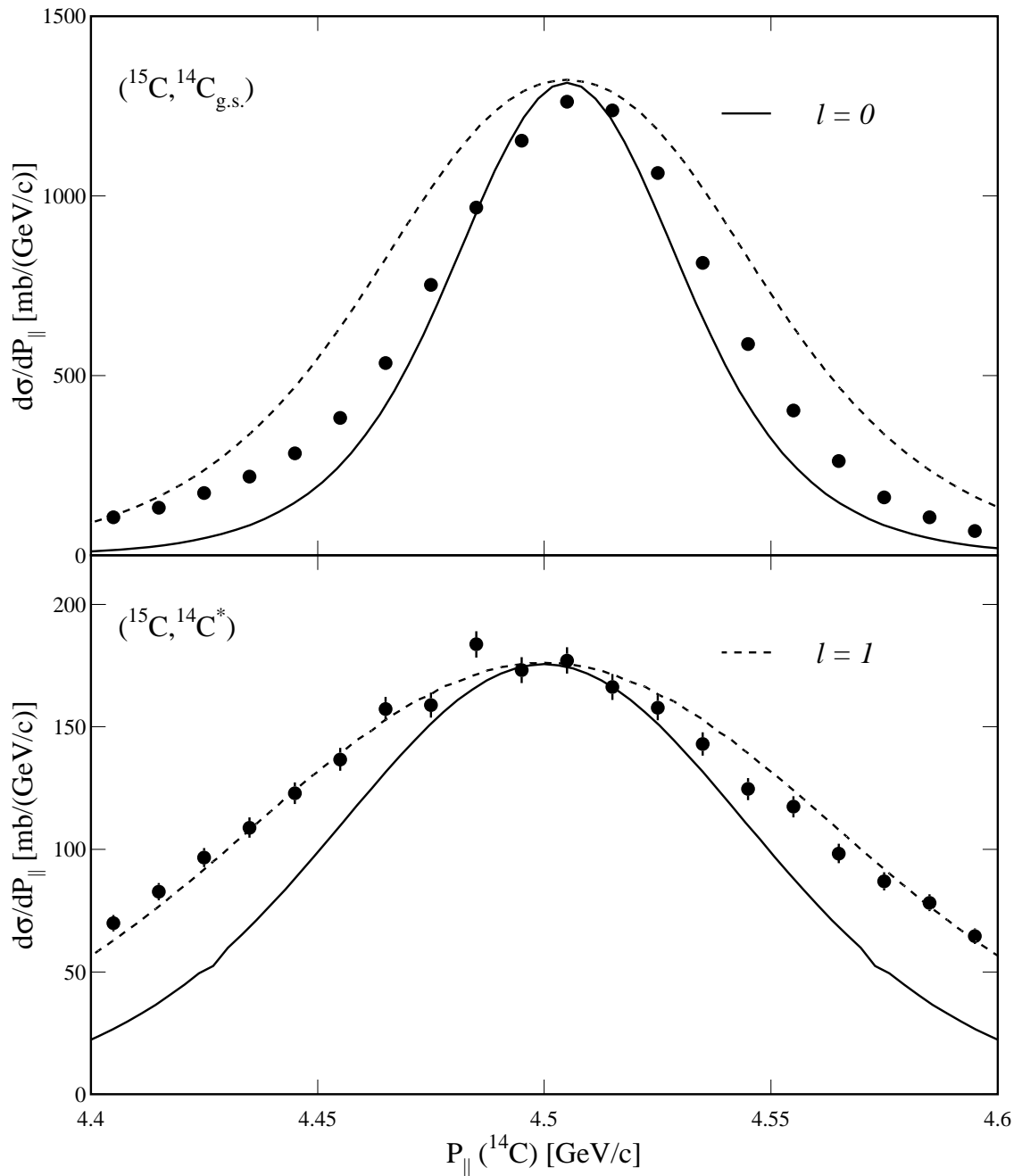
Figure 4.2: Longitudinal momentum distributions of $^{14}C_{g.s.}$ (top), and of $^{14}C_{1-,0-}$ (bottom), after one-neutron removal from $^{15}C$. The curves are calculated eikonal momentum distributions for $\ell = 0, 1$.

49
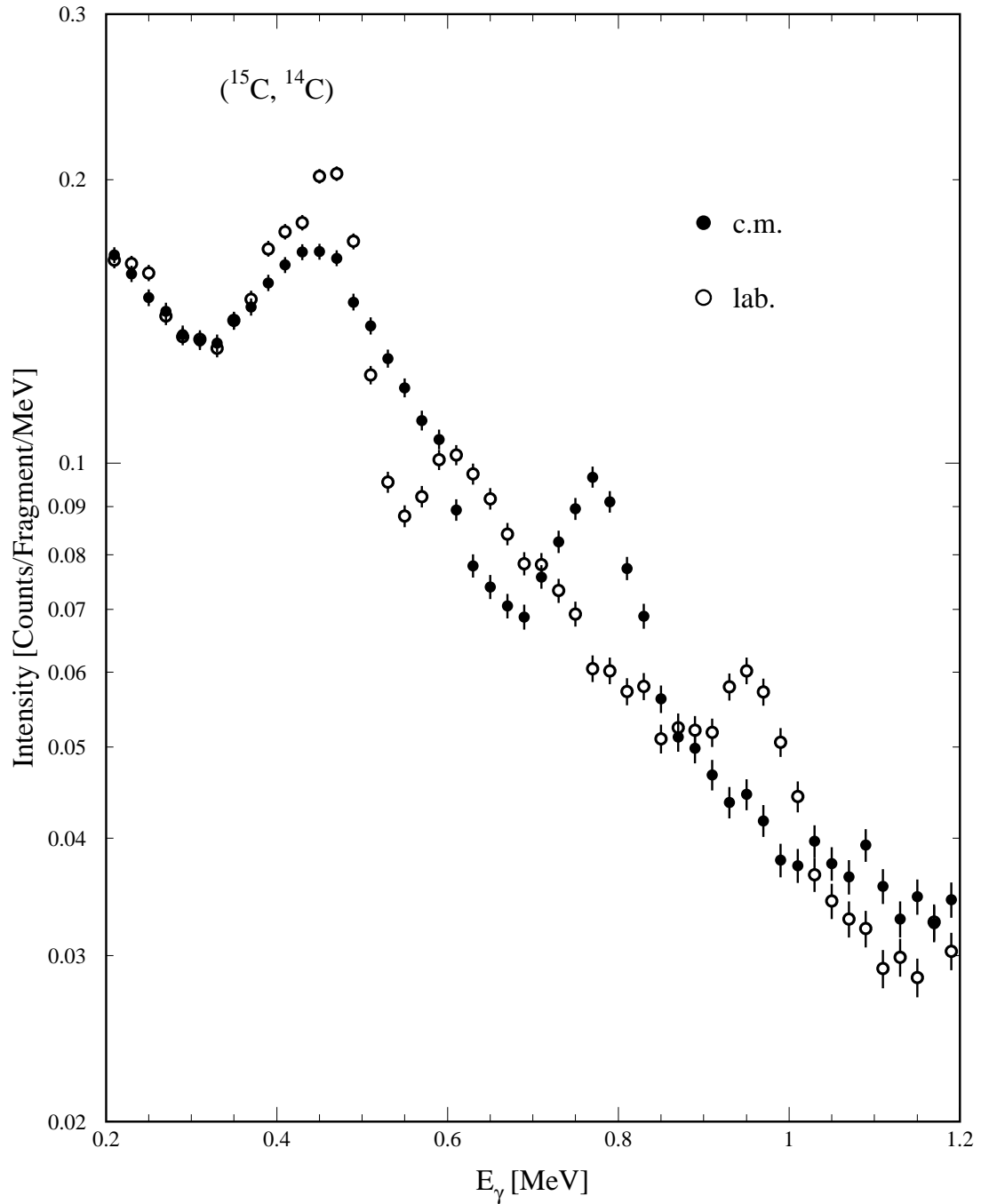
Figure 4.3: Laboratory and c.m. system $\gamma$-ray spectra measured in coincidence with $^{14}$C residues produced in one-neutron removal reactions on $^{15}$C. The 0.98 MeV peak in the laboratory spectrum corresponds to a $\gamma$ ray emitted by $^8$Li, produced in reactions in the target, and is smeard out by the Doppler correction in the c.m. spectrum.
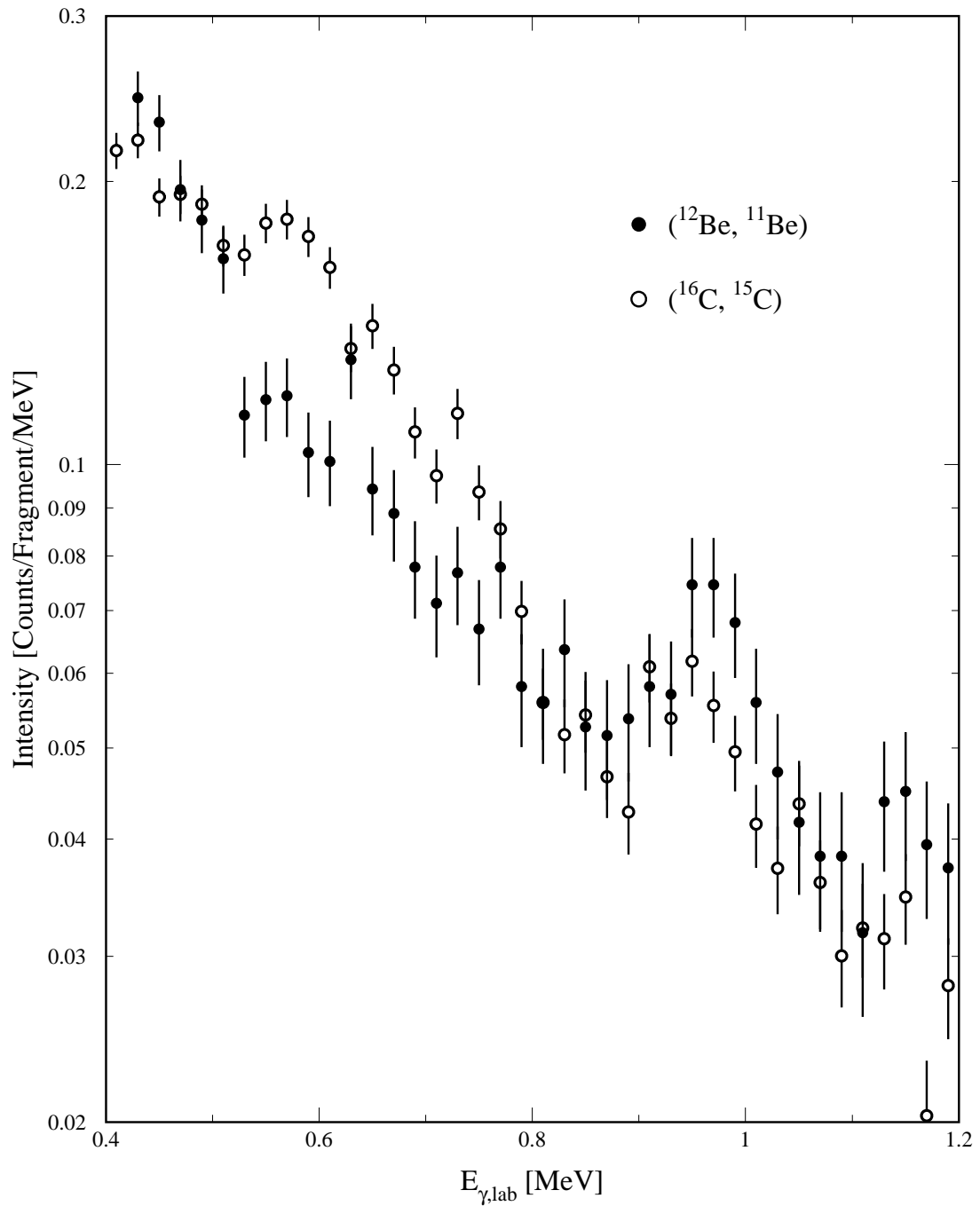
Figure 4.4: Laboratory $\gamma$-ray spectra from one-neutron removal reactions on $^{12}$Be and $^{16}$C. The 0.98 MeV peak coresponds to a $\gamma$ ray emitted by $^{8}$Li, produced in reactions in the target.

51

ment with the $\ell = 1$ calculated curve, small deviations in the shape of the ground state momentum distribution, especially at low energies, are apparent. These could be related to the use of the sudden approximation (which does not require energy conservation), on which the eikonal model calculations rely. Recently, fully quantum mechanical calculations have been developed to investigate this possibility with a coupled discretized continuum channels approach (CDCC) [Tos00]. In fact, with this approach the calculated diffraction momentum distributions appear asymmetric and can explain the observed deviations. This effect has been observed also in the one-neutron removal data from $^{11}$Be, and has been investigated [Tos00].

An interesting feature of the CDCC momentum ditributions is that their asymmetry becomes more pronounced progressing from small to large scattering angles. This effect is present in the data as well, as shown in Figs. 4.6 and 4.7. Four momentum distributions for the $^{14}$C residues in their ground state were obtained by grouping the data according to scattering angle, from $0°$ to $4°$, on $1°$ intervals. The size of the intervals was limited by the experimental angular resolution, which was estimated to be $1°$, as discussed in detail in the second part of section A.1.2. Their asymmetry increases with the the scattering angle as predicted by CDCC. However, the measured momentum distributions include both diffraction and stripping contributions, which cannot be separated, as the experiment was not designed to detect the outcoming neutrons.

Two assumptions on the stripping distribution can be made:

(i): it has the same shape as the diffractive;

(ii): it has the shape calculated in the eikonal model.

The calculated ground state cross section has been compared to the measured value in both $^{15}$C and $^{11}$Be. For this purpose the measured cross section has been

divided into stripping and diffraction components, in the ratio of the predictions of the eikonal calculation. The obtained diffraction cross section is in good agreement with the results from the CDCC calculations. Fig. 4.5 shows the experimental and CDCC diffraction cross sections in each angle bin.

The comparison between the measured and calculated distributions using assumption (i) and assumption (ii) is illustrated in Fig. 4.6 for $^{15}$C and in Fig. 4.7 for $^{11}$Be. When assumption (i) is taken, the curves superimposed to the data represent the CDCC calculations, scaled to the measured cross sections. For assumption (ii) the stripping (eikonal) and diffraction (CDCC) curves were added in the proportions obtained from Fig. 4.5.

The comparison with the data suggests that the stripping distribution has a similar shape to the one corresponding to diffraction. In fact, with assumption (i) a good description of the data is obtained at all scattering angles. Moreover, the shape of the measured inclusive ground state momentum distribution is similar to the one calculated for the diffractive part of the cross section in both $^{15}$C and $^{11}$Be. (Figs. 4.8 and 4.9). (The instrumental resolution in momentum is not included in the theoretical curves. However, its value measured for the incident $^{15}$C beam was of 6 MeV/c FWHM and the consequent broadening of the folded distributions would be less than 1%.)

With assumption (ii), the contribution from the eikonal stripping momentum distribution introduces sizable deviations from the observed behavior, especially at scattering angles between 1° and 3°.

Besides improving the interpretation of the reaction mechanism, these calculations prove the accuracy of the experimental ground state momentum distributions, obtained by subtracting the events in coincidence with $\gamma$ rays from the inclusive
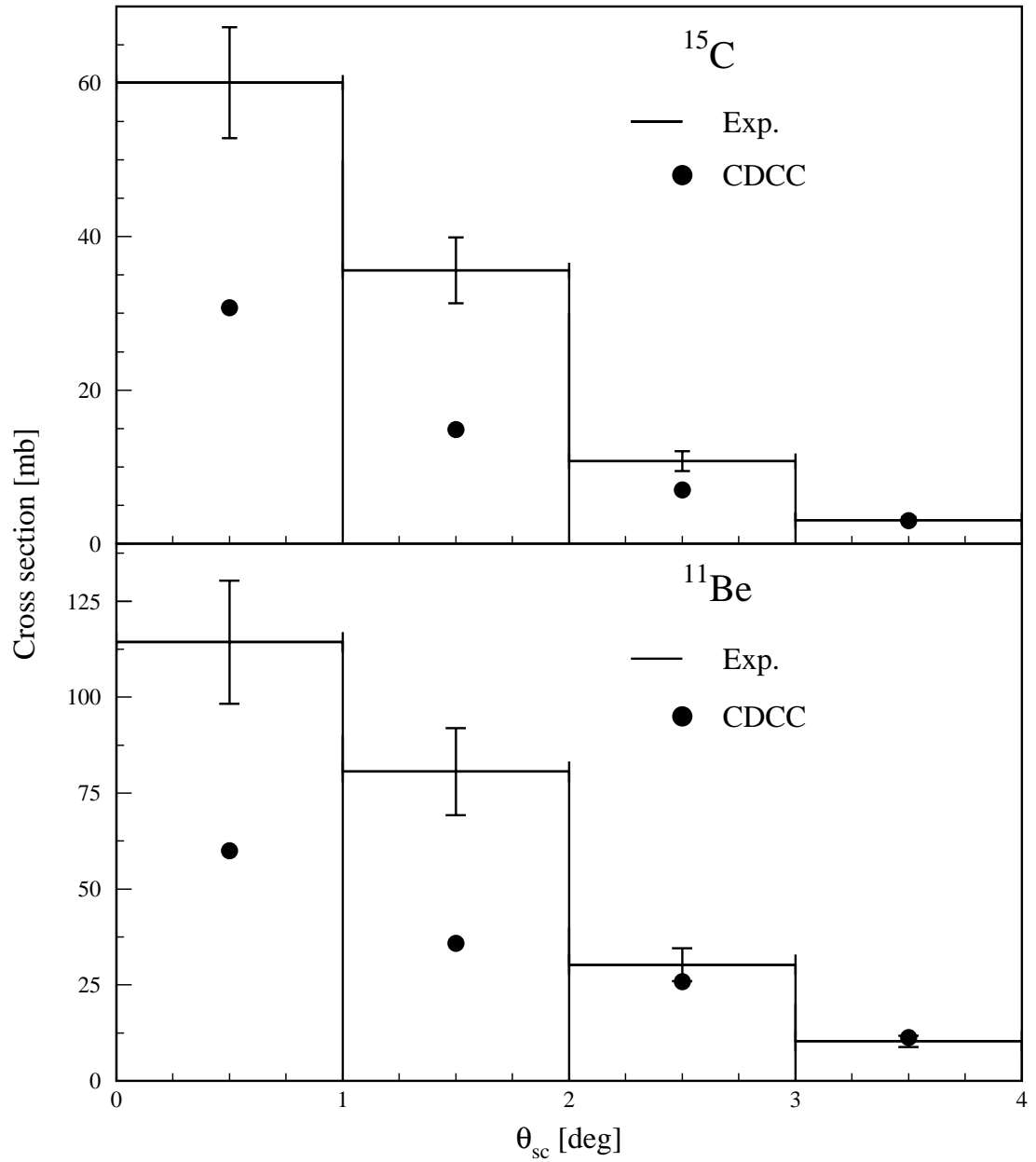
Figure 4.5: Experimental cross sections and calculated diffraction cross sections with CDCC, for $^{15}$C (top) and $^{11}$Be (bottom).
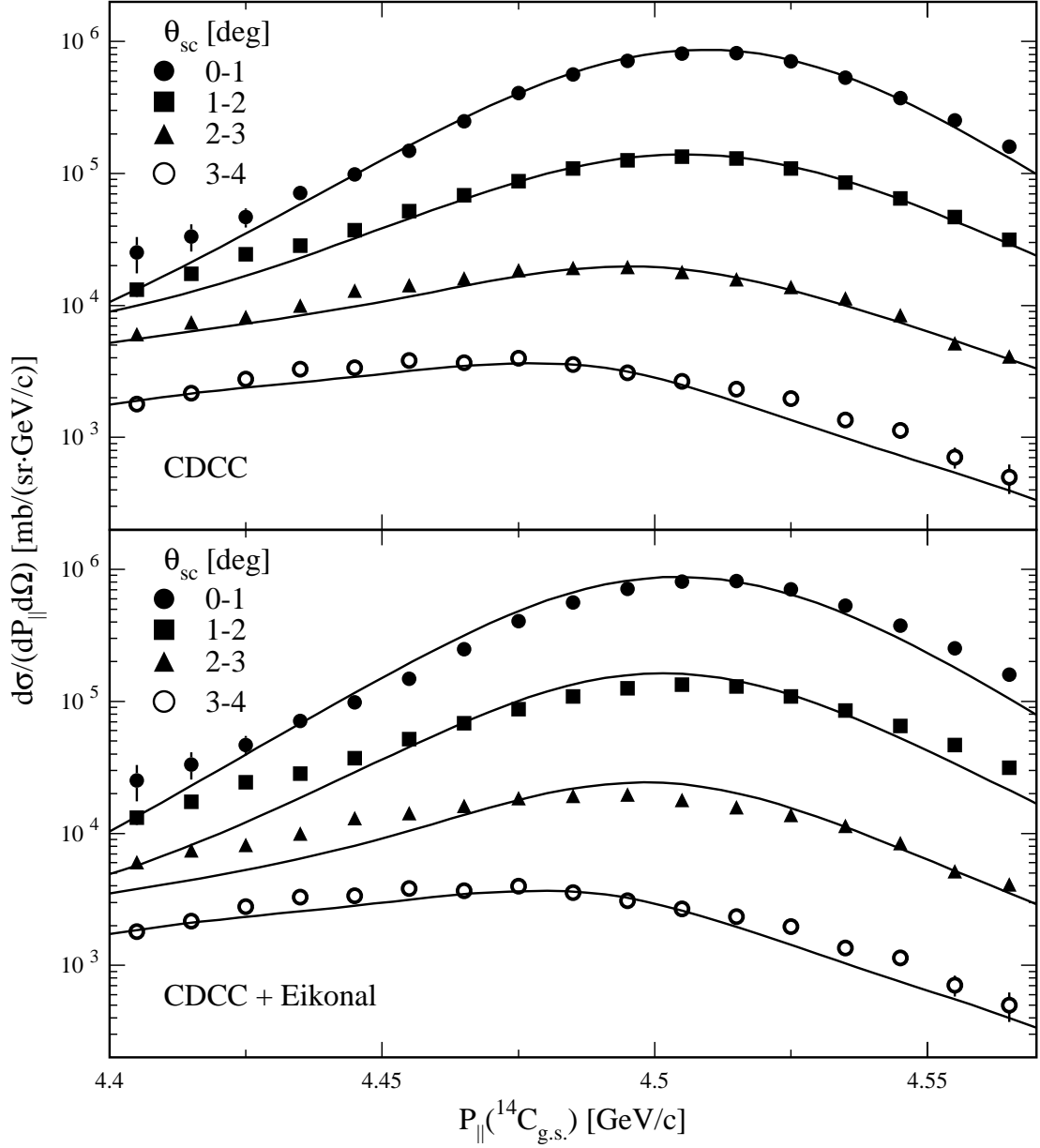
Figure 4.6: Longitudinal momentum distributions of the $^{14}C_{g.s.}$, at different scattering angles. Top: The curves are calculated with CDCC, and scaled to reproduce the measured cross sections. Bottom: The curves are the sum of the calculated CDCC distributions for the diffractive part and the eikonal distributions for the stripping part.
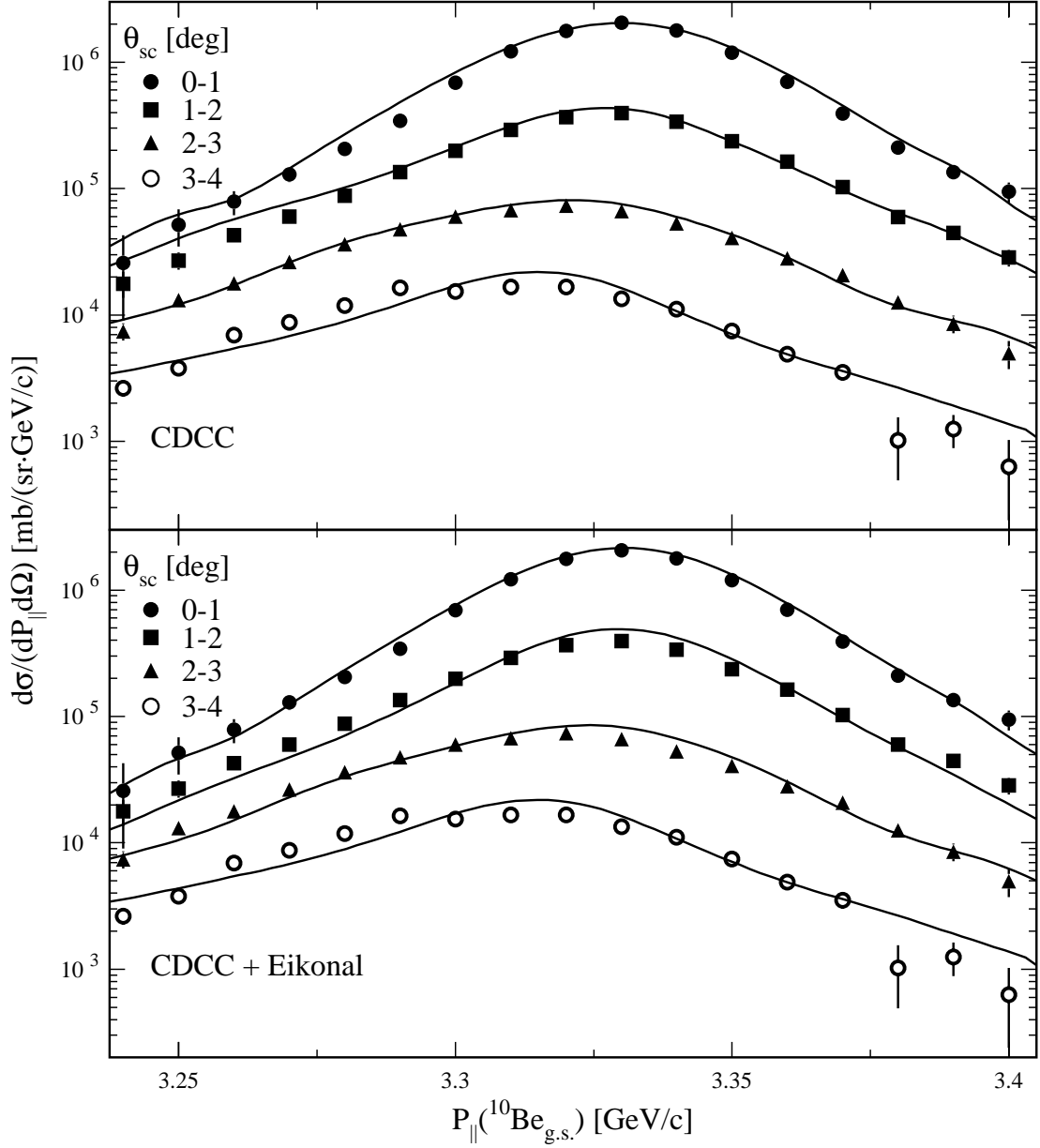
Figure 4.7: Longitudinal momentum distributions of the $^{10}$Be$_{g.s.}$, at different scattering angles. Top: The curves are calculated with CDCC, and scaled to reproduce the measured cross sections. Bottom: The curves are the sum of the calculated CDCC distributions for the diffractive part and the eikonal distributions for the stripping part.
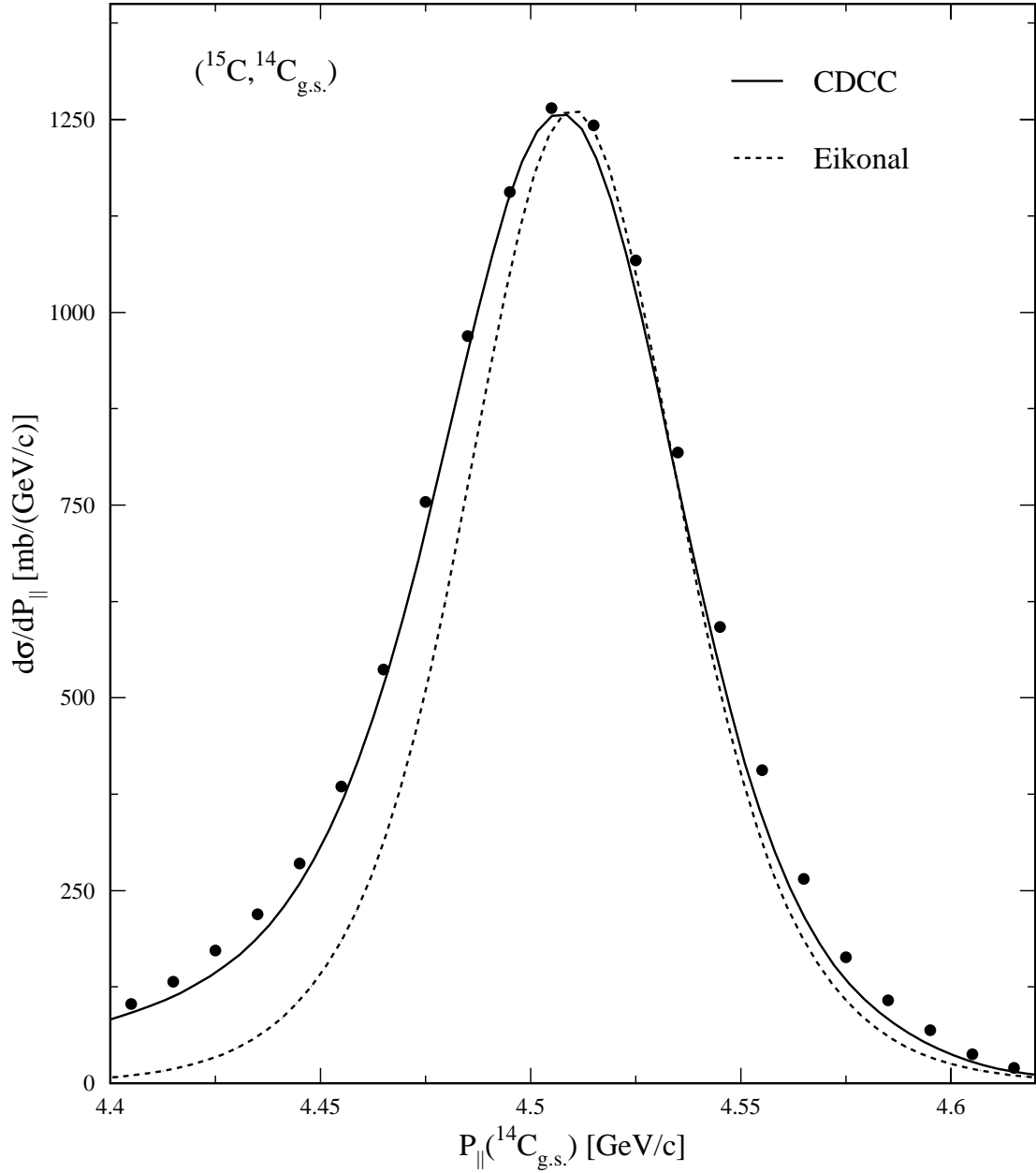
Figure 4.8: Longitudinal momentum distribution of the $^{14}C_{g.s.}$ residues from one-neutron removal reactions on $^{15}C$. The curves are CDCC (solid line) and eikonal (dashed line) calculations. The CDCC curve is scaled to reproduce the measured cross section, the eikonal curve is arbitrarily scaled.
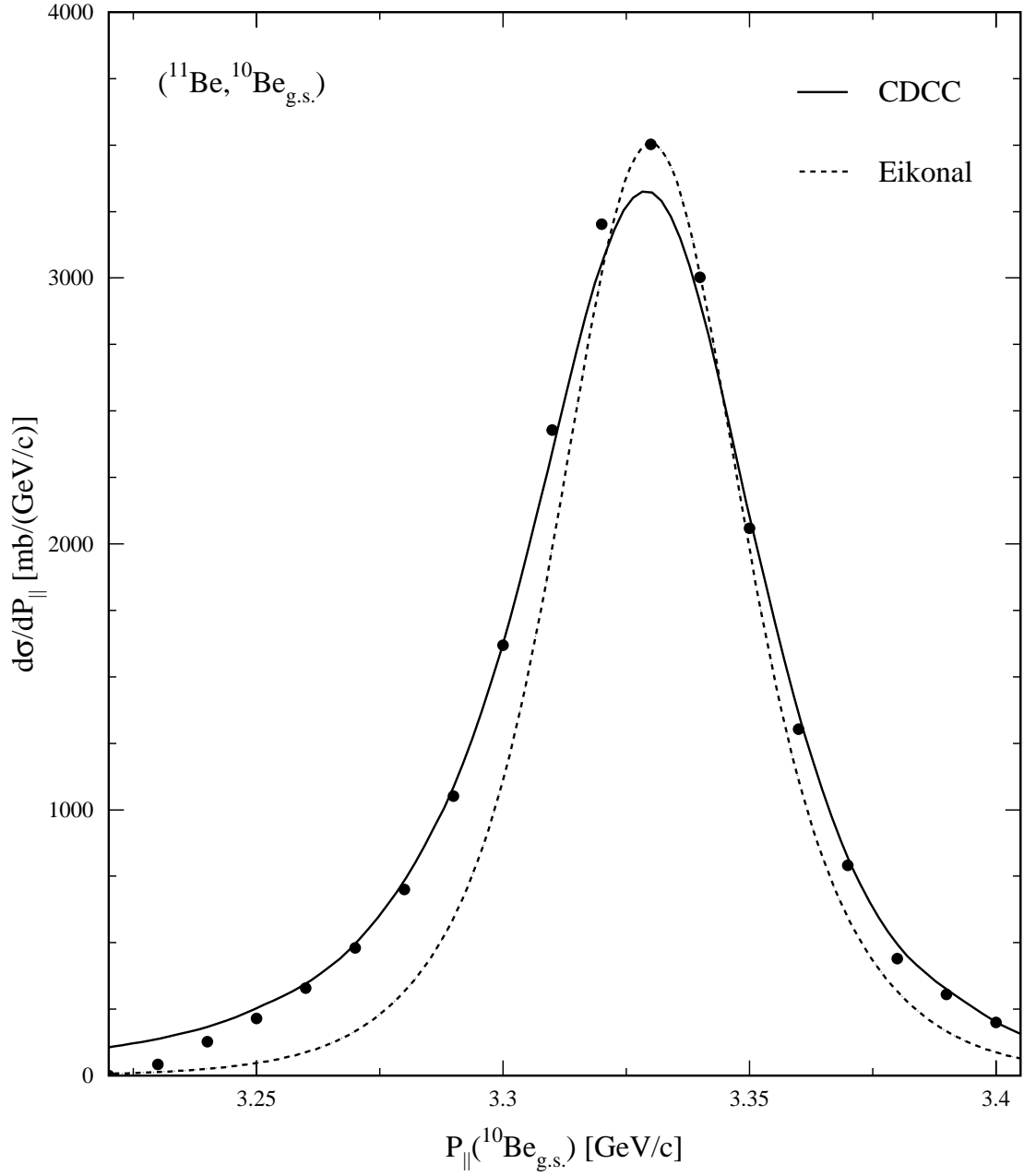
Figure 4.9: Longitudinal momentum distribution of the $^{10}\mathrm{Be}_{g.s.}$ residues from one-neutron removal reactions on $^{11}\mathrm{Be}$. The curves are CDCC (solid line) and eikonal (dashed line) calculations. The CDCC curve is scaled to reproduce the measured cross section, the eikonal curve is arbitrarily scaled.

distributions.

Finally, an interesting feature of the ground state momentum distributions for $^{15}$C and $^{11}$Be is that they are identical in shape, when appropriately transformed into the center of mass system, taking into account the relativistic $\gamma$ factor, provided that the $^{11}$Be distribution is broadened by the square root of the ratio of their separation energies $(\sqrt{S_n(^{15}\text{C})/S_n(^{11}\text{Be})} = \sqrt{1.218/0.504})$, as shown in Fig. 4.10. This is in fact the expected dependence with separation energy of the width of the momentum distribution for an $s$–wave neutron and a Yukawa wave function. The wave function has the form $\exp(-r/\rho)/r$, where the decay length $\rho = \hbar/\sqrt{2\mu S_n}$, and $\mu$ is the reduced mass. The Fourier transform of this wave function gives a Lorentzian distribution of width $\Gamma = 2\hbar/\rho = 2\sqrt{2\mu S_n}$. The result shows a consistency between the data, and the systematics of the asymmetry effect.
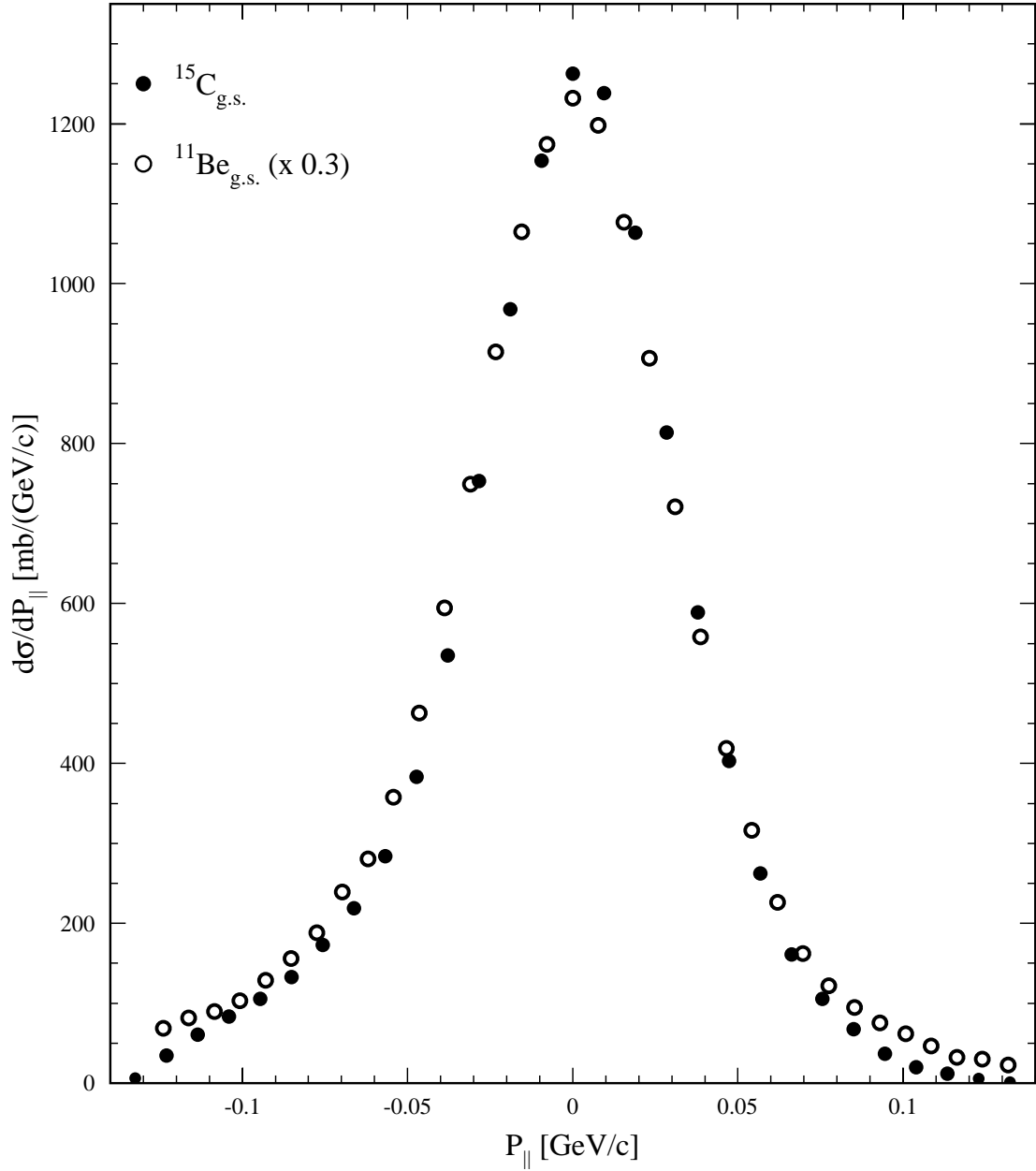
Figure 4.10: Projectile center of mass longitudinal momentum distributions of the $^{14}$C and $^{10}$Be residues in their ground state after one-neutron removal from $^{15}$C and $^{10}$Be. The $^{10}$Be distribution has been broadened by the square root of the ratio of the separation energies.

# Chapter 5

# The structure of the heavier carbon isotopes

## 5.1 Spectroscopy of $^{16}$C

### 5.1.1 Previous theoretical and experimental work

The structure of the low-lying levels in $^{16}$C has been investigated [For77, For78, Ser78, Bal77] in the reactions $^{14}$C(t,p)$^{16}$C and $^{14}$C(t,p$\gamma$)$^{16}$C. Tilley et al. [Til93] discuss properties and the level scheme, that will be referred to in more detail in section 5.2. The structure of $^{16}$C is expected to correspond to $^{14}$C $\otimes$ $^{18}$O. Since $^{14}$C is a near-magic nucleus, the simplest conjecture is that the neutron pair of $^{16}$C should be similar to that of $^{18}$O, which has a relatively pure $s^2+d^2$ two-particle configuration with spectroscopic factors [Law76] $C^2S(1s_{1/2}) = 0.38$ and $C^2S(0d_{5/2}) = 1.44$, and where the missing part is a 4p-2h collective contribution. The wave functions in Ref. [Law76] were later used in the study of the mirror nucleus $^{18}$Ne [She98] and successfully reproduced the observed Coulomb energy shifts. When the LSF model [Law76] is applied to $^{16}$C, the $s^2$ and $d^2$ components are about equal and the spectroscopic factors would be about $C^2S(1s_{1/2}) = 0.93$ and $C^2S(0d_{5/2}) = 1.07$ [For78]. As discussed in the next section, the origin of the difference between the $^{18}$O and $^{16}$C spectroscopic factors arises mainly from the change in single-particle energies.

The experimental situation for the next lighter $N = 10$ isotone $^{14}$Be is interesting but less clear experimentally. The breakup reaction to $^{12}$Be [Zah93] leads to a narrow momentum distribution indicating a halo structure, presumably arising from a substantial $s^2$ component. The same is suggested by the beta-delayed neutron decay of $^{14}$Be, which shows [Bel95, Ber99] an almost superallowed branch ($\log ft \approx 3.7$) to a $1^+$ state (not directly observed) at 1-2 MeV excitation energy. The theory of the $^{14}$Be beta decay has been discussed by Timofeyuk and Descouvemont [Tim96]. A recent $2n$ pairing model calculation [Lab99] suggests, somewhat surprisingly, a negative-parity ground state of $^{13}$Be and spectroscopic factors of 0.9, 0.6, and 0.5 for single-neutron breakup to the $\frac{1}{2}^-$ ground state, the $\frac{1}{2}^+$ and $\frac{5}{2}^+$ $s-$ and $d-$states, respectively.

## 5.1.2   Present shell-model results

For $^{18}$O, WBP and WBT are equivalent to the $sd-$shell USD results with $C^2S(1s_{1/2}) = 0.30$ and $C^2S(0d_{5/2}) = 1.58$ (with the remaining in $C^2S(0d_{3/2}) = 0.12$ leading to a state at high excitation energy). For $^{16}$C, WBP gives $C^2S(1s_{1/2}) = 0.60$ and $C^2S(0d_{5/2}) = 1.23$, and WBT gives $C^2S(1s_{1/2}) = 0.78$ and $C^2S(0d_{5/2}) = 1.07$. One reason for the difference can be related to the $^{15}$C spectrum with the $\frac{5}{2}^+$ excited state at 0.38 MeV with WBP and at 0.66 MeV with WBT, compared to the experimental energy at 0.74 MeV; and on this basis the WBT results are preferred. The spectroscopic factors depend upon the spacing of the single-particle energies and, in particular, the crossing of the single-particle energies between $^{17}$O (where the $\frac{1}{2}^+$ is 0.87 MeV above the $\frac{5}{2}^+$) and $^{15}$C, which gives rise to the large change between $^{18}$O and $^{16}$C.

### 5.1.3 Experimental results and discussion

The neutron knockout reaction on $^{16}$C (neutron separation energy $S_n = 4.25$ MeV [Aud93, Aud97]) leads to the two (only) bound levels of $^{15}$C, the $\frac{1}{2}^+$ ground state and the $\frac{5}{2}^+$ state at 0.740 MeV [Ajz91]. The latter has a long half-life ($2.60 \pm 0.07$ ns), which combined with the high velocity of the residues causes the $\gamma$ rays to be emitted at a mean distance of 34 cm from the center of the detectors, which are only 20 cm long. This means that the Doppler correction scheme described in section 2.4 fails. In fact, most $\gamma$ rays are emitted outside of the apparatus reducing the detected intensity. Fig. 5.1 shows the $\gamma$-ray spectrum measured in coincidence with $^{15}$C residues without the Doppler back-correction.

Fortunately, accurate estimates of the continuum distribution are available from the previous experiments on $^{11}$Be [Aum00] and $^{12}$Be [Nav00], cf. section 2.4.2. The $^{16}$C data in Fig. 5.1 show a clear excess above the $^{12}$Be background in the region 0.5-0.8 MeV. A simulated response curve of the NaI array to the isomeric decay was generated in a Monte Carlo procedure in which the $\gamma$ events were assumed to appear downstream along the beam axis with the appropriate exponential distribution. The response was then simulated by the GEANT code, as before. The resulting efficiency turned out to be reduced by a factor of 4 as compared to instantaneous emission. A combined fit to the components in Fig. 5.1 gave an absolute branch of $30 \pm 10\%$ to the excited $\frac{5}{2}^+$ state with the error determined by the statistics alone. However, this result is almost certainly an underestimate, corresponding to an overestimate of the detection efficiency. This is because the simulation did not include the size and divergence of the incoming beam and the angular spread of the outgoing residues, nor did it include the way that these affect the absorption of the low-energy $\gamma$ rays emitted in the backward direction. This analysis provides a semi-quantitative but
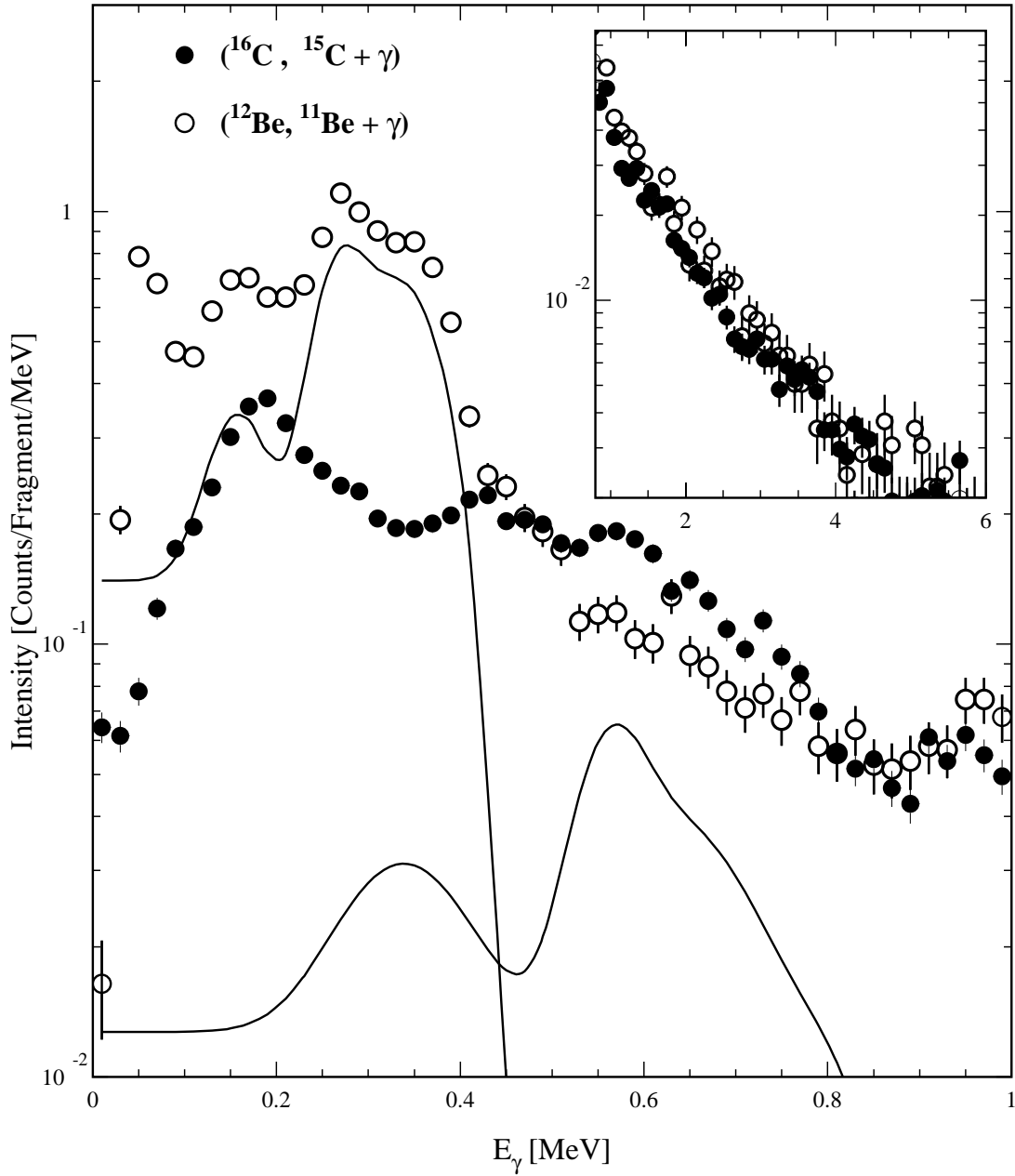
Figure 5.1: Laboratory system $\gamma$-ray spectra from ${}^{9}\text{Be}({}^{16}\text{C},\ {}^{15}\text{C}+\gamma)\text{X}$ (filled circles) and ${}^{9}\text{Be}({}^{12}\text{Be},\ {}^{11}\text{Be}+\gamma)\text{X}$ (open circles), normalized to the number of projectile fragments. The solid lines are simulated response functions for the 0.74 MeV $\gamma$ ray from the decay in flight of ${}^{15}\text{C}^*$ and for the 0.32 MeV $\gamma$ ray from ${}^{11}\text{Be}^*$. The inset shows experimental $\gamma$-ray spectra from ${}^{11}\text{Be}$ and ${}^{15}\text{C}$ for $\text{E}_\gamma > 1$ MeV. The "tails" above the $\gamma$ lines, the only discrete lines present, are the continuum distributions discussed in the text.

Table 5.1: Partial cross sections $\sigma$ and branching ratios $b$ for the final states $I^\pi$ in the residues produced in $^9$Be($^{16}$C,$^{15}$C)X at $E = 62$ MeV/nucleon. The theoretical cross sections $\sigma_{th}$ are calculated from Eq. (3.1) using the WBP spectroscopic factors $C^2S$ and the single-particle cross sections $\sigma_{sp}$. The values of $\sigma_{th}$ include overlap factors of 0.897 and 0.948, respectively (see section 3.2).

| ($^{16}$C,$^{15}$C) | $E$ [MeV] | $I^\pi$ [$\hbar$] | $\ell$ [$\hbar$] | $C^2S$ | $\sigma_{sp}$ [mb] | $\sigma_{th}$ [mb] | $\sigma_{exp}$ [mb] | $b_{th}$ [%] | $b_{exp}$ [%] |
|---|---|---|---|---|---|---|---|---|---|
| | 0.0 | $\frac{1}{2}^+$ | 0 | 0.60 | 64 | 34 | 32±6 | 44 | 42 ± 6 |
| | 0.74 | $\frac{5}{2}^+$ | 2 | 1.23 | 37 | 43 | 45±7 | 56 | 58 ± 6 |
| $\sigma_{tot}$ | | | | | | 77 | 77±9 | | |

direct indication of the contribution of the appearance of the $d^2$ component in the $^{16}$C ground state. The statistics in Fig. 5.1 are insufficient to permit an extraction of the momentum distribution to the excited level, but since the assignments in the $^{15}$C nucleus are well established, this is probably of little importance.

A more accurate estimate of the branching ratio was obtained from the measured inclusive longitudinal momentum distribution of the residues shown in Fig. 5.2. Experience from previous experiments has shown that the shapes of the theoretically calculated momentum distributions are well reproduced by experiment. As these, furthermore, are very different for $s-$ and $d-$state knockout, it is easy to arrive at the overall fit (envelope) shown in the figure. The criterion adopted to fix the limits of the fit was to consider the momentum acceptance range of $\pm 2.5\%$. The geometrical loss for the inclusive spectrum was estimated to be 2% by the method described in section A.1. The extrapolation of the envelope gave momentum acceptance losses of 4%. Both corrections were applied to the measurement to give the total (inclusive) cross section of $77 \pm 9$ mb reported in Table 5.1.

This agrees reasonably well with the inclusive one-neutron removal cross section of $65 \pm 6$ mb for $^{16}$C recently measured at 55 MeV/nucleon by Sauvan et al.[Sau00]
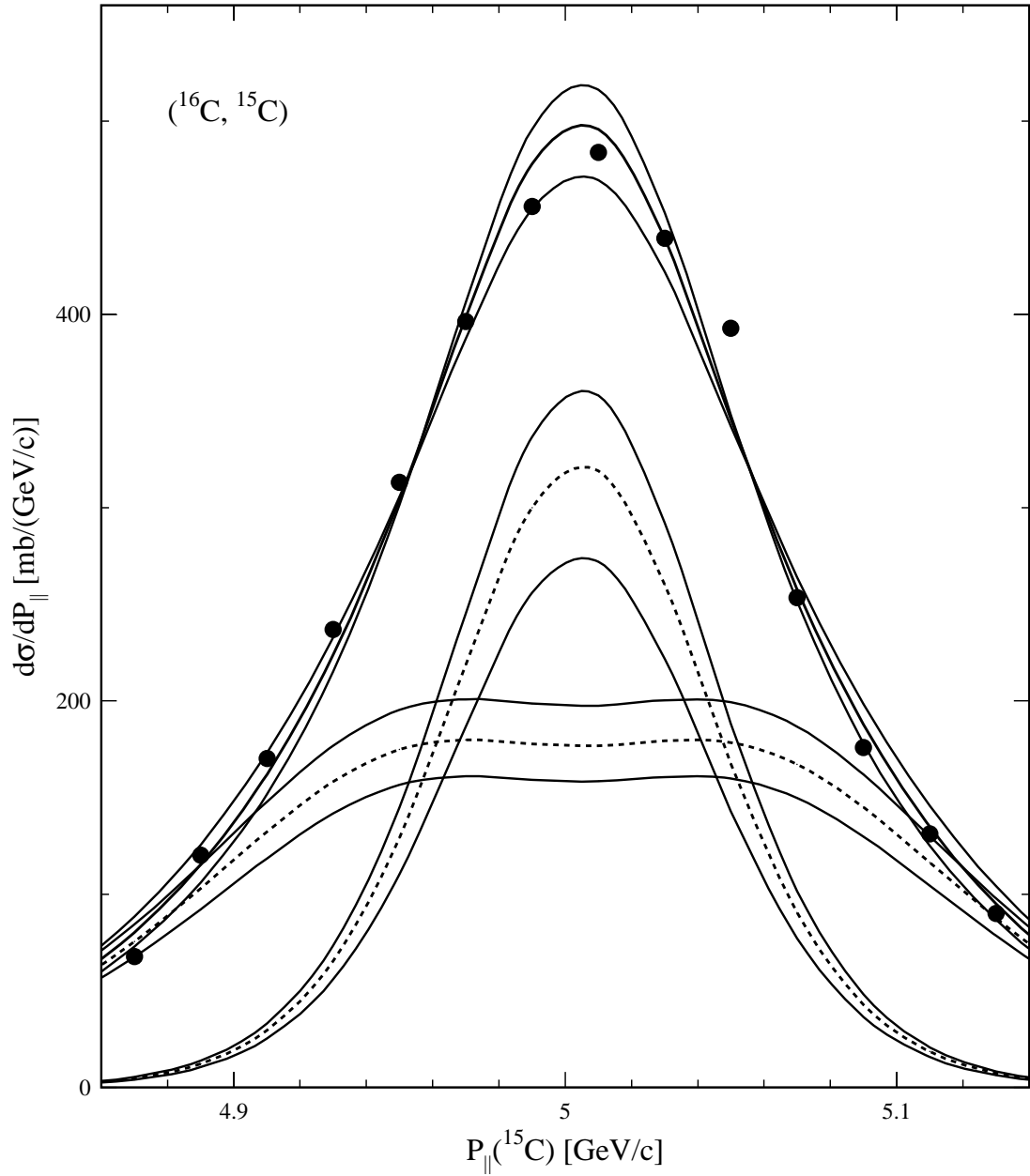
Figure 5.2: Inclusive longitudinal momentum distribution of the $^{15}$C fragments produced in one-neutron removal reactions of $^{16}$C on a $^9$Be target. The experimental errors are smaller than the size of the points. The full-drawn line is a fit with the short-dashed lines showing the individual theoretical components. The thin lines indicate the error limits allowed by the fit. The broad component corresponds to $58 \pm 6\%$ $d$–wave and the narrow one to $42 \mp 6\%$ $s$–wave, with the contributions from the (unobserved) tails of the $d$–wave distribution taken into account.

and their calculated value of 75 mb is essentially identical with ours. The resulting intensity of the broad ($d$–wave) component gave $58 \pm 6\%$ excited state contribution to the cross section. This is twice the value obtained from the analysis of coincident $\gamma$ rays and suggests that the simulation of the delayed events overestimated the $\gamma$ detection efficiency.

Table 5.1 compares the measured partial cross sections with the theoretical results obtained as the product of the spectroscopic factor and the single-particle cross section following Eq. 3.1. For the case of $^{16}$C, it was also necessary, as in [Nav00], to take into account the radial mismatch factor arising from the difference in single-particle potential between the two nuclei. This is not included in the shell-model calculations used here. The effective neutron separation energies (to which the wave function must be adjusted) are for $^{15,16}$C, respectively, 1.22 and 4.25 MeV for the $s$–state and 0.48 and 4.99 MeV for the $d$–state. In the table the correction has been included in the theoretical partial cross sections with the values 0.897 and 0.948. The non-overlap effect is less important for the $\ell = 2$ state, which is already spatially constrained by the angular momentum barrier. For the direct comparison with the shell-model occupancies of the $^{16}$C neutron pair, the experimental cross sections must be divided by the corresponding single-particle cross sections and mismatch factors, to obtain the spectroscopic factors $C^2 S^*_{exp}$ corresponding to the quantities defined in [Nav00]. The resulting values and experimental error limits are $0.56 \pm 0.10$ ($\frac{1}{2}^+$) and $1.28 \pm 0.20$ ($\frac{5}{2}^+$). They are in excellent agreement with the theoretical spectroscopic factors 0.60 and 1.23, respectively.

## 5.2  The projectile $^{17}$C

### 5.2.1  Previous theoretical and experimental work

The levels of $^{17}$C have been studied by Fifield et al. [Fif82] in the multi-nucleon transfer reaction $^{48}$Ca$(^{18}$O,$^{17}$C$)^{49}$Ti. The lowest state, interpreted as the ground state, has a neutron separation energy of $0.729 \pm 0.018$ MeV [Aud93, Aud97] based on this and a previous measurement. Fifield et al. found a cross section five times larger to a level at 0.395 MeV. The analysis by Warburton and Millener [War89] interprets this as the $\frac{5}{2}^+$ state, expected to be favored in a two-step transfer reaction; see for example [Cat89]. Their analysis of the beta decay data for $^{17}$N [Duf86, Cur86] supports this conclusion and allows the $\frac{5}{2}^+$ ground-state assignment to be "eliminated model-independently". Of the remaining likely spin-parity assignments for the ground state, $\frac{1}{2}^+$ and $\frac{3}{2}^+$, they prefer the latter, but both remain "quite possible". Several theoretical papers [Sme99, Cha00, Des00] have dealt with the one-neutron removal reactions on $^{17}$C.

### 5.2.2  Present shell-model results

As discussed in section 3.1, the WBP and WBT interactions both present a triplet of low-lying states for $^{17}$C. The present experimental results are in agreement only with the spectroscopic factors based upon the $\frac{3}{2}^+$ ground state. The WBP interaction gives a $\frac{3}{2}^+$ ground state and this will be used for further comparisons. However, for the given spin-parity of $\frac{3}{2}^+$ the spectroscopic factors are very similar between WBP and WBT.

With the WBP interaction, the largest components of the $^{17}$C $\frac{3}{2}^+$ state are 32% for $[(0p_{3/2})^8, (0p_{1/2})^2, (0d_{5/2})^3]$ and 31% for $[(0p_{3/2})^8, (0p_{1/2})^2, (0d_{5/2})^2, (1s_{1/2})^1]$, with the remaining 37% in small components. The $0d_{3/2}$ component is small resulting in

$C^2S(0d_{3/2}) = 0.035$ for the $^{17}$C $\frac{3}{2}^+$ state to the $^{16}$C $0^+$ ground state. As discussed in the next section, the strongest $sd$ spectroscopic factors are to the excited $2^+$ state in $^{16}$C. The consequences and interpretation of this unusual situation will be discussed.

### 5.2.3 Experimental results

The Doppler-corrected $\gamma$-ray spectrum from the decay of the $^{16}$C residues produced in one-neutron knockout reactions from $^{17}$C is shown in Fig. 5.3. The simplified level scheme of $^{16}$C, based on [Bal77, Til93], is sketched in Fig. 5.5.

The $\gamma$ peak at 1.77 MeV arises in the decay from the first $2^+$ level at 1.77 MeV to the $^{16}$C ground state. The broad peak near 2.3 MeV is assumed to represent decays from the three (unresolved) levels near 4.1 MeV to the $2^+$(1.77 MeV) state. The background was parameterized as an exponential, as in Fig. 5.1 and Refs. [Aum00, Nav00]. The resulting curve was compared to the measured continuum from the $^{12}$Be and $^{16}$C data (section 2.4.2, Fig. 2.7) and found to be in agreement, as shown in Fig. 5.4.

The total experimental spectrum was fitted with the individual response functions obtained from the Monte Carlo simulations superimposed on the background. This leads to the branching ratios $b_{exp}$ given in Table 5.2.

The branch to the ground state of 19$\pm$9% was obtained from an intensity balance; since this relatively large cross section disagrees with the shell-model calculations, it has been examined whether the number would be consistent with zero. However, from the following analysis a substantial branch to this state has been found to be definitely present.

An alternative explanation for the relatively strong cross section to the ground state would be the presence of unobserved $\gamma$ rays, which would distort the intensity
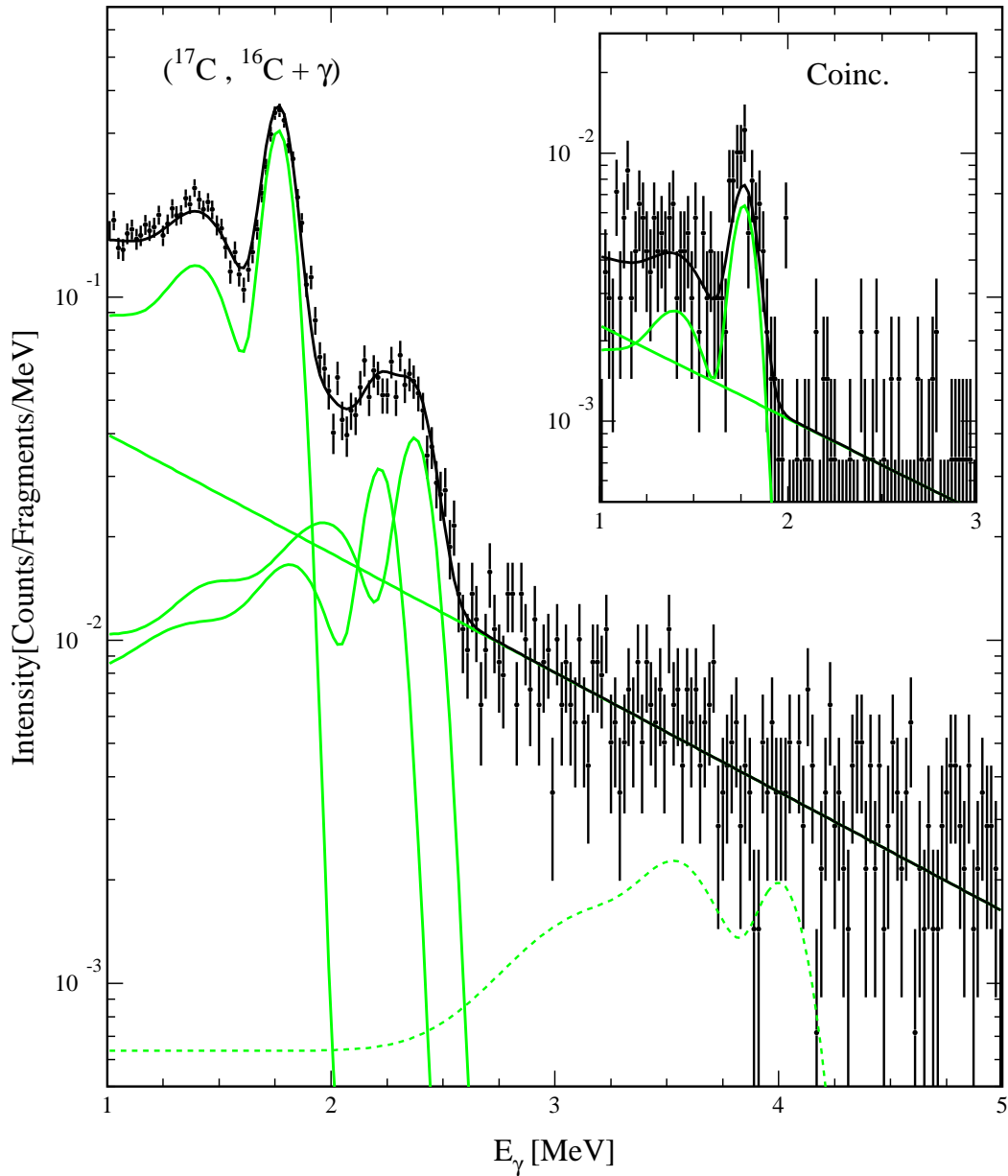
Figure 5.3: Doppler-corrected $\gamma$-ray spectrum measured in ${}^9$Be(${}^{17}$C, ${}^{16}$C+$\gamma$)X. The black curve is a fit to the spectrum using an exponential curve for the background and response functions (grey curves) for each of the $\gamma$-ray transitions shown in the simplified level scheme of Fig. 5.5. The dashed line corresponds to an estimated upper limit of 2% for the direct transition from the $J = 2$ level at 3.99 MeV to the ground state. Inset: $\gamma$ spectrum gated on the transitions between the levels at $\simeq 4$ MeV and the $2^+$ level at 1.77 MeV. The spectrum was fitted using the same procedure as described above.
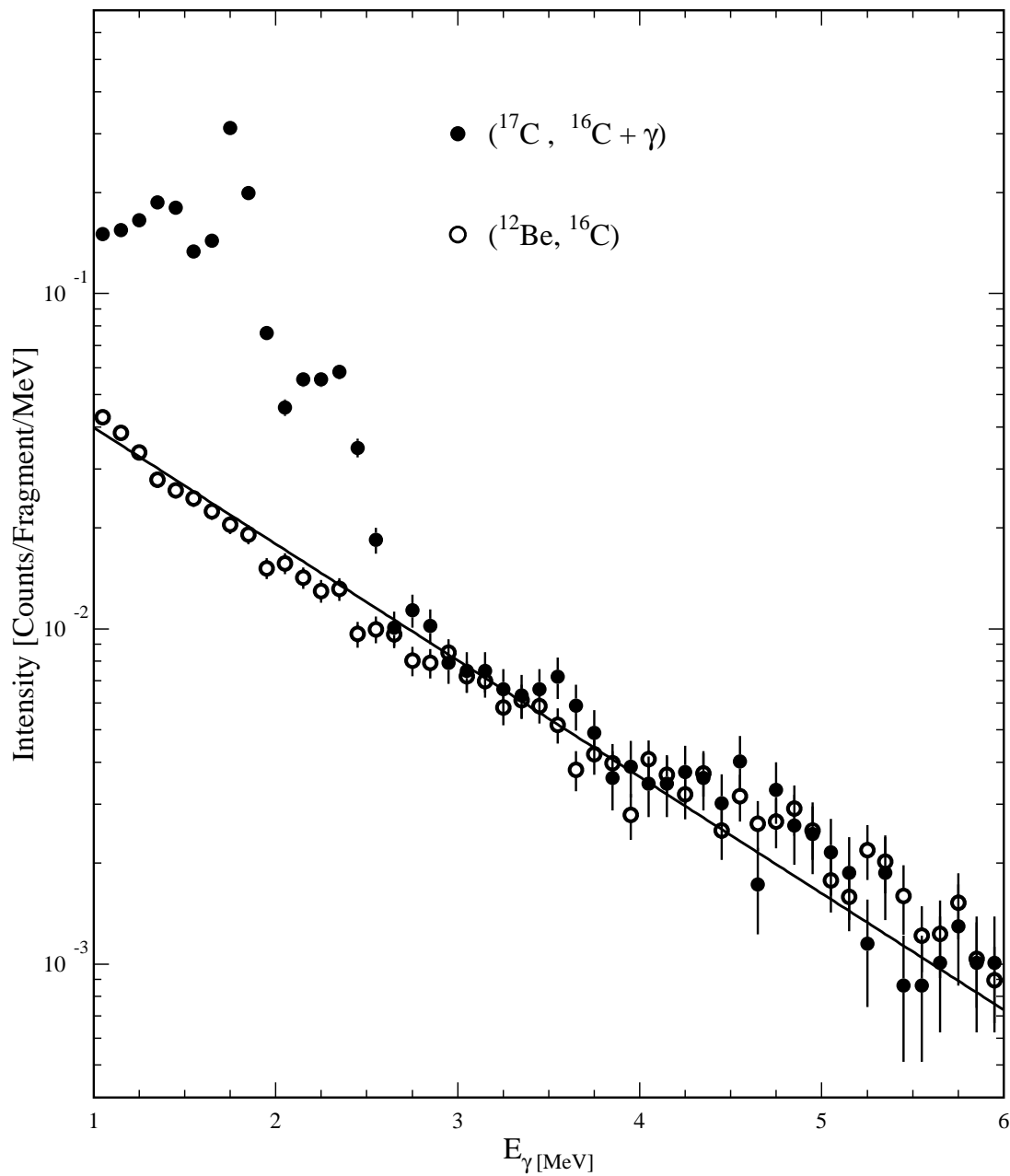
Figure 5.4: Comparison between the $\gamma$-ray spectrum from the excited $^{16}$C residues after one-neutron removal reactions on $^{17}$C, and the measured continuum distribution extracted from the analysis of the $^{12}$Be and $^{16}$C data. The solid line is the result from the fit of the spectrum.

Table 5.2: Partial cross sections $\sigma$ and branching ratios $b$ for the final states $I^\pi$ in the residues produced in $^9\text{Be}(^{17}\text{C},^{16}\text{C})\text{X}$ at $E = 62$ MeV/nucleon. The theoretical cross sections $\sigma_{th}$ are calculated from Eq. (3.1) using the WBP spectroscopic factors $C^2S$ and the single-particle cross sections $\sigma_{sp}$. * The components of this group have been analyzed together. We identify them with three states predicted by theory in the range 4.9-5.7 MeV. The main contributions were given by at least two components.

| $(^{17}\text{C},^{16}\text{C})$ | $E$ [MeV] | $I^\pi$ [$\hbar$] | $\ell$ [$\hbar$] | $C^2S$ | $\sigma_{sp}$ [mb] | $\sigma_{th}$ [mb] | $\sigma_{exp}$ [mb] | $b_{th}$ [%] | $b_{exp}$ [%] |
|---|---|---|---|---|---|---|---|---|---|
| | 0.0 | $0^+$ | 2 | 0.03 | 53 | 2 | 22±11 | 2 | 19 ± 9 |
| | 1.77 | $2^+$ | 0 | 0.16 | 75 | 12 | 16±7 | 12 | 14 ± 6 |
| | | | 2 | 1.44 | 37 | 53 | 44±11 | 53 | 38 ± 8 |
| | | | sum | | | 65 | 60±12 | 65 | 52 ± 8 |
| | 4.1* | $2, 3^{(+)}, 4^+$ | 0 | 0.22 | 50 | 11 | 2±2 | 11 | 2 ± 2 |
| | | | 2 | 0.76 | 29 | 22 | 31±7 | 22 | 27 ± 5 |
| | | | sum | | | 33 | 33±7 | 33 | 29 ± 5 |
| $\sigma_{tot}$ | | | | | | 100 | 115±14 | | |

balance. Two possibilities were examined. The first would be a small direct branch to the ground state from the $J = 2$ level near 4 MeV. An upper limit of 2% was estimated as shown by the dashed curve in Fig. 5.3. This is consistent with shell-model calculations. Another possibility would be that part of the intensity in the broad peak near 2.3 MeV would arise from a state of this energy decaying directly to the ground state. (No such state is known or expected [Til93].) Such a $\gamma$ ray clearly would not be in coincidence with the 1.77 $\gamma$ ray, while the other 2.3 MeV $\gamma$ rays are followed by this to 100%. This possibility has been examined by searching for triple coincidences (residue-$\gamma$-$\gamma$) in the data. With a gate on E$_\gamma \simeq 2.3$ MeV the spectrum, shown as an inset in Fig. 5.3, was obtained and fitted with the response function for the 1.77 MeV $\gamma$ ray and an exponential background. The result was then compared on a quantitative basis with an event-by-event simulation generated with a $\gamma$ ray from the first excited level at 1.77 MeV produced simultaneously with a $\gamma$ ray from one of

the three levels at $E \simeq 4.1$ MeV. The ratio between the experimental intensity for the coincident events and the intensity obtained in the simulation was $105 \pm 15\%$. The error limit would allow for at most a 5% (absolute) feeding of the ground state via such a mechanism, rather unlikely in the first place. These results support the level scheme assumed in the right side of Fig. 5.5 and the branching ratios for the knockout cross section given in Tables 5.2 and 5.3.

Yet another experimental effect that, at least in principle, might call the normalization into question and explain the enhanced cross section to the $^{16}$C ground state would be the presence of the spin-parity $\frac{1}{2}^{+}$ state of $^{17}$C as a contaminant isomer in the beam. This state has a reaction cross section that goes predominantly to the ground state of the residue; see Table 5.3. In connection with the analysis of the $^{16}$C experiment (section 5.1.3), where a half-life of a few ns gave a mean flight path for the residues of 0.34 m, a half-life that were a factor 100 or more longer would allow isomers produced in the primary production target of the A1200 fragment separator to react with the target and reach the S800. Since the position of the $\frac{1}{2}^{+}$ state is unknown but presumably low in energy, such a long half-life is entirely possible. However, as will be discussed below, the momentum distribution belonging to this component would have a very characteristic $\ell = 0$ shape in contradiction with the experiment, which gives $\ell = 2$, as shown in Fig. 5.5. Hence also this explanation can be excluded.

The inclusive longitudinal momentum distribution of the $^{16}$C residues was measured and found to be consistent with earlier measurements [Baz95, Baz98, Bau98]. The estimated angular acceptance correction was 3.6%. From the $\gamma$ coincidence information, the distribution could be separated into three components corresponding to feeding of the ground state, the $2^{+}$ level, and the 4.1 MeV group of levels (Fig. 5.5).
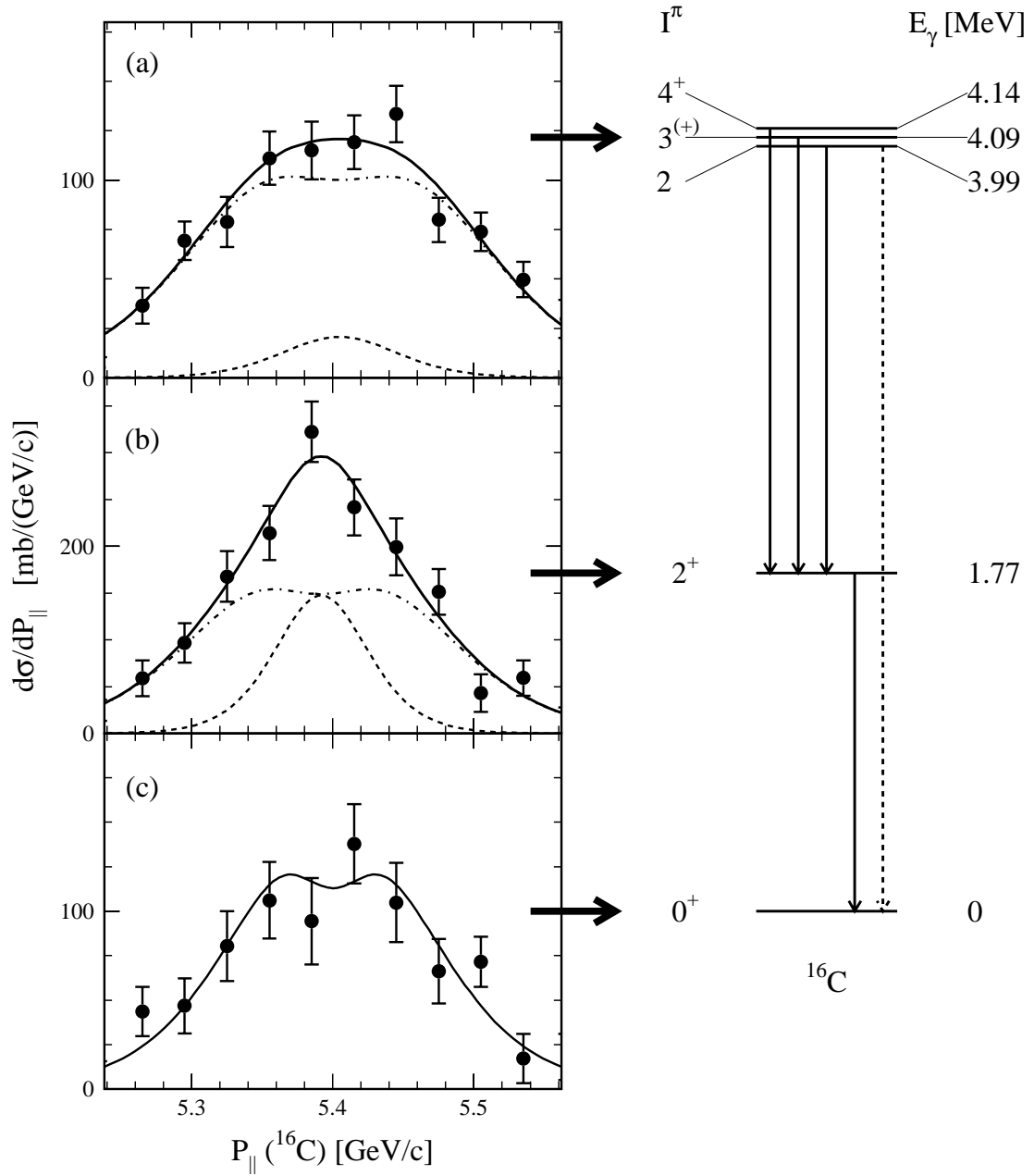
Figure 5.5: Longitudinal momentum distributions corresponding to the states indicated in the simplified level scheme of $^{16}$C. (a), (b): The solid curves are the calculated momentum distributions with a mixture of $s-$ and $d-$waves shown as dashed and dot-dashed lines, respectively (8% $s$ and 92% $d$ in (a), 26% $s$ and 74% $d$ in (b)). (c): The solid curve is the calculated momentum distribution of a pure $d-$wave.

74

In view of the relatively large error on the intensity of the ground-state branch, obtained by subtracting an 81% correction from the inclusive spectrum, it is important to note that the shape has been observed to remain stable within the error limits given. The reason for this is that the shapes for the excited levels are very similar, all three being dominated by $\ell = 2$ components. The distributions were fitted with theoretical momentum distributions as described in section 3.2 assuming $\ell = 0, 2$ components, in the momentum range corresponding to the $\pm$ 2.5% instrumental momentum acceptance. The most interesting result was found for the distributions to the excited states, which are an admixture of $s$– and $d$–waves, with a dominant $d$–wave character in both cases (92 $\pm$ 8% for the 4.1 MeV group of levels, and 74 $\pm$ 10% for the $2^+$ state). This is the second case of a cross section with mixed $\ell$–values observed in our experiments. (The reaction $^9$Be($^{14}$B,$^{13}B_{gs}$)X was found [Gui00] to be predominantly $\ell = 0$ with an 11 $\pm$ 3% $\ell = 2$ admixture.) Finally, the cross section to the $^{16}$C ground state is essentially $\ell = 2$. The total inclusive cross section, after extrapolation of momentum acceptance losses (estimated to be 2.4%), is 115$\pm$14 mb, about two standard deviations above the value of 84 $\pm$ 9 mb measured [Sau00] at 49 MeV/nucleon. The information supplied by the momentum distributions has made it possible to subdivide the measured cross section to the 1.77 MeV level into the $\ell$ components given in Tables 5.2 and 5.3. This evidence is now compared with the theoretical calculations.

The literature basically leaves two options for the $^{17}$C spin, $\frac{1}{2}^+$ and $\frac{3}{2}^+$, as summarized in the previous subsection. The absence of an $\ell = 0$ reaction to the $^{16}$C ground state is basically enough to fix the spin as $\frac{3}{2}^+$. This is actually the assignment that is proposed here and the one used in the discussion of the structure and spectroscopic factors in Table 5.2. However, to demonstrate that the spectroscopic factors measured in the present work allow on their own a unique determination of the spin, the predicted cross sections and branching ratios for assumed spin-parity assignments of

Table 5.3: The reaction $^9$Be($^{17}$C,$^{16}$C)X at $E = 62$ MeV/nucleon, for a $^{17}$C ground-state spin $J^\pi = 5/2^+$ or $1/2^+$, see Table 5.2. * The components of this group have been analyzed together. We identify them with three states predicted by theory in the range 4.9-5.7 MeV. The main contributions were given by at least two components.

| $J^\pi(^{17}C)$ | $E[MeV]$ [MeV] | $I^\pi$ [$\hbar$] | $\ell$ [$\hbar$] | $C^2S$ | $\sigma_{sp}$ [mb] | $\sigma_{th}$ [mb] | $\sigma_{exp}$ [mb] | $b_{th}$ [%] | $b_{exp}$ [%] |
|---|---|---|---|---|---|---|---|---|---|
| $\frac{5}{2}^+$ | 0.0 | $0^+$ | 2 | 0.70 | 53 | 37 | 22±11 | 35 | 19 ± 9 |
| | 1.77 | $2^+$ | 0 | 0.10 | 75 | 8 | 16±7 | 7 | 14 ± 6 |
| | | | 2 | 0.22 | 37 | 8 | 44±11 | 7 | 38 ± 8 |
| | | | sum | | | 16 | 60±12 | 14 | 52 ± 8 |
| | $4.1^*$ | $2, 3^{(+)}, 4^+$ | 0 | 0.39 | 50 | 20 | 2±2 | 19 | 2 ± 2 |
| | | | 2 | 1.16 | 29 | 34 | 31±7 | 32 | 27 ± 5 |
| | | | sum | | | 54 | 33±7 | 51 | 29 ± 5 |
| $\sigma_{tot}$ | | | | | | 107 | 115±14 | | |
| $\frac{1}{2}^+$ | 0.0 | $0^+$ | 0 | 0.64 | 148 | 95 | 22±11 | 57 | 19 ± 9 |
| | 1.77 | $2^+$ | 2 | 0.39 | 37 | 14 | 60±12 | 9 | 52 ± 8 |
| | 3.03 | $0^+$ | 0 | 0.29 | 59 | 17 | – | 10 | – |
| | $4.1^*$ | $2, 3^{(+)}$ | 2 | 1.39 | 29 | 40 | 33±7 | 24 | 29 ± 5 |
| $\sigma_{tot}$ | | | | | | 166 | 115± 14 | | |

$\frac{1}{2}^+$ and $\frac{5}{2}^+$ are shown in Table 5.3.

The former is clearly excluded by the predicted dominance of $s-$wave knockout to the ground state with only weak branches to the excited states, both contradicted by experiment. Calculations for the case $J^\pi = \frac{5}{2}^+$, also listed in Table 5.3, are also in disagreement with experiment, which has the main cross section to the 1.77 MeV $2^+$ level and smaller branches to 0 and $\approx 4.1$ MeV. The pattern predicted for an initial spin-parity of $\frac{5}{2}^+$ is exactly opposite. Only the $J^\pi = \frac{3}{2}^+$ assignment for $^{17}$C explains that the main part of the cross section goes to the 1.77 MeV $2^+$ and about half as much to the 4.1 MeV group. Contrary to the statement made in [Sau00], an $\ell = 2$ momentum distribution and the inclusive cross section are insufficient for determining the ground-state spin and parity of $^{17}$C as $J^\pi = \frac{3}{2}^+$. The only remaining difficulty

is that the cross section to the ground state of $^{16}$C of 22 mb is roughly one order of magnitude larger than expected. It has been argued above that this does not appear to be an experimental problem.

It is probably useful at this point to sum up in simple language some of the structural information conveyed by the $^{17}$C results in Table 5.2. The $\frac{3}{2}^+$ ground state may be thought of as having three components, of which the main one is $0d_{5/2} \otimes [0d_{5/2}^2]_{2^+}$. This accounts for the dominant $\ell = 2$ knockout to the $2^+$ state. The smaller $\ell = 0$ component to the same state arises from a small admixture of $1s_{1/2} \otimes [0d_{5/2}^2]_{2^+}$. There is excellent agreement between experiment and theory for both components. The predicted small cross section to the $^{16}$C ground state comes from a small amount of $0d_{3/2} \otimes [0d_{5/2}^2]_{0^+}$ in the $^{17}$C ground state and a simple explanation for the experimental result would be that theory for some reason underestimates this component. There are, however, other possibilities.

The theory for calculating the cross sections, outlined in section 3.2, assumes explicitly that the only reaction mechanism is the direct removal of a bound nucleon from a core of nucleons, which is otherwise a spectator. It is, however, possible to have contributions from other (higher order) mechanisms, such as the collective contributions, of order 10 mb, invoked to account for part of the ($^{11}$Be,$^{10}$Be) cross sections in [Aum00]. Another possibility, recently investigated by Al-Khalili [AlK00] is to allow the nucleon-target interaction to induce transitions between different single-particle states or between different $m$ components of the same state. This mechanism, for the main $0d_{5/2} \otimes [0d_{5/2}^2]_{2^+}$ component discussed here, requires a spin-flip $0^+$ recoupling of the two unstripped neutrons, and is estimated to contribute less than 1 mb.

## 5.3 The projectile $^{19}$C

### 5.3.1 Previous experimental and theoretical work

The isotope $^{19}$C occupies a position in the nuclear chart similar to that of $^{11}$Be, and it has attracted much interest as a possible second candidate for a well developed one-neutron halo state. This was suggested by the low adjusted value [Aud93] of its one-neutron separation energy, $S_n = 0.16 \pm 0.11$ MeV. This number represents the weighted average of measurements carried out at Los Alamos and GANIL [Wou88, Orr91]. The value of 0.24 MeV often encountered in the literature includes, in addition, two earlier and less precise measurements by the same groups in the weighted average.The adjustment [Aud97] normally excludes such results from its recommendation. Indirect evidence discussed below suggests that a value larger than 0.16 MeV, i.e., 0.5-1.0 MeV, is required to interpret the data in a consistent way.

Several previous experiments have investigated the structure of $^{19}$C by measuring the longitudinal momentum distributions of the core fragments $^{18}$C [Baz95, Baz98, Bau98]. The narrow widths observed in these experiments resemble those found for $^{11}$Be and were suggestive of a halo structure. They were, however, wider than the adjusted neutron separation energy value would allow, which prompted speculations that the $^{19}$C ground state is dominated by complex-structure components. Bazin et al.[Baz95, Baz98], however, pointed out that the momentum distribution in the Coulomb breakup of $^{19}$C could be understood if the neutron separation energy was about 0.6 MeV. An experiment by Marqués et al.[Mar96] observed neutrons from $^{19}$C breakup reactions in which neutrons were detected in coincidence with charged fragments with charge five and lower. They found a broad component in the angular distribution, which they associated with nucleus-nucleus collisions. A narrow component with a Lorentzian width parameter $\Gamma$ of 55 MeV/c was taken as evidence for a

halo neutron present as a spectator in the collision.

A recent experiment on the Coulomb dissociation of $^{19}$C on a lead target by Naka-mura et al. [Nak99] represents a decisive step forward. They found that the angular distribution of the decaying $^{18}$C+n system required a neutron separation energy $S_n$ of $0.53 \pm 0.13$ MeV. With this energy they could also understand the differential cross section as a function of the relative energy of the dissociation products, which was not the case for a value of 0.16 MeV. The absolute Coulomb cross section (neglecting possible contributions to excited levels, discussed below) leads to a spectroscopic factor of 0.67, thus showing that the dominant character of the $^{19}$C ground state is $1s_{1/2} \otimes 0^+$. Since this analysis does not correct for branches to excited states, which are expected to be present, also for the Coulomb part of the cross section, the results should be taken as qualitative.

Interaction cross section measurements have also been reported for $^{19}$C on $^{12}$C at 960 MeV/nucleon [Oza98]. The analysis of these data in a few-body Glauber theory approach has shown [Tos99a] that the measured $\sigma_I$ are consistent with a $J^\pi = \frac{1}{2}^+$ $^{19}$C ground state, while excluding $J^\pi = \frac{3}{2}^+$ and $J^\pi = \frac{5}{2}^+$ assignments. In particular, the $\sigma_I$ datum was found to be consistent with a dominant $1s_{1/2} \otimes 0^+$ configuration for separation energy values ranging between 0.12 and 0.65 MeV, with spectroscopic factors between 0.7 and 1.0. This result is consistent with the separation energy value found from the Coulomb dissociation experiment [Nak99] and with the results reported below.

A number of papers have discussed the structure and reactions of $^{19}$C, primarily in the light of particle-core coupling models [Rid97, Rid98, Ban98, Sme99, Bon99, Cha00, Des00, Kan00]. Smedberg and Zhukov [Sme99] attempted to account for a perceived difference in longitudinal momentum widths observed at 77 MeV/nucleon

[Baz95, Baz98] and at 910 MeV/nucleon [Bau98]. They invoked an additional reaction mechanism involving an unspecified intermediate resonance just above the $^{18}$C+n threshold. This hypothesis does not find support in the present work, where the 62 and 910 MeV/nucleon data are analyzed in more detail below. In another analysis, Kanungo et al. [Kan00] found it difficult to reconcile the $^{19}$C momentum distributions at the two energies with the measured interaction cross section. As a remedy they proposed that the core of $^{19}$C is considerably larger than that of free $^{18}$C.

## 5.3.2 Present shell-model results

Shell-model calculations [Bro88] predict the presence of three bound states above the ground state of $^{18}$C. There are two $2^+$ levels at 2.1 MeV (observed experimentally at $1.62 \pm 0.02$ [Fif82]) and at 3.4 MeV. A $0^+$ level at 4.0 MeV, just below the neutron threshold of 4.2 MeV, is expected to decay by a cascade of 1.6 and 2.4 MeV $\gamma$ rays, and it has a large $\ell = 0$ spectroscopic factor that would contribute noticeably to the Coulomb cross section. There are two more states ($2^+$, $3^+$) close in energy, near 4.9 MeV, which are included in the analysis, observing that the calculations tend to overestimate the level energies by several hundreds of keV. The lowest levels in $^{19}$C are predicted to be ($\frac{5}{2}^+$,0.00), ($\frac{1}{2}^+$,0.05), ($\frac{3}{2}^+$,0.40) with energies in MeV. In the following the spin-parity assignment for the ground state is assumed to be established by the Coulomb dissociation experiment [Nak99]. It will be seen below that the same conclusion can be reached independently from our data. The spectroscopic factors obtained with the WBP parameters [Bro88] are given in Table 5.4, where the 3.4 MeV level, for which the spectroscopic factors are small (total 0.10 for $\ell = 2$), is left out.

As discussed in section 3.1, the WBP and WBT interactions both present a triplet of low-lying states for $^{19}$C. The present experimental results are in agreement only with the spectroscopic factors based upon the $\frac{1}{2}^+$ ground state. The WBP interaction

gives a $\frac{1}{2}^+$ ground state and this will be used for further comparisons. However, for the given spin-parity of $\frac{1}{2}^+$, the spectroscopic factors are very similar between WBP and WBT.

With WBP the largest component of the $^{19}$C ground state $\frac{1}{2}^+$ is 48% for the configuration $[(0p_{3/2})^8, (0p_{1/2})^2, (0d_{5/2})^4, (1s_{1/2})^1]$, with the remaining 52% in smaller components. The $[(0d_{5/2})^4, (1s_{1/2})^1]$ configuration appears at an excitation energy of 1.33 MeV in $^{21}$O with the USD interaction [Bro88], and may be associated with an experimental state observed at the same energy [Cat89]. In the framework of WBP (and WBT) its energy is lowered in $^{19}$C due to the 1.6 MeV downward shift of the $1s_{1/2}$ state relative to $0d_{5/2}$ between $^{17}$O and $^{15}$C.

### 5.3.3 Experimental results

In spite of the low intensity of the incident $^{19}$C ($\simeq 0.5 - 1$ particles/sec), enough information was collected in different reaction channels to confirm that its ground state is a well developed halo state. This evidence is discussed in the following, first the $\gamma$-coincidence information leading to the ground state partial cross section and exclusive momentum distribution, second the inclusive momentum spectrum, and, third, the exclusive cross section for Coulomb dissociation to the $^{18}$C ground state. The evidence combines to give a consistent set of parameters for the halo state.

The $\gamma$-ray spectrum in coincidence with projectile residues had too little statistics for it to be analyzed with the peak-fitting procedure used in the case of $^{17}$C. Instead, all $\gamma$ rays above 0.25 MeV were used as a tag identifying $\gamma$-coincident events and a correction based on the average $\gamma$ efficiency to the residual noncoincident events was applied. (This was the experimental approach taken previously in our work on the phosphorus isotopes [Nav98].) The branching ratio listed in Table 5.4 and the ground-state momentum distribution shown in Fig. 5.6 were then obtained as follows.

Figure 5.6: Longitudinal momentum distribution corresponding to the ground state of the $^{18}$C residues after one-neutron removal from $^{19}$C on a $^9$Be target. The coincidences with $\gamma$ rays have been used to correct the inclusive distribution for contributions from excited levels. The momentum distribution corresponding to the extracted separation energy $S_n = 0.8$ MeV is represented by the solid line. The dashed lines represent the momentum distributions corresponding to separation energies of 0.5 and 1.1 MeV. The dot-dashed curve is calculated for a $d$–state for a separation energy of 0.8 MeV.

Table 5.4: Partial cross sections $\sigma$ and branching ratios $b$ for the final states $I^\pi$ in the residues produced in $^9\text{Be}(^{19}\text{C},^{18}\text{C})\text{X}$ at $E = 57$ MeV/nucleon. The theoretical cross sections $\sigma_{th}$ are calculated from Eq. (3.1) using the WBP spectroscopic factors $C^2S$ and the single-particle cross sections $\sigma_{sp}$. The neutron separation energy of $^{19}\text{C}$ was assumed to be 0.8 MeV. * All excited states in $^{18}\text{C}$ were analyzed as one group. The energy 1.6 MeV for the $2^+$ is the experimental value; the WBP calculation gives 2.16 MeV.

| $(^{19}\text{C},^{18}\text{C})$ | $E$ [MeV] | $I^\pi$ [$\hbar$] | $\ell$ [$\hbar$] | $C^2S$ | $\sigma_{sp}$ [mb] | $\sigma_{th}$ [mb] | $\sigma_{exp}$ [mb] | $b_{th}$ [%] | $b_{exp}$ [%] |
|---|---|---|---|---|---|---|---|---|---|
| | 0.0 | $0^+$ | 0 | 0.58 | 136 | 79 | 148±50 | 46 | 56 ± 9 |
| | 1.6* | $2^+$ | 2 | 0.48 | 34 | 16 | | | |
| | 4.0* | $0^+$ | 0 | 0.32 | 45 | 14 | | | |
| | 4.9* | $2^+,3^+$ | 2 | 2.44 | 26 | 63 | | | |
| | | | sum | | | 93 | 116±45 | 54 | 44 ± 11 |
| $\sigma_{tot}$ | | | | | | 172 | 264±80 | | |

As discussed in section 2.4.2, a structureless continuum distribution that depends approximately exponentially on the energy, lies below the experimental $\gamma$-ray spectra. With an integral cutoff at 0.25 MeV, the intensity of this per fragment is approximately 9%, consistent in all the cases studied, and the corresponding coincident momentum distribution is very similar to that of the inclusive spectrum. The average detection efficiency for the excited levels was calculated in the GEANT Monte Carlo simulations and gave the results of section A.1.4. The resulting branching ratio to the ground state was $56 \pm 9$%, consistent within the error with the result that would be obtained if the theoretically predicted levels near 4 MeV were not populated, i.e., if they were above the neutron threshold. The branching ratio has been corrected for the momentum acceptance of the spectrometer, which eliminates the "tails" of the momentum distributions, especially for the $\ell = 2$ component. The corrections are based on the theoretical momentum distributions for a neutron separation energy of 0.8 MeV and assumed the theoretical branching ratios of the excited states. This

leads to the partial cross section of $148 \pm 50$ mb, a large value typical of a halo state.

The analysis based on integral-bias $\gamma$ tagging also leads to the ground-state momentum distribution shown in Fig. 5.6, narrow and consistent with an $s$–state halo structure. The calculations are based on the black-disk model discussed above. Together with the large partial cross section this proves the ground-state spin-parity of $^{19}$C to be $J^{\pi} = \frac{1}{2}^{+}$, in agreement with the analyses of [Nak99, Oza98, Tos99a]. The width of the momentum distribution is quite sensitive to the separation energy; a least-squares adjustment suggests a value $S_n = 0.8 \pm 0.3$ MeV.

An alternative way of testing the dependence on the assumed value of $S_n$ is to fit the inclusive momentum distribution, i.e., without the $\gamma$ coincidence requirement, of the $^{18}$C residues. For this analysis the theoretical spectroscopic factors given in Table 5.4 are assumed. The adjusted momentum distributions for the assumed values $S_n = 0.5$ and 0.8 MeV are shown in Fig. 5.7. The result of the least-squares analysis was $S_n = 0.65 \pm 0.15$ MeV, which gives a branching ratio to the ground state of $48 \pm 2\%$ in good agreement with the $56 \pm 9\%$ obtained in the $\gamma$ coincidence analysis. This result is in quantitative agreement with the coincidence analysis of the ground state momentum distribution.

Another inclusive spectrum of the projectile residues has been obtained for $^{19}$C on a $^{12}$C target at 910 MeV/nucleon in a GSI experiment [Bau98]. This distribution is close to identical to that of Fig. 5.7, and both are marginally consistent with that given by [Baz95, Baz98], which has much poorer statistics. For this result, adjustment of a theoretical momentum distribution similar to that in Fig. 5.7 leads to a somewhat lower branch to the ground state, 40% as compared with the 48% found at our energy in the same analysis. The smaller value is to a large extent accounted for by smaller nucleon-nucleon cross sections and real-to-imaginary amplitudes at the higher
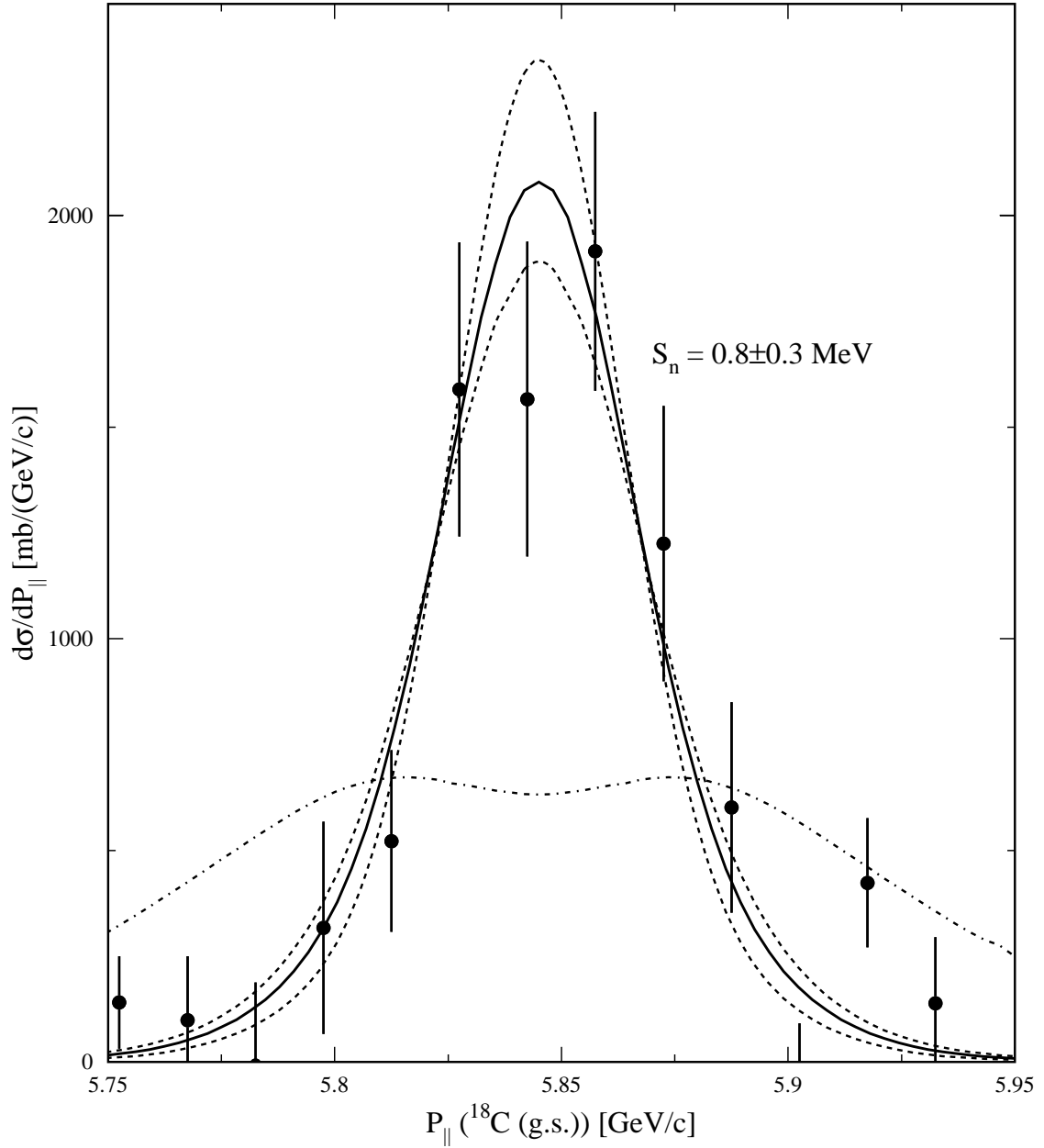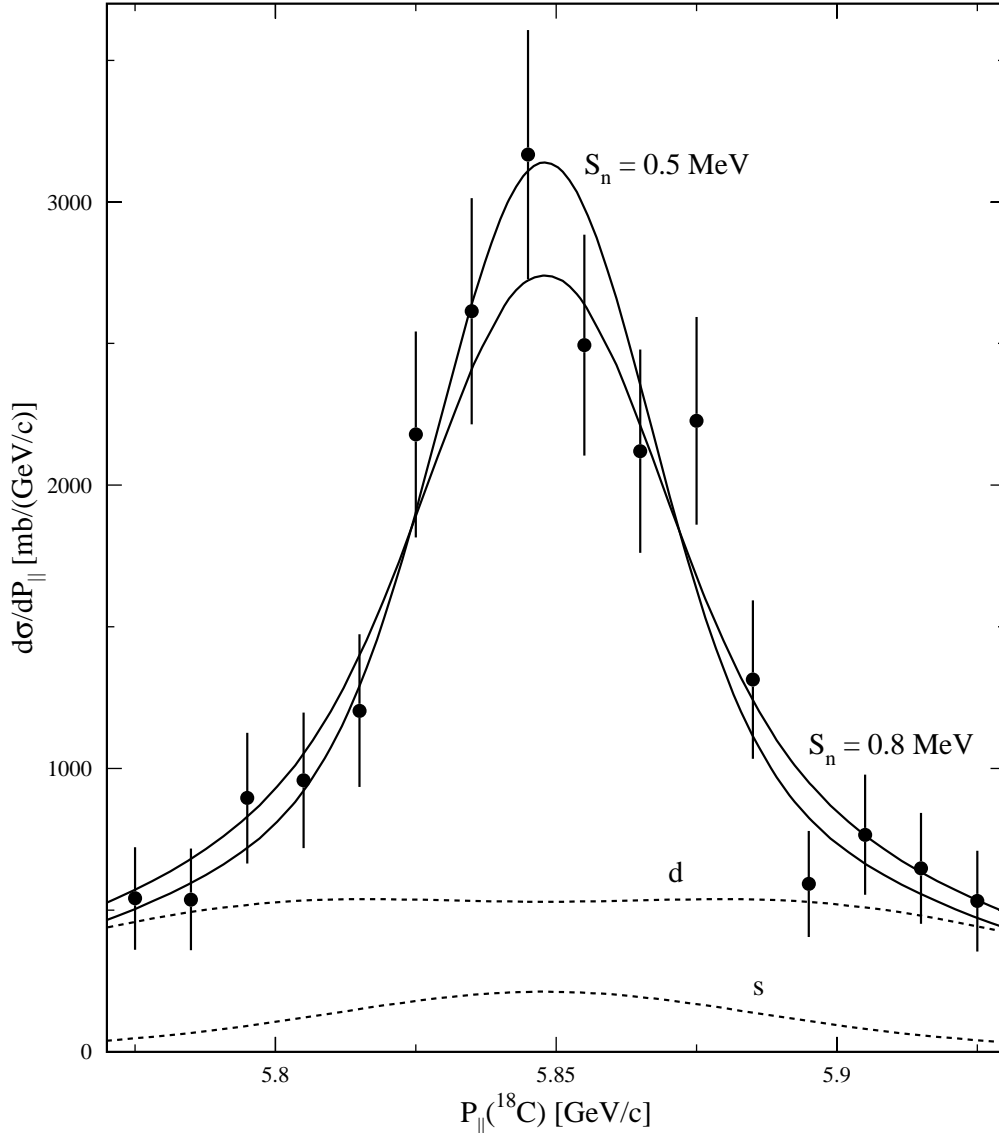
Figure 5.7: Inclusive longitudinal momentum distribution corresponding to $^{18}$C residues after one-neutron removal from $^{19}$C on a $^9$Be target. The solid lines represent the calculated inclusive momentum distributions corresponding to $S_n = 0.5$ MeV and $S_n = 0.8$ MeV obtained as a least-squares fit assuming the branching ratios given by the theoretical spectroscopic factors of Table 5.4. These values represent approximately the $\pm 1\sigma$ limits of the allowed interval and correspond to a $\chi^2$ of 8 and 9, respectively for 14 degrees of freedom. (For $S_n = 0.3$ MeV and $S_n = 1.1$ MeV $\chi^2$ increases to 18 and 14, respectively.) The dashed lines labeled with $s$ and $d$ represent the contributions from the $\ell = 0, 2$ excited states for $S_n = 0.8$ MeV. Their contributions for $S_n = 0.5$ MeV would be almost identical.

energy. An analysis for 910 MeV/nucleon on a carbon target and with the theoretical spectroscopic factors of Table 5.4 reduces the theoretical ground-state branch to 40% from the 46% obtained for a beryllium target at 57 MeV/nucleon. Therefore, the experiment of Baumann et al. [Bau98], is entirely consistent with ours.

Finally, data that had been taken for reactions of $^{19}$C on a Au target were also used to provide a constraint on the parameters. A detailed analysis is given in the second part of section A.1.4. The measured inclusive ($^{19}$C,$^{18}$C) cross section on the gold target was $1.35 \pm 0.18$ b at 56 MeV/nucleon. This is close to the value of $1.34 \pm 0.12$ b observed in the ($^{19}$C,$^{18}$C+n) channel on a lead target at 67 MeV/nucleon [Nak99]. In order to compare more precisely, an (unobserved) absorptive part, assumed to be 0.15 b, should be added to the cross section of Nakamura et al. [Nak99] (their estimate) and their Coulomb part of the cross section should be scaled by the inverse of the beam energy and by the square of the target charge number. This yields an equivalent cross section of $1.53 \pm 0.14$ b under our conditions in excellent agreement with our value of $1.35 \pm 0.18$ b. Since our experiment observed $\gamma$ rays in coincidence with the projectile residue, the $\gamma$-ray tagging method described above could be used for finding that $85 \pm 7\%$ of the total cross section connects to the ground state corresponding to an absolute value of $1.15 \pm 0.18$ b. The contribution from the continuum distribution is considerably higher from a gold target than from a beryllium target, especially at low energies. For this reason the bias setting for the tag was increased to 1 MeV. The background yield was then 12% as could be deduced from the Au($^{16}$C,$^{15}$C)X data (it would have been 4% with a Be target) and the detection efficiency was estimated (in the same fashion as for the beryllium target) to be $\epsilon_{tot} = 24.3\%$. The deduced ground-state cross section could now be compared with theoretically calculated single-particle cross sections based on the assumption that nuclear and Coulomb contributions are additive. The nuclear part was calculated as in [Tos99b] and the electromagnetic part

as in [Kal96].

It will be clear that the neutron separation energy and the ground-state spectroscopic factor both must be considered unknown parameters. The data discussed above are now used to place constraints in the $S_n$–$C^2S$ plane as shown in Fig. 5.8, where the boundaries corresponding to the five sets of input data indicate limits corresponding to plus or minus one standard deviation. Two cross-hatched areas represent limits on $S_n$. One is from the analysis of the momentum width shown in Fig. 5.6 and the other from the differential cross section $\frac{d\sigma}{d\Omega}$ as a function of the center-of-mass deflection angle [Nak99]. Two other regions of the $S_n$–$C^2S$ plane, marked with vertical and horizontal lines, denote limits obtained from the absolute partial cross sections on beryllium and gold, respectively. The Coulomb cross section is based on our value; the result of Nakamura et al. would place the curve slightly higher but still within the error band. Four of the allowed bands point to a single consistent solution corresponding to a neutron separation energy of 0.5-1.0 MeV and a spectroscopic factor of 0.5-1.0 (theoretical value 0.58). This allows the conclusion that the ground state of $^{19}$C has a well developed halo, similar to that of $^{11}$Be. The fifth band, representing the direct mass measurement, does not allow a solution consistent with the other experimental input.

Since the lack of precise knowledge of the $^{19}$C mass has been a main obstacle to our understanding of this case, it should be clear that it would be extremely valuable to have an accurate direct measurement. Still, it is probably useful at this point to summarize the indirect evidence. The analysis based on integral $\gamma$ tagging (Fig. 5.6) is free from evident systematic errors, but suffers from low statistics. This leads to the rather imprecise value of the neutron separation energy, $S_n = 0.8 \pm 0.3$ MeV, which, nevertheless, has been used for the analysis of the cross sections in Table 5.4. The values obtained from the analysis of the inclusive momentum spectrum (Fig. 5.7),
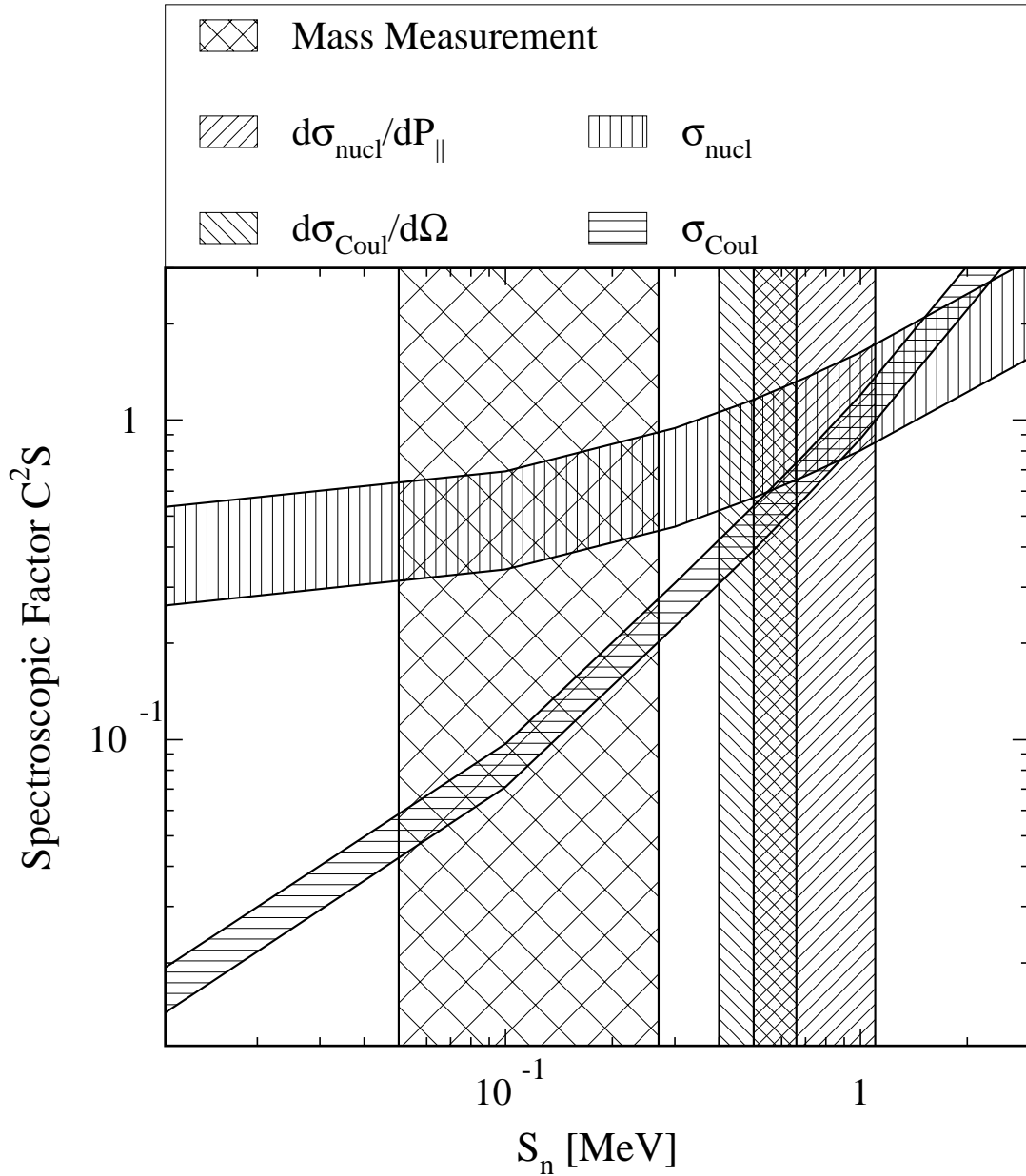
Figure 5.8: Permitted regions in the space of spectroscopic factor and one-neutron separation energy for the ground state of $^{19}$C. The hatched areas result from different information: measured nuclear and Coulomb breakup cross-sections ($\sigma_{nucl}$, $\sigma_{Coul}$), and analysis of the ground state momentum distribution ($d\sigma/dP_\parallel$). Also shown are the result from the Coulomb dissociation experiment in [Nak99], deduced from $d\sigma/d\Omega$, and the separation energy value in [Aud93, Aud97]. A consistent description of the experimental results is given for values of $C^2S$ between 0.5 and 1 and of $S_n$ between 0.5 and 1 MeV. Note that this graph does not display the two analyses of inclusive momentum distributions discussed in the text.

$0.65 \pm 0.15$ MeV, and from the Coulomb dissociation experiment by Nakamura et al. [Nak99], $0.53 \pm 0.13$ MeV, are both more appealing. They suffer, however, from uncertainties concerning the contributions from excited levels, which were taken from theory in the former case and neglected in the latter. The absolute nuclear and electric cross sections of Fig. 5.8 are again consistent with the three values given here, and all approaches give definitely larger values for the separation energy than the $0.16 \pm 0.11$ MeV based on the direct mass measurements. It would probably be premature to propose a combined value at this moment.

# Chapter 6

# Summary

In this work and in previous papers knockout reactions have been proven to offer a very promising spectroscopic tool that can test nuclear structure theory in considerable detail. This technique also has the high sensitivity that is a prerequisite for experiments with beams of rare isotopes. The best example of this, so far, is Fig. 5.8, for which the main part of the data was obtained in reactions induced by an incident (secondary) beam of $^{19}$C of slightly less than one atom per second. (The results for $^{25}$F recently presented by Sauvan et al. [Sau00] used a similar beam intensity.) This information has been sufficient for determining the spin and parity of the ground state and for showing that it is a neutron halo state with a spectroscopic factor approaching unity. This is the second established case of a pronounced single-neutron halo beyond $^{11}$Be, although $^{14}$B and $^{15}$C might also be considered as qualifying for this epithet. All the measurements reported here have been limited by counting statistics and by the mediocre resolution of the NaI(Tl) $\gamma$ detectors. Very soon better measurements, based on a more powerful radioactive-beam facility and on segmented germanium detectors, should become possible.

Theory is the second essential ingredient in the kind of studies presented here. One cannot overestimate the importance of basing experiments and analysis on rigorous

theoretical models with a predetermined set of parameters and, if possible, offering a clear choice of alternatives. In the field of exotic nuclei, where only a limited amount of experimental information is available, it may be dangerous to work with flexible models that can be tailored to the needs of each individual nucleus and that, seen in isolation, may seem plausible. The version of the many-particle shell-model used in this work accounts very well for both single-particle and collective variables, and Tables 4.2, 5.1, 5.2, 5.3, and 5.4, demonstrate how a combination of $\ell$–assignments and spectroscopic factors can provide very detailed tests of nuclear structure. In the case of $^{17}$C a $\frac{3}{2}^+$ spin-parity is assigned, cf. the predictions for the excluded alternatives given in Table 5.3. Note also that the experiment successfully confirms the predicted 20% admixture of $\ell = 0$ in the predominantly $\ell = 2$ knockout to the $2^+$ level.

The absolute precision of the method still is an open question. Until now, investigated $\ell$–values and spectroscopic factors in about 20 partial cross sections have been investigated for proton and neutron removal reactions in the $p$– and $sd$–shells, and consistent results have been found. Preliminary estimates of the experimental and theoretical errors have been offered in [Nav00], and arrive in both ways at a relative value of $\pm 20\%$. The well known $^{15}$C nucleus has been investigated as a test of the method. The results indicate an overall agreement (70%) with theory. Fully quantum mechanical calculations of the elastic breakup explain the observed asymmetry of the measured momentum distribution (not present in the eikonal curves) and the dependence on the scattering angle. These calculations have also been performed to successfully interpret the momentum distribution of $^{11}$Be, which appears also asymmetric. However, the observed deviations do not affect the identification of the angular momentum value of the removed nucleon. Moreover, the calculated cross sections for the elastic breakup are similar in both cases, demonstrating the reliability of the reaction model. It remains to be seen whether this holds (or im-

proves) as more evidence accumulates, or whether there will be a need for fine-tuning the theory. Our current impression is that the knockout reactions show promise of becoming an interesting precision complement to the classical pickup reactions at low beam energies.

A more fundamental question is why there is such good agreement between experimental and theoretical cross sections. The connection between the two is provided by equation (3.1), which supplies the heuristic link between two seemingly unconnected theories. The spectroscopic factors are defined in a severely truncated Hilbert space with nucleons assumed to be the fundamental building blocks. These are subject to effective interactions, which take values adjusted to compensate for the neglected degrees of freedom. The reaction theory used for calculating the stripping and diffraction dissociation cross sections also, as it seems successfully, starts from a picture of quasi-free nucleons, generally believed to be valid at very high energies. Essential input parameters are nucleon densities and free nucleon-nucleon scattering cross sections. In the present work, this version of Glauber theory is applied well below the energy at which it is usually assumed to become a good approximation. In both calculations pre-existing parameter selections have been used and good agreement on an absolute scale has been obtained.

It is tempting to speculate that this agreement is not a mere coincidence. The reason could be that the reactions are surface-dominated [Tos99b, Tos99c], and that they sample predominantly the nuclear exterior. In this region, where the density is low, the nucleons of the effective-interaction theory have properties close to those of a free nucleon. To give a rough quantitative scale for the average size of the exterior sampled in the experiments, consider, for the case of a beryllium target, the ratio of a typical single-particle stripping cross section of about 30 mb to the free-neutron reaction cross section at the same energy of 300 mb. This means that the

observed cross sections represent the outer 10% of the single-particle wave function. The same argument is the key point in the analysis of the momentum distributions [Han95, Han96, Hes96], namely that the reactions sample just the momentum content of this external region and are blind to contributions from the (unexplored) interior. As was alluded to in the introduction to the experimental technique, section 2.1, the dominance of the nuclear surface is a general characteristic of nuclear spectroscopy via transfer reactions at lower energies.

The experiment involving the excited level of $^{15}$C showed that isomeric states produced in the knockout reaction can give rise to experimental complications and serves as a reminder that it may be prudent (as well as rewarding) in general to carry out a separate search for possible unknown isomers in the outgoing residues (what one could call the "tertiary beam"). The presence of isomers in the secondary beam from fragmentation has already allowed Grzywacz et al. [Grz98, Grz95, Grz97] to discover a number of interesting new isomers. This suggests as another possibility the use of the techniques discussed in the present work for investigating spectroscopic reactions of isomers. If the outcome of the reactions were sufficiently different, the presence of two species in the beam may not be an unsurmountable obstacle, provided that the ratio of the intensities were known from direct experiments.

# Appendix A

# Data Analysis

The data were analyzed using the program package PAW (Physics Analysis Worksta-
tion) [PAW]. It is an instrument that provides statistical and mathematical analysis,
as well as interactive graphical presentation for versatile multi-parameters data sets.
The data are arranged as arrays of variables, called "Ntuples", on an event-by-event
basis. From these variables, or any combination of them, it is possible to define gates
for selecting or discarding events. PAW can be used interactively or in batch mode
and dedicated programs can be written to conveniently manage the analysis.

A schematic outline of the general procedure is given in the following section.
However, the details of the analysis differ in the different cases, depending on specific
physics characteristics of the nuclei studied, or on the available statistics. Therefore,
the sections following the outline contain the details regarding the separate cases. The
analysis of $^{17}$C offers the most comprehensive case to illustrate the analysis, therefore
it will be discussed first. Then the cases of $^{15}$C, $^{16}$C and $^{19}$C will be described in the
order.

# A.1 Summary of the procedure

1. The preliminary inclusive cross section $\sigma_{p,incl}$ was derived as the ratio between the rate of detected fragments and the rate of incident projectiles, appropriately scaled by target thickness ($t$ [g/cm$^2$]) and live time and multiplied by the target number density ($A_t/N_A$). The gates are assumed to be as wide as possible to avoid any losses.

   An uncertainty on the stability of the incident beam rate was estimated by comparing the rates in the beam-line timer (BLT) of the different fragments produced in the reaction, run by run. Any fluctuation indicated a variation in the beam intensity and composition or even a shift in trajectory. In the case of the $^{15,16,17}$C this was estimated to give at most a 7% uncertainty, which combined with the uncertainties on target thickness, acceptance, events selection (all estimated to 5%), gave a 12% total uncertainty on the total cross section. For $^{19}$C, while the uncertainties on target, acceptance and event selection were still estimated to 5%, the very low statistics prevented the assessing of the beam stability with the same confidence as in the other cases, and a total 30% uncertainty on the cross section was determined.

2. The full momentum distributions were reconstructed with the ion optics code COSY INFINITY [Ber93], described in the second part of section 2.3.1.

   The inclusive momentum distribution was extracted and represented in absolute scale as $d\sigma/dP_\parallel$ (i.e., scaled so that its area represented the measured cross section as calculated in step 1).

3. The $\gamma$-ray spectrum was analyzed and the partial intensities $b$ and the partial momentum distributions corresponding to each final state were derived, taking

into account the $\gamma$ efficiency, possible feeding from other states and background events.

The measured branching ratios deduced from the $\gamma$-ray spectra analysis (with indirect feeding taken into account) are given in Tables 4.2, 5.1, 5.2, 5.3, and 5.4. The results obtained for $^{15,16,17,19}$C are described in detail in sections 4.3, 5.1.3, 5.2.3 and 5.3.3, respectively.

4. Possible losses due to the finite geometrical acceptance were estimated using simulations of the performance of the S800 spectrograph for a distribution of events generated by a Monte Carlo procedure, using the measured transverse momentum distributions. The corrections were applied to the distributions obtained in step 2 (inclusive) and to the ones from step 3 (exclusive).

5. Theoretical momentum distributions were calculated for the expected $\ell$ values of the removed neutron orbitals, following the model discussed in section 3.2.

6. The curves were used to fit the intensity of the corrected measured momentum distributions in an appropriate momentum range.

7. The spectrograph acceptance provided complete momentum distributions for the narrow distributions corresponding to low angular momentum ($\ell = 0, 1$) of the removed nucleon. The tails of higher $\ell$ distributions were lost, due to both the angular and the momentum acceptance. The additional contributions from the (unobserved) tails were estimated from the theoretical curves used to interpret the measured data. The final total and partial cross sections were then obtained.

In the case of the reaction of $^{17}$C leading to the first excited level of $^{16}$C the momentum distributions of the residues observed in coincidence with $\gamma$ rays

corresponded to a mixture of the $\ell$ values 0 and 2. This has served to subdivide the experimental branching ratio further, corresponding to the two $\ell$ values. A similar case was found in $^{14}$B [Gui00].

## A.1.1   The analysis in the case of $^{17}$C

1.

$$\sigma_{p,incl} = \frac{^{16}C/BLT}{^{17}C/BLT \times \text{livetime}} \times \frac{A_t \times 10^{27}}{N_A \times t} =$$

$$= \frac{38982/82172340}{0.2909 \times 0.98365} \times \frac{9 \times 10^{27}}{6.02 \times 10^{23} \times 0.228} = 109(13) \text{ mb}$$

Since the statistics were high and fluctuations were observed in the rate of fragments run by run, only the two closest runs to the elastic run were taken to derive the cross section. Three gates were determined on $\Delta E$ vs. $TOF$, on $TOF$ vs. $x801$ (position in first CRDC), and on $TOF$ vs. $x802$, (position in second CRDC). The data used to extract the cross section were those satisfying the first gate and either one of the two other gates.

3.   The analysis of the $\gamma$-ray spectrum (shown in Fig. 5.3) gave the following branching ratios (see also level scheme in Fig. 5.5):

$b(g.s.) = 19(9)\%$

$b(2^+) = 52(8)\%$

$b(2, 3^{(+)}, 4^+) = 29(5)\%$

4. The geometrical acceptance correction was estimated to be 3.6% and applied to the momentum distributions.

7. The momentum distributions were fitted using the calculated momentum distributions. To reproduce the intensities given by the result of the fitting procedure,

and account for the missing tails of the distributions, the following corrections needed to be applied to the experimental cross sections for each final state: 1.046 for the cross section to the ground state ($\sigma_{g.s.}$), 1.051 for the cross section to the $2^+$ state ($\sigma_{2+}$), and 1.083 for the cross section to the group of levels $2,3^{(+)},4^+$ ($\sigma_{2,3^{(+)},4+}$).

The estimated total average correction was then:

$$0.19 \times 1.046 + 0.52 \times 1.051 + 0.29 \times 1.083 \simeq 1.06$$

Therefore, the final inclusive cross section was:

$$\sigma_{incl} = 109(13) \times 1.06 = 115(14) \text{ mb}$$

and the absolute partial cross sections were:

$$\sigma_{g.s.} = 19(9)\% \text{ of } 115(14) \text{ mb} = 22(10)(3) \text{ mb} = 22(11) \text{ mb}$$

$$\sigma_{2+} = 52(8)\% \text{ of } 115(14) \text{ mb} = 60(9)(7) \text{ mb} = 60(12) \text{ mb}$$

$$\sigma_{2,3+,4+} = 29(5)\% \text{ of } 115(14) \text{ mb} = 33(6)(4) \text{ mb} = 33(7) \text{ mb}$$

Moreover, the $2^+$ momentum distribution is a mixture of $\ell = 0, 2$ values. A fit of the experimental distribution with the calculated $s-$ and $d-$wave momentum distributions (step 6) yielded $26(10)\%$ $s-$wave component and $74(10)\%$ $d-$wave component.

Therefore, the absolute branching ratios were:

$$b_{2+,s} = 26(10)\% \text{ of } 52(8)\% = 14(5)(2)\% = 14(6)\%$$

$$b_{2+,d} = 74(10)\% \text{ of } 52(8)\% = 38(5)(6)\% = 38(8)\%$$

and the corresponding cross sections were:

$$\sigma_{2+,s} = 16(7)(2) \text{ mb} = 16(7) \text{ mb}$$

$$\sigma_{2+,d} = 44(9)(5) \text{ mb} = 44(11) \text{ mb}$$

The momentum distribution corresponding to the residues in the group of excited states ($2,3^{(+)},4^+$) is also a mixture of $\ell = 0, 2$ values. The fit of the measured distribu-

tion with the $s-$ and $d-$wave distributions (step 6) yielded 8(8)% $s-$wave component and 92(8)% $d-$wave component.

Therefore the absolute branching ratios were:

$b_{2,3^+,4^+,s} = 8(8)\%$ of $29(5)\% = 2(2)(1)\% = 2(2)\%$

$b_{2,3^+,4^+,d} = 92(8)\%$ of $29(5)\% = 27(2)(5)\% = 27(5)\%$

and the absolute cross sections were:

$\sigma_{2,3^+,4^+,s} = 2(2)(0.2)$ mb $= 2(2)$ mb

$\sigma_{2,3^+,4^+,d} = 31(6)(4)$ mb $= 31(7)$ mb

## A.1.2 The analysis in the case of $^{15}$C

1.

$$\sigma_{p,incl} = \frac{^{14}C/BLT}{^{15}C/BLT \times \text{livetime}} \times \frac{A_t \times 10^{27}}{N_A \times t} =$$

$$= \frac{1042690/2.2029 \times 10^9}{0.2756 \times 0.8233} \times \frac{9 \times 10^{27}}{6.02 \times 10^{23} \times 0.228} = 137(16) \text{ mb}$$

The gates applied in this case were analogous to the ones used for $^{17}$C.

3. The $\gamma$-ray spectrum (Fig. 4.1) was analyzed as described in section 4.3 and the following branching ratios were obtained for the ground state and for the excited states of the $^{14}$C residues:

$b_{g.s.} = 79.7(2.0)\%$

$b_{exc.} = 20.3(2.0)\%$

In particular, three excited states were identified and the following branching ratios were found:

$b_{1^-} = 15.7(1.6)\%$

$$b_{0^-} = 2.5(0.5)\%$$

$$b_{2^+} = 2.1(0.5)\%$$

With $2^+$ it is referred here to the two unresolved excited states (both of spin parity $2^+$) predicted by theory at energies of 7-8 MeV.

4. The geometrical acceptance correction was estimated to be smaller than 1% and was thus neglected.

7. The momentum distributions of the $^{14}$C residues were wider than expected by theory (Fig. 4.2), therefore no correction was estimated for the momentum acceptance.

The absolute partial cross sections were then:

$$\sigma_{g.s.} = 79.7(2.0)\% \text{ of } 137(16) \text{ mb} = 109.2(2.7)(13.1) \text{ mb} \simeq 109(13) \text{ mb}$$

$$\sigma_{exc.} = 20.3(2.0)\% \text{ of } 137(16) \text{ mb} = 27.8(2.7)(3.3) \text{ mb} \simeq 28(4) \text{ mb.}$$

The cross section to the excited states could be further subdivided into the individual components:

$$\sigma_{1^-} = 15.7(1.6)\% \text{ of } 137(16) \text{ mb} = 21.5(2.2)(2.6) \text{ mb} \simeq 22(3) \text{ mb}$$

$$\sigma_{0^-} = 2.5(0.5)\% \text{ of } 137(16) \text{ mb} = 3.4(0.7)(0.4) \text{ mb} \simeq 3(1) \text{ mb}$$

$$\sigma_{2^+} = 2.1(0.5)\% \text{ of } 137(16) \text{ mb} = 2.9(0.7)(0.3) \text{ mb} \simeq 3(1) \text{ mb}$$

**Derivation of the angular distributions for $(^{15}\text{C},^{14}\text{C})$**

As discussed in detail in Chapter 4, the measured momentum distributions of the $^{14}$C residues from one-neutron removal reactions on $^{15}$C showed a characteristic dependence on the scattering angle. The same feature was observed in previous data from one-neutron removal reactions on $^{11}$Be. This section illustrates how the angular distributions of Fig. 4.6 were obtained, in the specific case of $^{15}$C. An analogous procedure was used to derive the angular distributions of Fig. 4.7, for the case of $^{11}$Be.

- Four $\gamma$-ray spectra were obtained for different scattering angle bins (from $0°$ to $4°$ in step of $1°$). The size of the steps was fixed by the measured angular resolution, which was calculated in the following way. The scattering angle $\theta_{sc}$ was given by:

$$\theta_{sc} = \arctan(\sqrt{\tan^2 \vartheta + \tan^2 \phi}),$$

where $\vartheta$ and $\phi$ were the angles measured with respect to the beam in the dispersive and non-dispersive direction, respectively.

For small angles the following approximation holds:

$$\theta_{sc} = \sqrt{\vartheta^2 + \phi^2}.$$

The above expression could be derived with respect to $\vartheta$ and $\phi$ and expressed in terms of finite increments, as:

$$\Delta\theta_{sc} = \sqrt{\frac{\vartheta^2 \Delta\vartheta^2 + \phi^2 \Delta\phi^2}{\vartheta^2 + \phi^2}}.$$

For a fixed $\theta_{sc}$ with an isotropic distribution, $\vartheta$ and $\phi$ may be expressed as $\vartheta = \theta_{sc} \cos v$ and $\phi = \theta_{sc} \sin v$.

Then,

$$\langle \Delta\theta_{sc}^2 \rangle = \frac{1}{\pi/2} \int_0^{\pi/2} \frac{\theta_{sc}^2 \cos^2 v \Delta\vartheta^2 + \theta_{sc}^2 \sin^2 v \Delta\phi^2}{\theta_{sc}^2} dv$$

$$= \frac{2}{\pi} \left[ \frac{\pi}{4} \Delta\vartheta^2 + \frac{\pi}{4} \Delta\phi^2 \right] = \frac{1}{2} \Delta\vartheta^2 + \frac{1}{2} \Delta\phi^2.$$

The measured FWHM resolutions for $\vartheta$ and $\phi$ were 23 mrad and 10 mrad, respectively. Recalling that FWHM $= 2.35\,\sigma$, the corresponding standard deviations were $\langle \Delta\vartheta \rangle^{1/2} \simeq 9.8$ mrad and $\langle \Delta\phi \rangle^{1/2} \simeq 4.2$ mrad.

This gave an experimental standard deviation for the scattering angle $\langle\Delta\theta^2_{sc}\rangle^{1/2} =$ 7.5 mrad $\simeq 0.4°$. The FWHM resolution was then approximately $1°$.

- The gated $\gamma$-ray spectra were interpreted analogously to the total spectrum as described above and in section 4.3. The results of the fits gave the intensity of the excited states, from which the ground state intensity was derived.

- For each scattering angle bin, using the $\gamma$-ray information, the momentum distribution corresponding to the ground state of the $^{14}C$ residues was obtained and divided by the solid angle subtended in that angular bin.

## A.1.3 The analysis in the case of $^{16}C$

1.

$$\sigma_{p,incl} = \frac{^{15}C/BLT}{^{16}C/BLT \times \text{ivetime}} \times \frac{A_t \times 10^{27}}{N_A \times t} =$$

$$= \frac{147753/441306528}{0.321 \times 0.9539} \times \frac{9 \times 10^{27}}{6.02 \times 10^{23} \times 0.228} = 72(9) \text{ mb}$$

Analogous gates to the ones used in the above cases were applied.

3. As discussed in detail in section 5.1.3, the $\gamma$-ray spectrum could not be used to derive the partial cross sections and momentum distributions, therefore the partial cross sections were obtained from the analysis of the inclusive momentum distribution.

4. The geometrical correction was estimated to be 2%.

6. The inclusive momentum distribution was subdivided into the two expected components corresponding to the removal of a neutron with angular momentum $\ell = 0, 2$. This was done by fitting the measured distribution with the theoretical curves and a mixture of 42(6)% $s$–wave and 58(6)% $d$–wave components was found.

7. From the fit a correction of 6.4% to the total cross section was obtained.

The absolute total and partial cross sections were then:

$$\sigma_{incl} = 72(9) \times 1.064 \text{ mb} = 77(9) \text{ mb}$$

$$\sigma_s = 42(6)\% \text{ of } 77(9) \text{ mb} = 32(5)(4) \text{ mb} = 32(6) \text{ mb}$$

$$\sigma_d = 58(6)\% \text{ of } 77(9) \text{ mb} = 45(5)(5) \text{ mb} = 45(7) \text{ mb}$$

## A.1.4   The analysis in the case of $^{19}$C

**The $^9$Be target**

1.

$$\sigma_{p,incl} = \frac{^{18}C/BLT}{^{19}C/BLT \times \text{livetime}} \times \frac{A_t \times 10^{27}}{N_A \times t} =$$

$$= \frac{131/16591729}{2.14 \times 10^{-3} \times 0.985} \times \frac{9 \times 10^{27}}{6.02 \times 10^{23} \times 0.228} = 245(74) \text{ mb}$$

As pointed out in section A.1, since fluctuations were observed in the rate of fragments run by run, only the three closest runs to the elastic run were taken to derive the cross section, as those were the most stable ones. Only the gate on $\Delta E$ vs. $TOF$ was applied. An uncertainty of 30% was determined, which included uncertainty on the incident projectiles rate, as well as the uncertainties on target thickness, acceptance and statistics.

4. The geometrical acceptance correction was found to be small in this case, in the momentum range (5.7-6 GeV/c) covered by the measured distribution.

6. The inclusive momentum distribution is a mixture of $\ell = 0, 2$ values. To extract the momentum distribution for the ground state (corresponding to an $s$–wave neutron), the distributions obtained with and without $\gamma$ coincidences were combined, appropriately weighted by the efficiency and background rate. A ground state branching of 60(10)% was deduced.

The efficiency was estimated from the simulations for the expected $\gamma$ rays (see section 5.3 for a detailed discussion of the level scheme of $^{19}$C).

Two $\gamma$ rays at 1.6 and 2.4 MeV are expected from the decay of the $2^+$ state at 1.6 MeV and from the cascade from the $0^+$ state at 4 MeV, with efficiencies of 23% and 22.6% respectively; two other excited states ($2^+$ and $3^+$) are expected from theory at $E \simeq 4.9$ MeV. Due to the tendency of the shell-model to overestimate the energy of the levels, and with the neutron threshold energy being equal to 4.2 MeV, those two were also taken into account. The cascade efficiency for the decay of the $\gamma$ rays with energies around 4 MeV was $\epsilon_c = 1 - (1 - \epsilon_1)(1 - \epsilon_2) \simeq 41.2\%$. The total estimated efficiency was then $b_{th}(2^+)\epsilon_1 + (b_{th}(0^+) + b_{th}(3^+) + b_{th}(2^+))\epsilon_c = 38.1\%$.

As discussed in section 2.4.2, a background intensity of 9% with an integral cut-off at 0.25 MeV was estimated from the analysis of ($^{16}$C,$^{15}$C) and ($^{12}$Be,$^{11}$Be), which have no $\gamma$ rays above 0.74 and 0.32 MeV, respectively, and consistently with the ($^{11}$Be,$^{10}$Be) data.

7. The correction factors for the partial cross sections obtained from the calculated distributions were 1.002 for the ground state, 1.17 for the $2^+$ state, 1.02 for the $0^+$ state and 1.23 for the $2^+,3^+$ states, which were analyzed together.

The deduced average correction for the total cross section was then 7.6%. Therefore the absolute inclusive cross sections was:

$\sigma_{incl} = 245(74) \times 1.076$ mb $= 264(80)$ mb

and the absolute branching ratios and partial cross sections were:

$\sigma_{g.s.} = 56(9)\%$ of $264(80)$ mb $= 148(24)(44)$ mb $= 148(50)$ mb

$\sigma_{exc.} = 44(11)\%$ of $264(80)$ mb $= 116(29)(35)$ mb $= 116(45)$ mb

Here, the branch to the excited states was assumed to result from different con-

tributions (taken from theory) by the $2^+$ state at 1.6 MeV, the $0^+$ state at 4 MeV, and the $2^+,3^+$ states predicted around 4.9 MeV.

## The $^{197}$Au target

1.

$$\sigma_{p,incl} = \frac{^{18}C/BLT}{^{19}C/BLT \times \text{livetime}} \times \frac{A_t \times 10^{27}}{N_A \times t} =$$

$$= \frac{120/1.8 \times 10^7}{3.12 \times 10^{-3} \times 0.99} \times \frac{197 \times 10^{27}}{6.02 \times 10^{23} \times 0.518} = 1.35(18) \text{ b}$$

Note that the flux of incident projectiles was stable in the two elastic runs recorded before and after the breakup runs. No significant fluctuactions were observed in the rate of produced fragments, therefore the data from all the runs were taken to calculate the cross section, with the usual gates. An uncertainty of 13% was assigned, which included the uncertainties on target thickness (5%), on gates (5%), incident rate (7%) and number of counts (10%).

4. The angular acceptance correction was found to be smaller than 2%.

6. The inclusive momentum distribution is a mixture of $\ell = 0, 2$ values. Analogously to the $^9$Be target case, the distributions obtained with and without $\gamma$ coincidences (appropriately weighted by the efficiency and background rate) were combined to extract the ground state and excited states momentum distributions. A ground state branch of 85(7)% was extracted.

The efficiency estimate was derived analogously to the $^9$Be target case. The only difference was that the cut-off was increased to 1 MeV, because the gold target gave more contribution to the background. The efficiencies for the two $\gamma$ rays at 1.6 and 2.4 MeV were then 13.3% and 15.5%, respectively; the cascade efficiency for the decay

of the $\gamma$ rays at 4-5 MeV was $\epsilon_c = 1 - (1 - \epsilon_1)(1 - \epsilon_2) = 26.7\%$. The total estimated efficiency was then $b_{th}(2^+)\epsilon_1 + (b_{th}(0^+) + b_{th}(3^+) + b_{th}(2^+))\epsilon_c = 24.3\%$.

With the integral cut-off at 1 MeV, a background intensity of 12% was estimated from the analysis of $(^{16}\text{C},^{15}\text{C})$ and $(^{12}\text{Be},^{11}\text{Be})$, and consistently with the $(^{11}\text{Be},^{10}\text{Be})$ data.

7. The absolute partial cross sections were then:

$\sigma_{g.s.} = 85(7)\%$ of $1.35(18)$ b $= 1.15(9)(15)$ b $= 1.15(18)$ b

$\sigma_{exc.} = 15(7)\%$ of $1.35(18)$ b $= 0.20(9)(3)$ b $= 0.20(10)$ b

the 13% error on the partial cross section, respectively.

# Bibliography

[Ajz91]    F. Ajzenberg-Selove et al. *Nucl. Phys. A*, 523:1, 1991.

[AlK96]    J.S. Al-Khalili, J.A. Tostevin, and I.J. Thompson. *Phys. Rev. C*, 54:1843, 1996.

[AlK00]    J.S. Al-Khalili. Private communication, 2000.

[Ann90]    R. Ann et al. *Phys. Lett. B*, 250:19, 1990.

[Arn87]    E. Arnold et al. *Phys. Lett. B*, 197:311, 1987.

[Aud93]    G. Audi and A.H. Wapstra. *Nucl. Phys. A*, 565:1, 1993.

[Aud97]    G. Audi et al. *Nucl. Phys. A*, 624:1, 1997.

[Aum00]    T. Aumann et al. *Phys. Rev. Lett.*, 84:35, 2000.

[Bal77]    D.P. Balamuth et al. *Nucl. Phys. A*, 290:65, 1977.

[Ban98]    P. Banerjee, I.J. Thompson, and J.A. Tostevin. *Phys. Rev. C*, 58:1042, 1998.

[Bau98]    T. Baumann et al. *Phys. Lett. B*, 439:256, 1998.

[Baz95]    D. Bazin et al. *Phys. Rev. Lett.*, 74:3569, 1995.

[Baz98]    D. Bazin et al. *Phys. Rev. C*, 57:2156, 1998.

[Bel95]     M.D. Belbot et al. *Phys. Rev. C*, 51:2372, 1995.

[Ber88]     C.A. Bertulani and G. Baur. *Nucl. Phys. A*, 480:615, 1988.

[Ber90]     G. Bertsch, H. Esbensen, and A. Sustich. *Phys. Rev. C*, 42:758, 1990.

[Ber93]     M. Berz et al. *Phys. Rev. C*, 47:537, 1993.

[Ber99]     U.C. Bergmann et al. *Nucl. Phys. A*, 658:129, 1999.

[Bla92]     B. Blank et al. *Z. Phys. A*, 343:375, 1992.

[Boh68]     G. Bohm et al. *Nucl. Phys. B*, 4:511, 1968.

[Boh70]     G. Bohm and F. Wisotzky. *Nucl. Phys. B*, 15:628, 1970.

[Boh75]     Aa. Bohr and B.R. Mottelson. *Nuclear Structure*, pages Vol. I p. 420, Vol. II p. 243. Benjamin, New York, 1969 and 1975.

[Bon98a]    A. Bonaccorso and D.M. Brink. *Phys. Rev. C*, 57:R22, 1998.

[Bon98b]    A. Bonaccorso and D.M. Brink. *Phys. Rev. C*, 58:2864, 1998.

[Bon99]     A. Bonaccorso. *Phys. Rev. C*, 60:054604, 1999.

[Bon00]     A. Bonaccorso. Private communication, 2000.

[Bro88]     B.A. Brown and B.H. Wildenthal. *Ann. Rev. Nucl. Part. Sci.*, 38:29, 1988. the USD energy levels are given at.

[Bro95]     B.A. Brown. In *ENAM95*, 1995.

[Bro98]     B.A. Brown. In *International School of Heavy-Ion Physics, $4^{th}$ Course: Exotic Nuclei*, 1998.

[Cag99]   J.A. Caggiano. *Spectroscopy of exotic nuclei with the S800 spectrograph.* PhD thesis, Michigan State University, 1999.

[Cat89]   W.N. Catford et al. *Nucl. Phys. A*, 503:263, 1989.

[Cha90]   S.K. Charagi and S.K. Gupta. *Phys. Rev. C*, 41:1610, 1990.

[Cha00]   R. Chatterjee et al. *Nucl. Phys. A*, 675:477, 2000.

[Che00]   L. Chen et al. Evidence for an $\ell$=0 Ground State in $^9$He. *Submitted to Phys. Rev. Lett.*, 2000.

[Chu00]   L.V. Chulkov et al. *Nucl. Phys. A*, 674:330, 2000.

[Cur86]   M.S. Curtin et al. *Phys. Rev. Lett.*, 56:34, 1986.

[Des00]   P. Descouvemont et al. *Nucl. Phys. A*, 675:559, 2000.

[Die90]   A.E.L. Dieperink and P.K.A. de Witt Huberts. *Ann. Rev. Nucl. Part. Sci.*, 40:239, 1990.

[Duf86]   J. P. Dufour et al. *Z. Phys. A*, 324:487, 1986.

[Fes92]   H. Feshbach. *Theoretical Nuclear Physics: Nuclear Reactions*, page 455. Wiley, New York, 1992.

[Fif82]   L.K. Fifield et al. *Nucl. Phys. A*, 385:505, 1982.

[For77]   H.T. Fortune et al. *Phys. Lett. B*, 70:408, 1977.

[For78]   H.T. Fortune et al. *Phys. Rev. Lett.*, 40:1236, 1978.

[Fuk91]   M. Fukuda et al. *Phys. Lett. B*, 268:339, 1991.

[Gea94]   Geant. Cern Library Long Writeup. Technical Report W5013, CERN, 1994.

[Gla59]    R.J. Glauber. *Lectures in Theoretical Physics*, volume 1, page 315. Interscience, New York, 1959.

[Gos73]    J.D. Goss et al. *Phys. Rev. C*, 8:514, 1973.

[Grz95]    R. Grzywacz et al. *Phys. Lett. B*, 355:439, 1995.

[Grz97]    R. Grzywacz et al. *Phys. Rev. C*, 55:1126, 1997.

[Grz98]    R. Grzywacz et al. *Phys. Rev. Lett.*, 81:247, 1998.

[Gui00]    V. Guimarães et al. *Phys. Rev. C*, 61:064609, 2000.

[Han87]    P.G. Hansen and B. Jonson. The neutron halo of extremely neutron-rich nuclei. *Europhys. Lett.*, 4:409, 1987.

[Han95]    P.G. Hansen. Nuclear halos: Structure and reactions. In *Proceedings of the International Conference on Exotic Nuclei and Atomic Masses*, Arles, France, June 1995.

[Han95]    P.G. Hansen, A.S. Jensen, and B. Jonson. *Ann. Rev. Nucl. Part. Sci.*, 45:591, 1995.

[Han96]    P.G. Hansen. *Phys. Rev. Lett.*, 77:1016, 1996.

[Han00]    P.G. Hansen. Private communication, 2000.

[Hen96]    K. Hencken, G. Bertsch, and H. Esbensen. *Phys. Rev. C*, 54:3043, 1996.

[Hes96]    H. Hesbensen. *Phys. Rev. C*, 53:2007, 1996.

[Hus85]    M.S. Hussein and K.W. McVoy. *Nucl. Phys. A*, 445:124, 1985.

[Kal96]    D.M. Kalassa and G. Baur. *J. Phys. G*, 22:115, 1996.

[Kan00]   R. Kanungo et al. *Nucl. Phys. A*, 677:171, 2000.

[Kel95]   J.H. Kelley et al. *Phys. Rev. Lett.*, 74:30, 1995.

[Kob88]   T. Kobayashi et al. *Phys. Rev. Lett.*, 60:2599, 1988.

[Kob89]   T. Kobayashi et al. *Phys. Lett. B*, 232:51, 1989.

[Kox87]   S. Kox et al. *Phys. Rev. C*, 35:1678, 1987.

[Lab99]   M. Labiche et al. *Phys. Rev. C*, 60:027303, 1999.

[Law76]   R.D. Lawson, F.J.D. Serduke, and H.T. Fortune. *Phys. Rev. C*, 14:1245, 1976.

[Lia90]   E. Liatard et al. *Europhys. Lett.*, 13:401, 1990.

[Mad00]   V. Maddalena et al. Single-neutron knockout reactions: Application to the spectroscopy of $^{16,17,19}$C. *Submitted to Phys. Rev. C*, 2000.

[Mar96]   F.M. Marqués et al. *Phys. Lett. B*, 381:407, 1996.

[Mil75]   D.J. Millener and D. Kurath. *Nucl. Phys. A*, 255:315, 1975.

[Nak99]   T. Nakamura et al. *Phys. Rev. Lett.*, 83:1112, 1999.

[Nav98]   A. Navin et al. *Phys. Rev. Lett.*, 81:5089, 1998.

[Nav00]   A. Navin et al. *Phys. Rev. Lett.*, 85:266, 2000.

[Orr91]   N. Orr et al. *Phys. Lett. B*, 258:29, 1991.

[Orr92]   N.A. Orr et al. *Phys. Rev. Lett.*, 69:2050, 1992.

[Oza98]   A. Ozawa et al. Measurements of interaction cross sections for Carbon isotopes at relativistic energies and the halo structure of $^{19}$C. Technical Report RIKEN-AF-NP-294, RIKEN, 1998.

[PAW]        Physics Analysis Workstation. http://wwwinfo.cern.ch/asd/paw/.

[Ray79]      L. Ray. *Phys. Rev. C*, 20:1857, 1979.

[Ren72]      P.U. Renberg et al. *Nucl. Phys. A*, 183:81, 1972.

[Rid97]      D. Ridikas et al. *Europhys. Lett.*, 37:385, 1997.

[Rid98]      D. Ridikas et al. *Nucl. Phys. A*, 628:363, 1998.

[Sai89]      M.G. Saint-Laurent et al. *Z. Phys. A*, 332:457, 1989.

[Sak99]      A. Sakharuk and V. Zelevinsky. *Phys. Rev. C*, 61:014609, 1999.

[Sat90]      G.R. Satchler. *Direct Nuclear Reactions*. Oxford, University Press, 1990.

[Sau00]      E. Sauvan et al. One-neutron removal reactions on neutron-rich psd-shell nuclei. *Submitted to Phys. Lett. B*, 2000.

[Sch99]      H. Scheit et al. *Nucl. Instr. Methods A*, 422:124, 1999.

[Ser78]      R.R. Sercely, R.J. Peterson, and E.R. Flynn. *Phys. Rev. C*, 17:1919, 1978.

[She92]      B.M. Sherrill et al. *Nucl. Instr. Methods B*, 70:298, 1992.

[She98]      R. Sherr and H.T. Fortune. *Phys. Rev. C*, 58:3292, 1998.

[Sme99]     M.H. Smedberg and M.V. Zhukov. *Phys. Rev. C*, 59:2048, 1999.

[Tan85]      I. Tanihata et al. *Physical Review Letters*, 55:2676, 1985.

[Til93]      D.R. Tilley et al. *Nucl. Phys. A*, 564:1, 1993.

[Tim96]     N.K. Timofeyuk and P. Descouvemont. *J. Phys. G*, 22:L99, 1996.

[Tos97]      J.A. Tostevin and J.S. Al-Khalili. *Nucl. Phys. A*, 616:418c, 1997.

[Tos99a]    J.A. Tostevin and J.S. Al-Khalili. *Phys. Rev. C*, 59:5R, 1999.

[Tos99b]    J.A. Tostevin. *J. Phys. G*, 25:735, 1999.

[Tos99c]    J.A. Tostevin. In *Fission and Properties of Neutron-Rich Nuclei, Proceedings of the Second International Conference*, page 429, St. Andrews, Scotland, 1999.

[Tos00]     J.A. Tostevin. Single-nucleon knockout reactions at fragmentation beam energies. To be published in Nucl. Phys. A, 2000. Paper presented at NS2000, International Conference on Nuclear Structure, East Lansing, MI, USA, August 13-19, 2000.

[War89]     E.K. Warburton and D.J. Millener. *Phys. Rev. C*, 39:1120, 1989.

[War92]     E.K. Warburton and B.A. Brown. *Phys. Rev. C*, 46:923, 1992.

[Wou88]     J. Wouters et al. *Z. Phys. A*, 331:229, 1988.

[Yab92]     K. Yabana, Y. Ogawa, and Y. Suzuki. *Nucl. Phys. A*, 539:293, 1992.

[Yam96]     T. Yamazaki et al. *Z. Phys. A*, 355:219, 1996.

[Yur99]     J. Yurkon et al. *Nucl. Instr. Methods A*, 422:291, 1999.

[Zah93]     M. Zahar et al. *Phys. Rev. C*, 48:R1484, 1993.